Title
Control and Self-Calibration of Microscale Rate Integrating Gyroscopes (MRIGs)

Author
Zhang, Fu

Publication Date
2015

Peer reviewed|Thesis/dissertation

Control and Self-Calibration of Microscale Rate Integrating Gyroscopes (MRIGs)

by

Fu Zhang

A dissertation submitted in partial satisfaction of the

requirements for the degree of

Doctor of Philosophy

in

Engineering - Mechanical Engineering

in the

Graduate Division

of the

University of California, Berkeley

Committee in charge:

Professor Roberto Horowitz, Chair
Professor Masayoshi Tomizuka
Associate Professor Pieter Abbeel

Fall 2015

Control and Self-Calibration of Microscale Rate Integrating Gyroscopes (MRIGs)

Abstract

Control and Self-Calibration of Microscale Rate Integrating Gyroscopes (MRIGs)

by

Fu Zhang

Doctor of Philosophy in Engineering - Mechanical Engineering

University of California, Berkeley

Professor Roberto Horowitz, Chair

This dissertation investigates the design of control algorithms and calibration methods for Microscale Rate Integrating Gyroscopes (MRIGs). As its name implies, a MRIG operates in rate integrating mode and can directly measure the rotation angle of the base where it is mounted. However, the MRIG mechanical system does not spontaneously operate in a rate integrating mode, but requires an active controller. Such a controller enables the MRIG to oscillate in a specific pattern that is related to the input rotation angle in a measurable way.

Conventional micro-machined gyroscopes (i.e. MEMS gyroscopes) operate in rate mode (as apposed to rate integrating mode). That is, the gyroscope directly measures the rotation rate of the base. The measured rotation rate is then numerically integrated over time to obtain the input rotation angle. The main drawback of this measuring mechanism is that, by integrating, the rate measurement error will propagate over time, causing the angle measurement to drift from the real input angle. MRIG, by its operating principle, can directly measure the input rotation angle; hence it suffers from no such error propagation.

A well-known control scheme for rate integrating gyroscopes was proposed by Lynch in 1995 [51]. This control scheme has demonstrated its efficacy on precisely fabricated rate integrating gyroscopes such as Hemispherical Resonance Gyroscopes (HRGs). However, for MRIGs fabricated by micro-fabrication technology, fabrication imperfections significantly degrade the gyro performance. In addition, the Lynch-proposed-scheme is essentially nonlinear. As a consequence, the controller performance is hard to predict and analyze prior to real tests.

In this dissertation, a novel demodulation method is developed to transform the original nonlinear control problem into a linear time invariant controller design problem. This technique is based on the averaging method proposed by Lynch [50] but enables the use of well studied linear system theory for MRIG controller design and analysis. The resulting controller design for MRIGs is much more tractable and the performance is rather predictable. This fundamental improvement also opens up new opportunities for implementing and analyzing

control systems based on linear control theory.

Two schemes are proposed in this dissertation to compensate for the parameter mismatches caused by fabrication imperfections. The first one is based on electrostatic spring softening and tuning. The basic operation principle is first introduced. Then a full derivation of this method on a real MRIG configuration is conducted. Experimental results confirm that this compensation scheme can significantly attenuate the parameter mismatch.

The other compensation scheme considered in this dissertation is an adaptive compensation scheme consisting of three feedforward controllers. Each of them runs on top of the corresponding feedback control loop and estimates and compensates parameter mismatches in real time. We also present a stability and convergence analysis that shows such adaptive controllers converge to the correct values and perfectly cancel the parameter mismatch. A simulation study performed on a MRIG model also confirms the efficacy of the compensation scheme. Then a self-calibration process is proposed to automatically calibrate the gyroscope. This self-calibration method requires no human involvement or auxiliary device, hence enables the gyroscope to calibrate itself whenever necessary, even in use.

Contents

List of Figures

List of Tables

Acknowledgments

I take this opportunity to show my sincerely appreciation to all of those people who have helped me completing the research described in this dissertation.

First and foremost, I express my deepest gratitude to my advisor Professor Roberto Horowitz. His wisdom and academic enthusiasms guided me through the most harsh period of the research. I feel much honored to have him as my advisor. Besides the valuable knowledge, he also delivered me the passion, the attitude and the persistence on academics. He means far more than a research advisor to me. Without his support and persistence, I would never have the opportunity to compose this dissertation. His constant support is the origin of the fruitful research. I am also grateful to have Professors Masayoshi Tomizuka, Karl Hedrick, Laurent El Ghaoui, and Pieter Abbeel on my qualification or dissertation committees.

I would like to appreciate the Mechanical Engineering department for awarding me two fellowships and providing all other resources, and the university for allowing me to take the qualifying exam and complete the PhD degree remotely. I show my sincerely thanks to all of those staff and faculty who have helped me on finishing this dissertation and my PhD degree.

I also want to extend my appreciation to my colleagues and lab mates. Especially, I want to thank Dr. Ehsan Keikha who has provided me great help on running simulation and performing experiments related to the research in this dissertation. I also thank my lab mate Behrooz Shahsavari.

This research is a subcontract from our industrial partner Honywell International Inc.. I would like to thank Dr. Burgess R. Johnson and all our other collaborators from Honeywell for their experimental setups and equipments, gyroscope modeling data and continuous and helpful feedback on control design development.

Finally, I would like to thank my friends and beloved family.

Chapter 1

Introduction

1.1 Background

Gyroscopes are sensing devices that are widely used to measure angular motion (i.e. rotation rate or rotation angle) of the object where they are mounted. They are self-contained sensing devices that operate without the use of external reference signals like GPS. Applications of gyroscopes include inertial navigation systems, vehicles stabilization and consumer electronics such as virtual reality, video games and smart phones, etc. [79, 19, 3].

By their functions, gyroscopes can be divided into two categories: rate gyroscopes and rate integrating gyroscopes [74]. Rate gyroscopes operate in the rate mode, where the gyroscope measures the rotation rate. The rotation angle is then obtained by numerically integrating the measured rate. Rate integrating gyroscopes operate in the rate integrating mode, where the gyroscope directly measures the rotation angle.

By their operation principles, gyroscopes include spinning mass gyroscopes, optical gyroscopes, vibratory gyroscopes, nuclear magnetic resonance gyroscopes and super-fluid gyroscopes [55, 42, 11, 88, 9]. We will briefly go through the first three types of gyroscopes in this text.

Spinning mass gyroscopes are based on the conservation of angular momentum law. They are usually configured with a wheel spinning at a very high speed with respect to a free movable frame which is anchored on the base [85]. The high speed spinning wheel has a tremendous angular momentum, which will tend to maintain its spinning axis at a constant direction. As a result, the spinning axis will remain static relative to the inertial frame, while the mount frame is rotating with the base. By detecting the relative rotation between the spinning axis and the mount frame, the rotation angle of the base can be measured. This process is illustrated in Fig. 1.1. Other variants of gyroscopes like gyrostats [25], gyrocompasses [39], etc. are based on similar facts.

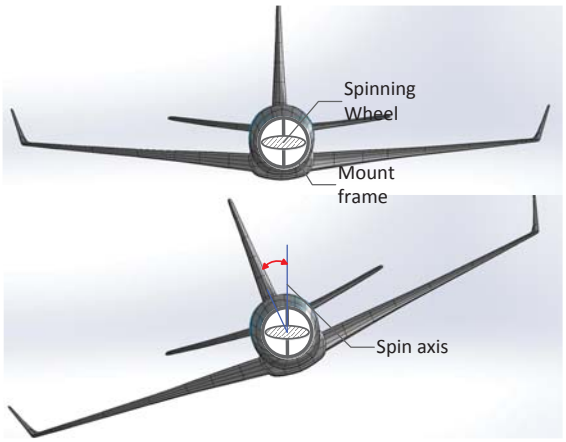

Figure 1.1: Operation principle of spinning mass gyroscopes. The spin axis does not alter its direction regardless of the attitude change of the base.

Spinning mass gyroscopes were used for many years in the aerospace and military industries. One successful spinning mass gyroscope is the Control Moment Gyroscope [41], which was widely used in space aircraft and satellite stabilization [21]. However, spinning mass gyroscopes are typical mechanical systems with bulky size. Their miniaturization is rather difficult and suffers from many mechanical limitations like wear, friction, shock and vibration. These drawbacks created great opportunities for optical and vibratory gyroscopes, which respectively utilize the integrated optical and Micro-Electro Mechanical System (MEMS) technologies for miniaturization [5].

The first optical gyroscope, the Ring Laser Gyroscope (RLG) [52], was developed in 1963, soon after the discovery of laser technology. Other optical gyroscopes include Fiber Optical Gyroscopes (FOGs) and integrated-optics gyroscopes [16, 17].

The operating principle of optical gyroscopes is based on the Sagnac effect [4]. As shown by Fig. 1.2, the gyroscope sends two laser beams around a closed loop path in opposite directions. If the beam splitter/receiver stays stationary, the two laser beams traverse the same distance to arrive to the receiver. However, if the beam splitter/receiver is rotating along the circle, then it takes a longer distance for the laser beam in front to traverse, causing a phase shift between the two received lasers. By detecting this phase shift, the rotational rate can be measured.

Because of its lack of mechanical moving parts, optical gyroscopes suffer from no mechanical wear or friction. In addition, due to the high consistency of the laser speed, optical gyroscopes provides extremely precise rotational rate information. Hence, they found many high-end applications like navy shipboard navigation despite their high costs [20] .

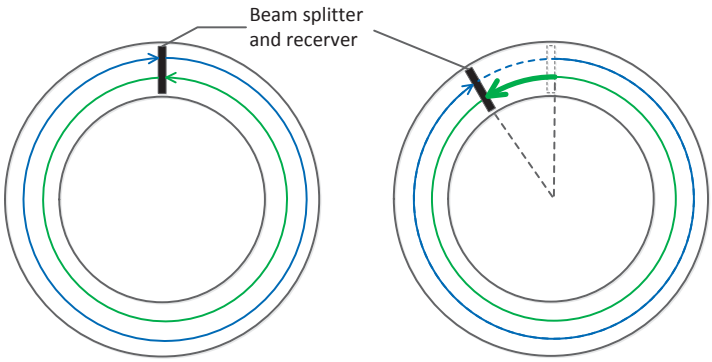

Figure 1.2: Sagnac effect

The class of vibratory gyroscopes, also known as Coriolis Vibratory Gyroscopes (CVGs), are based on the Coriolis effect. The basic configuration of most vibratory gyroscopes can be described by a proof mass attached by two perpendicular springs, as shown in Fig. 1.3. In this system, the mass oscillates along two directions that are perpendicular to each other. If the gyroscope is stationary, oscillations along these two directions are independent. However, when external rotation is present, oscillations along these two perpendicular directions will be coupled by the Coriolis acceleration. Since the Coriolis acceleration is proportional to the external rotation rate, by detecting the coupling motion, it is possible to measure the rotational motion of the frame. Micro-Electro Mechanical System (MEMS) gyroscopes and Hemispherical Resonator Gyroscopes (HRG) are the two most significant implementations of Coriolis Vibratory Gyroscopes.

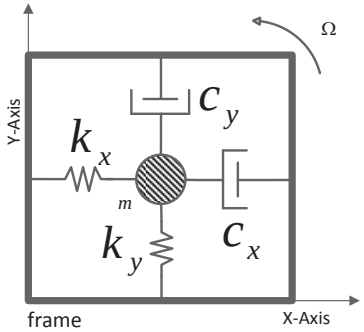

Figure 1.3: Schematic of a typical vibratory gyroscope configuration. The dampers are used to account for energy dissipation.

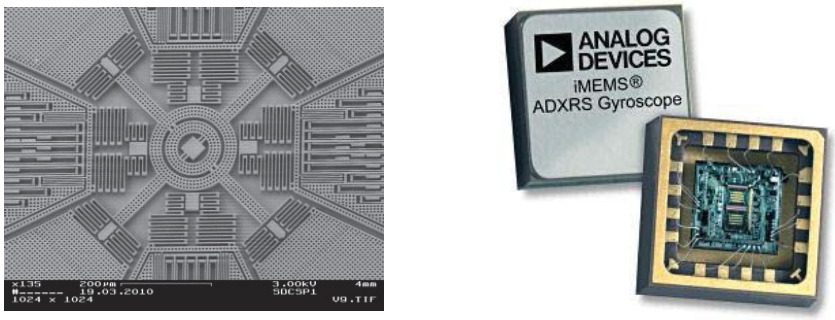

Figure 1.4: A generic MEMS gyroscope implementation (left) and the iMEMS ADXRS rate gyroscope package by Analog Devices (right). Pictures are taken from [29].

Benefiting from the MEMS technology, MEMS gyroscopes have their effective mass, spring components, sensing and driving electrodes all integrated in one package, as shown in Fig. 1.4. Such a package is in the size of electronic chips and can be integrated to driver circuits board. Compared with conventional mechanical gyroscopes, MEMS gyroscopes are several orders of magnitude smaller. In addition, MEMS batch processing techniques enable the production of large quantities of MEMS gyroscopes at a very low cost. Due to these benefits, MEMS gyroscopes have opened up new market opportunities [63, 58] and applications in the area of low-cost to medium performance inertial devices, like consumer electronics including smart phones, gaming systems, tablets, toys, wearable devices, etc., image stabilization, automotive applications and miniaturized air vehicles (MAVs) [62, 70].

To date, all commercially available MEMS gyroscopes are of the rate measuring type [80]. The main drawback of rate gyroscopes is that, by numerically integrating the measured rate, the measurement error will propagate, causing the angle measurement to drift from the ground true base rotation angle. Such a drawback limits the use of MEMS gyroscopes to be within low-end, cost and size crucial applications. More comprehensive discussion on rate versus rate integrating gyroscopes will be presented in subsequent chapters.

Hemispherical Resonance Gyros (HRGs) are another type of vibratory gyroscopes. They are configured with a thin solid-state hemispherical shell anchored by a thick stem at the center, as shown in Fig. 1.5. This shell is driven to flexural resonance by electrostatic forces generated by electrodes, which are deposited directly onto separate fused quartz structures that surround the shell. Due to the inertial property of the flexural standing waves, the Coriolis acceleration will cause a slow precession on the standing oscillatory wave [10], with a rate proportional to the input angular rate. Therefore when subject to external rotation, the standing wave does not totally rotate with the shell. The difference between both rotations, which can be sensed, is nevertheless perfectly proportional to the input rotation [86].

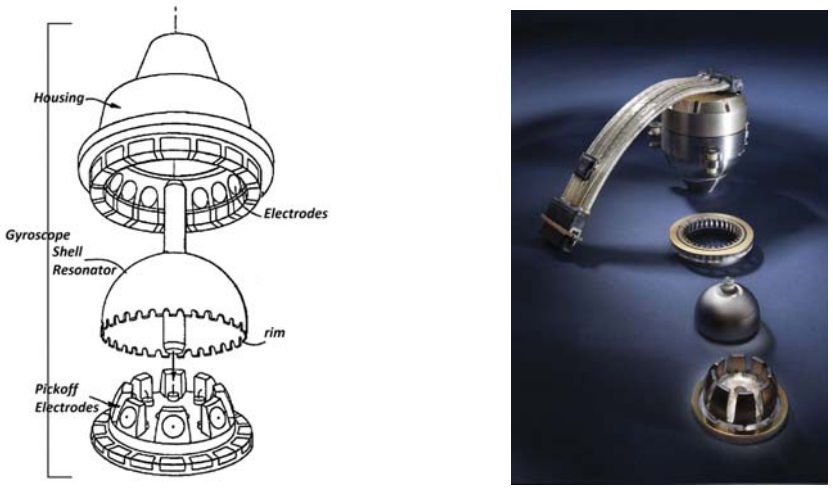

Figure 1.5: Configurations of a typical hemispherical resonator gyroscope (left) and a package example (right). Pictures are taken from [32] and [22].

The most prominent advantage of HRGs is perhaps its extremely simple hardware, containing no moving parts. In addition, the material character of shell resonator is rather stable. These features make HRGs extremely reliable and accurate, insensitive to external environmental perturbations like vibrations, accelerations and shocks. Moreover, HRGs can operate in either rate integrating mode (i.e. whole angle mode) that sense the standing waves position or rate mode (i.e. force to rebalance mode) that holds the standing wave in a fixed orientation with respect to the gyro.

HRG is a very high-tech device that requires a sophisticated manufacturing process in order to perfectly polish the hemispherical shell. In addition, in contrast to the MEMS gyroscopes, components of the HRG (the shell resonator, pickoff and driving electrodes, etc.) are separately manufactured. The multi-piece design requires a sophisticated assembly process. Such a process produces devices that have very high performance but at the same time high cost, large size and have a high power consumption [34].

1.2 Microscale Rate Integrating Gyroscopes (MRIGs)

MEMS gyroscopes have the advantage of very low cost and small size while rate integrating gyroscopes like HRGs have the advantage of extremely high reliability and accuracy. Current effort is being devoted on fabricating rate integrating gyroscopes using microfabrication technology, i.e. Microscale Rate Integrating Gyroscopes (MRIGs). Ideally, MRIGs can inherit the benefits of both: size and cost as low as MEMS gyroscopes but performance competitive with conventional HRGs [47, 73].

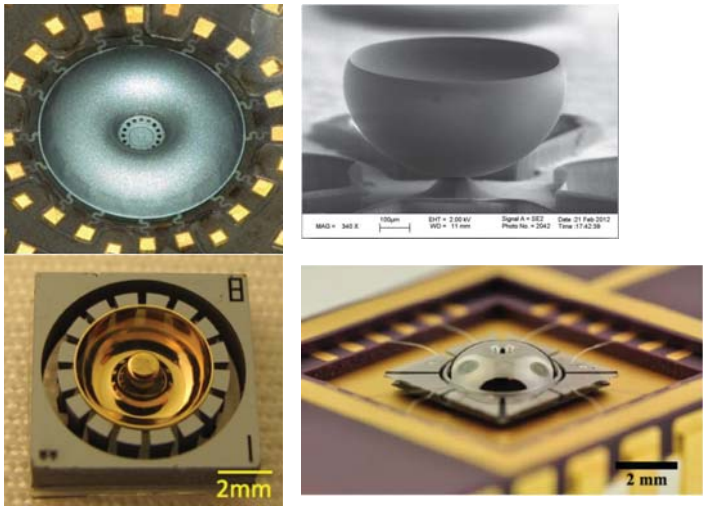

Figure 1.6: A number of successfully demonstrated MRIGs. Pictures are respectively taken from [37, 14, 78, 69].

.

Conventional micromachined gyroscopes (i.e. MEMS gyroscopes) measure the rotation rate by employing energy being transferred from the primary driving direction to the secondary sensing direction [1]. The resolution and sensitivity of MEMS gyroscopes are often improved by maximizing Q-factors and reducing the frequency mismatch between the two directions of vibration [84]. The measurement bandwidth is typically improved by utilizing a closed loop driving strategy, or force-rebalance mode [50]. The improvement is however at the cost of increasing the noise level and decreasing the bandwidth of the input angular rate.

In order for micromachined gyroscopes to measure the rotation angle directly, development has to be made on several aspects: precision 3-D fabrication technologies utilizing high-Q materials; wafer-level balancing and trimming techniques that reduce the effects of mass, stiffness and damping mismatches; and active control and calibration architectures [73].

During the last a few years, 3-D fabrication technology as well as wafer-level balancing and trimming techniques have been significantly improved. A number of MRIG prototypes have been successfully fabricated and demonstrated, as shown in Fig. 1.6. More MRIGs can be seen in [77, 31, 66, 78, 38, 65]

This dissertation considers the control and calibration for MRIGs. Topics covered in this dissertation include MRIG modeling, feedback controller design, stiffness and damping mismatch compensation and design of self-calibration methods.

1.3 Outline of the Dissertation

The remainder of this dissertation is organized as follows: Chapter 2 describes the basic configurations and theory of MRIGs. A comprehensive MRIG dynamic model, taking into account stiffness and damping mismatches caused by fabrication imperfections, is derived. The control objective is casted based on the trajectory solution of ideal MRIGs.

Chapter 3 addresses the control design for MRIGs. A well known feedback control strategy based on the averaging method introduced by Lynch [50] is first described. A full analysis of the effect of nonlinearities and stiffness and damping mismatches is then performed on such a control strategy. Then this dissertation presents a novel demodulation method that can eliminate the nonlinearities inherited in the Lynch control strategy. A linear time invariant controller design approach is proposed. Such an approach enables us to design, analyze and predict the performance of the controller using well established linear system theory.

Chapter 4 considers the stiffness mismatch compensation. A scheme based on electrostatic spring softening and tuning is proposed. It is shown that by applying a DC voltage on the MRIG driving or sensing electrodes, the MRIG stiffness will be softened by an extent determined by the amount of applied DC voltage. This creates a way to re-balance the stiffness mismatch caused by fabrication imperfections.

Chapter 5 considers an alternative mismatch compensation scheme. An adaptive feedfoward compensation scheme is presented and proven to converge. Such an adaptive compensator runs on top of the feedback controller and can estimate both stiffness and damping mismatch in real time. In order to calibrate the gyro mismatches, artificial input rate is then introduced to produce an autonomous calibration process. This self-calibration scheme is capable of calibrating the MRIG fully autonomous, requiring no auxiliary device or human involvement.

Chapter 6 concludes the dissertation by summarizing the results and major achievements.

Chapter 2

Basics of MRIGs

This chapter introduces the basic configurations and theory of Microscale Rate Integrating Gyroscopes (MRIGs). Mechanical and electronic components of a MRIG are modeled. A comprehensive dynamics that describes the MRIG vibrations is derived, by accounting for the stiffness and damping mismatch caused by fabrication imperfections [71]. The derived model will serve as the basic model for controller design in the subsequent chapters.

Behaviors of ideal MRIGs are studied in detail, by removing all the stiffness mismatch and damping effect from the comprehensive model. It is shown that the ideal MRIG is a natural rate integrating gyro, requiring no exogenous control input. Based on these facts, control objectives of actual MRIGs with stiffness mismatch and damping effect are casted.

2.1 Configurations of MRIGs

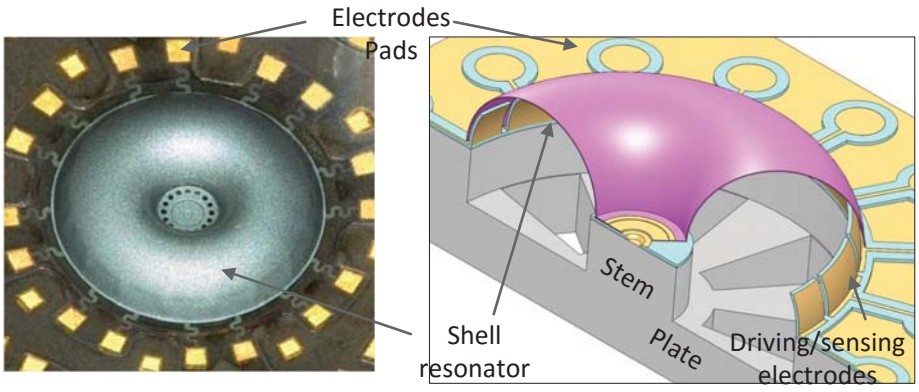

Figure 2.1: Microscope image of a MRIG fabricated by Honeywell (left) and its concept schematic (right). Courtesy of Burgess R. Johnson, Honeywell.

As shown in Fig. 2.1, a typical MRIG consists of a thin micro-machined shell resonator that is anchored on the plate by a thick stem at center. It also includes electrostatic driving electrodes and electrostatic sensing electrodes. It can be seen that such a configuration is very similar to that of Hemispherical Resonator Gyroscopes (HRGs). This is not surprising as MRIGs are essentially HRGs micro-machined on a chip. As shown in Fig. 2.2, the MRIG chip has a vacuum package with interfacing pads that can be used to drive or sense the shell vibration. The MRIG package is integrated to an analog front-end electronics board containing op-amps and D/A converters for the purpose of signal amplification and noise reduction, and then to a digital processor for signal processing and control purposes.

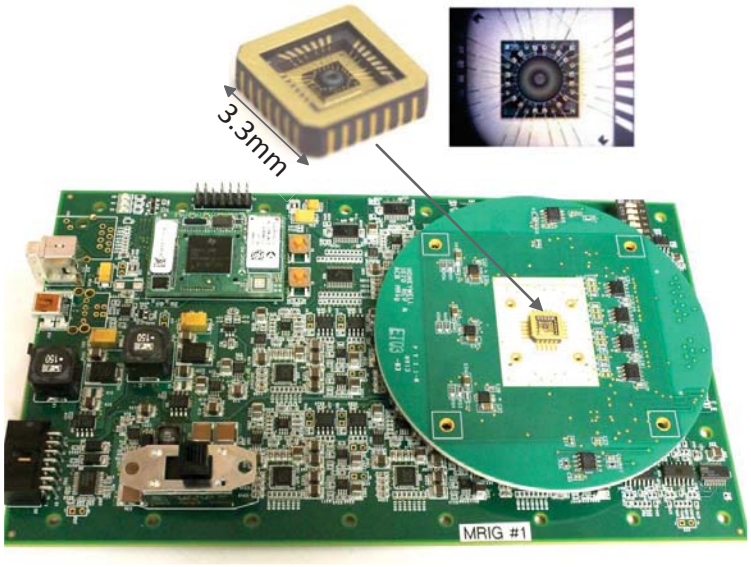

Figure 2.2: Analog front-end electronics (Circular board) with a 3.3 mm by 3.3 mm MRIG package manufactured by Honeywell, and a DSP board for gyro control. Courtesy of Burgess R. Johnson, Honeywell.

2.2 Vibration Modes of the Shell Resonator

The shell resonator is usually very thin and deformable. The deformation is repetitive at some resonance frequency that is determined by shell material and size. Hence, the shell is also called shell resonator. As shown in Fig. 2.3, there are three prominent vibration modes: $n = 0$ mode, $n = 1$ mode and $n = 2$ mode. The $n = 0$ mode refers to a vibration where the whole shell resonator moves up and down; the $n = 1$ mode refers to a vibration where the whole shell resonator tilts back and forth between left and right (primary vibration mode), or forward and backward (secondary vibration mode); the $n = 2$ mode refers to a

vibration where the shell deforms its rim along x and y axes (primary vibration mode), or along a direction in between x and y axes (secondary vibration mode). These three modes of vibration usually have different resonance frequencies. The preferred vibration mode can hence be excited by modulating the driving signal onto the corresponding resonance frequency.

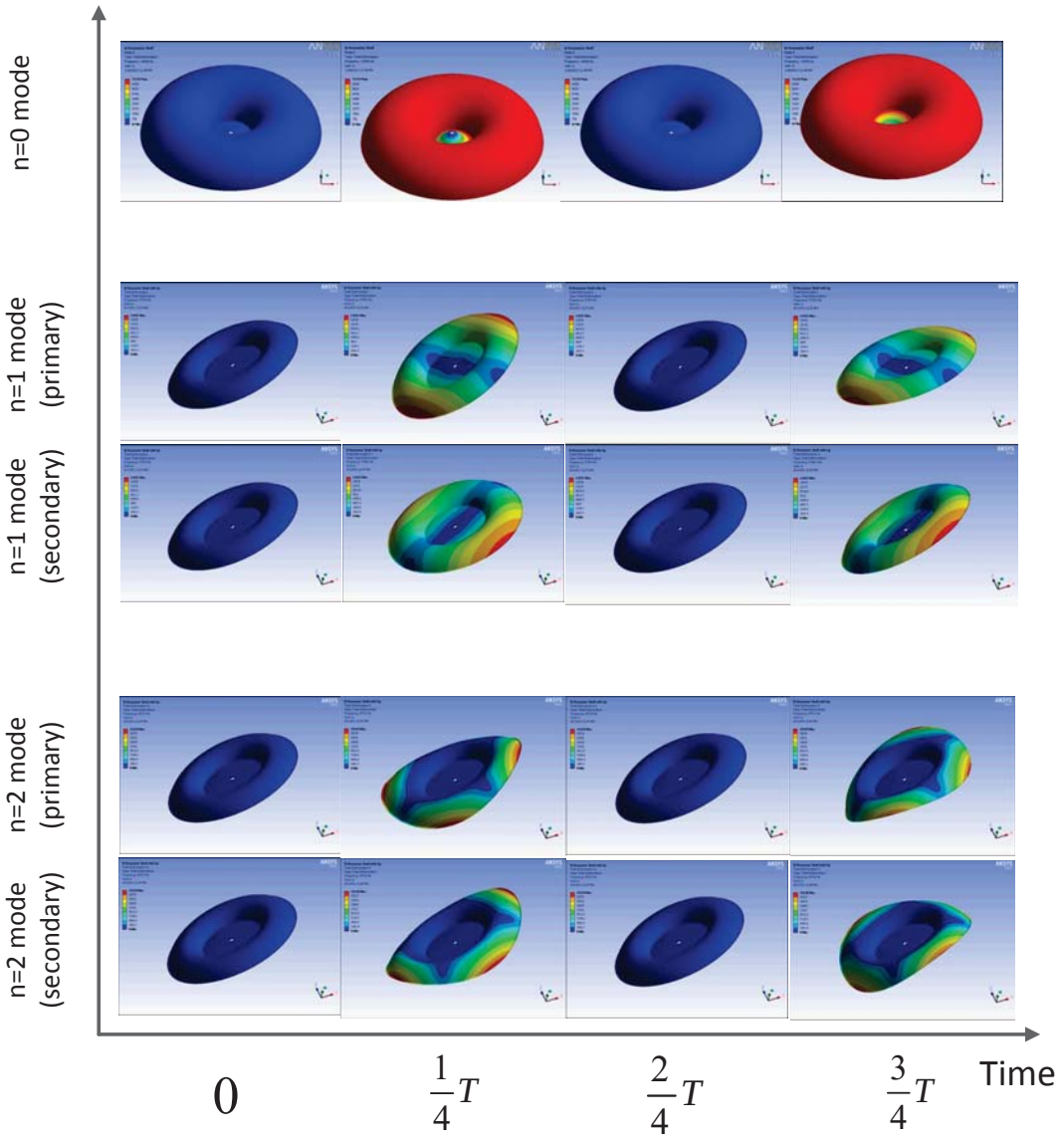

Figure 2.3: Vibration modes of a MRIG shell resonator simulated by ANSYS: $n = 0$ mode moves up and down (top), $n = 1$ mode tilts (middle) and $n = 2$ mode deforms the shell rim (bottom). Shapes of the shell resonator over a whole vibration period is considered. Courtesy of Burgess R. Johnson, Honeywell

2.3 The $n = 2$ Mode of Vibration

Among the three vibration modes discussed in preceding sections, the $n = 2$ mode is usually selected as the gyro operating mode due to its stable vibration pattern. In addition, the $n = 2$ mode of vibration has a modulate resonance frequency that achieves a good trade-off between the input bandwidth and the cost. Lower vibration frequency needs to lower the input rate bandwidth in order to obtain good Signal to Noise Ratio (SNR) while higher vibration frequency requires much more sophisticated sampling circuits and faster processor, which in turn increases the cost.

Fig. 2.4 depicts the top view of the $n = 2$ mode of vibration, when no external rotation is present. There are two vibration modes in the category of $n = 2$ mode of vibration: the primary vibration mode is the vibration pattern where the shell rim deforms into an ellipse with the principal and secondary axes repetitively aligned with Cartesian x and y axes; the secondary vibration mode is the vibration pattern where the shell rim deforms into an ellipse with the principal and secondary axes repetitively aligned with Cartesian x' and y' axes, which is rotated 45 degrees from the Cartesian $x - y$ coordinates. In addition, it can be observed that the two vibration modes are independent, i.e. when the primary vibration mode is excited, no vibration signal can be sensed from the secondary vibration mode (denoted as anti-node in the figure) and vice versa.

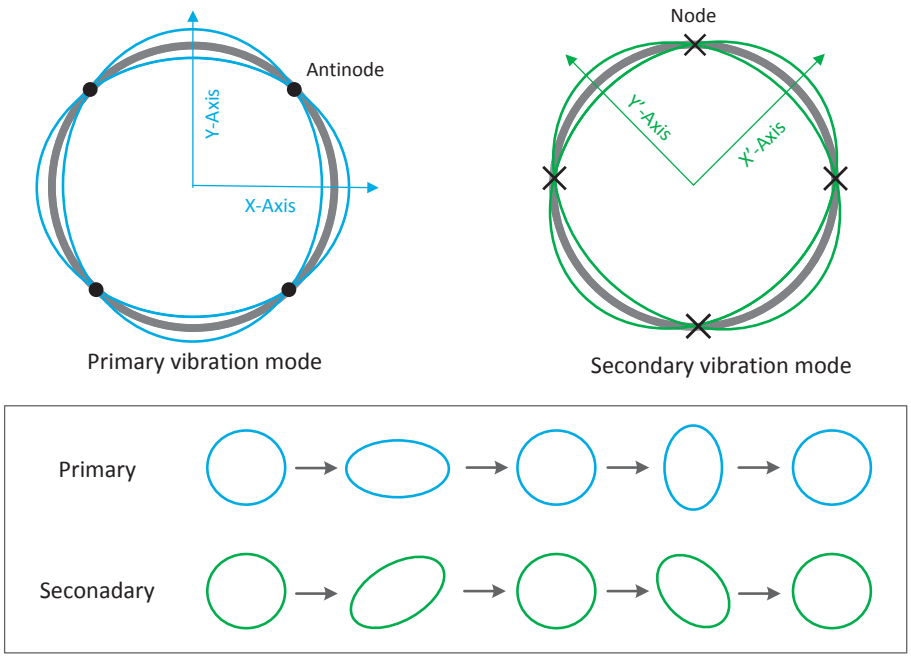

Figure 2.4: The primary and secondary vibration modes are independent for the $n = 2$ mode of vibration, when no external rotation is present.

2.4 Dynamics of the $n = 2$ Mode of Vibration

2.4.1 Equivalent Model

As discussed in preceding sections, the shell resonator's $n = 2$ mode of vibration has primary and secondary vibration modes that are independent to each other, when no external rotation is present. This fact enables us to model the shell resonator as a two dimensional harmonic oscillator shown in Fig. 2.5, where the two vibration modes are geometrically perpendicular, hence independent, to each other. This modeling approach can be validated by a more accurate modeling process based on solid-state thin shell theory presented in [82].

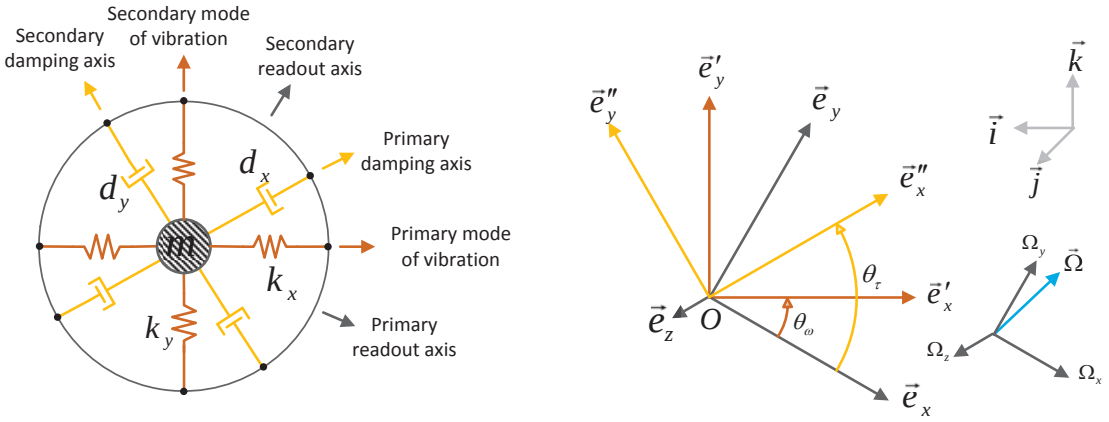

Figure 2.5: Schematic of a two dimensional harmonic oscillator (left) and its coordinate systems (right). In all the three types of coordinate systems, z-axis are the same and perpendicular to the paper plane.

Table 2.1: Summary of parameters in Fig. 2.5

Parameter	Description	Unit
Ω	Input rotation rate	rad/s
m	Effective mass	Kg
k_x	Stiffness of primary vibration mode	N/m
k_y	Stiffness of secondary vibration mode	N/m
d_x	Damping coefficient in the primary damping axis	$N \cdot s/m$
d_y	Damping coefficient in the secondary damping axis	$N \cdot s/m$
θ_ω	Azimuthal angle of stiffness axes	rad
θ_τ	Azimuthal angle of damping axes	rad

As shown in Fig. 2.5, due to the fabrication imperfections, the stiffness in the primary vibration mode k_x is different from the stiffness in the secondary vibration mode k_y, causing a stiffness mismatch. Dampers d_x and d_y are introduced to account for the energy dissipation. d_x is usually different from d_y as the energy dissipation over different vibration directions is usually different, which causes a damping mismatch. In addition, the readout electrodes are not ideally aligned with the stiffness principal axes nor the damping principal axes, as shown in Fig. 2.5. The resulting stiffness axes are misaligned with the readout axes by angle θ_ω while the damping axes are misaligned with the readout axes by angle θ_τ.

2.4.2 Coordinate Systems

In order to ease the subsequent analysis, we embed the readout axes, stiffness axes and damping axes respectively with the coordinate systems $\{O, \vec{e_x}, \vec{e_y}, \vec{e_z}\}$, $\{O, \vec{e_x}', \vec{e_y}', \vec{e_z}'\}$ and $\{O, \vec{e_x}'', \vec{e_y}'', \vec{e_z}''\}$. Then,

$$\begin{bmatrix} \vec{e_x}' & \vec{e_y}' & \vec{e_z}' \end{bmatrix} = \begin{bmatrix} \vec{e_x} & \vec{e_y} & \vec{e_z} \end{bmatrix} \begin{bmatrix} \cos(\theta_\omega) & -\sin(\theta_\omega) & 0 \\ \sin(\theta_\omega) & \cos(\theta_\omega) & 0 \\ 0 & 0 & 1 \end{bmatrix} \tag{2.1}$$

and

$$\begin{bmatrix} \vec{e_x}'' & \vec{e_y}'' & \vec{e_z}'' \end{bmatrix} = \begin{bmatrix} \vec{e_x} & \vec{e_y} & \vec{e_z} \end{bmatrix} \begin{bmatrix} \cos(\theta_\tau) & -\sin(\theta_\tau) & 0 \\ \sin(\theta_\tau) & \cos(\theta_\tau) & 0 \\ 0 & 0 & 1 \end{bmatrix} \tag{2.2}$$

These three coordinate systems are all static to the base and rotate with the base at the rate of $\vec{\Omega}$, with respect to the inertial frame $\{O, \vec{i}, \vec{j}, \vec{k}\}$. Note that the rotation rate $\vec{\Omega}$ is a vector that can be decomposed into either the body frame $\{O, \vec{e_x}, \vec{e_y}, \vec{e_z}\}$ or the inertial frame $\{O, \vec{i}, \vec{j}, \vec{k}\}$:

$$\vec{\Omega} = \begin{bmatrix} \vec{e_x} & \vec{e_y} & \vec{e_z} \end{bmatrix} \begin{bmatrix} \Omega_x \\ \Omega_y \\ \Omega_z \end{bmatrix} = \begin{bmatrix} \vec{i} & \vec{j} & \vec{k} \end{bmatrix} \begin{bmatrix} \Omega_i \\ \Omega_j \\ \Omega_k \end{bmatrix} \tag{2.3}$$

2.4.3 Kinematics

Since the coordinate system $\{O, \vec{e_x}, \vec{e_y}, \vec{e_z}\}$ (as well as $\{O, \vec{e_x}', \vec{e_y}', \vec{e_z}'\}$ and $\{O, \vec{e_x}'', \vec{e_y}'', \vec{e_z}''\}$) is rotating at the rate of $\vec{\Omega}$, it is subject to

$$\begin{aligned} \dot{\vec{e_x}} &= \vec{\Omega} \times \vec{e_x}; \quad \ddot{\vec{e_x}} = \dot{\vec{\Omega}} \times \vec{e_x} + \vec{\Omega} \times \dot{\vec{e_x}} \\ \dot{\vec{e_y}} &= \vec{\Omega} \times \vec{e_y}; \quad \ddot{\vec{e_y}} = \dot{\vec{\Omega}} \times \vec{e_y} + \vec{\Omega} \times \dot{\vec{e_y}} \\ \dot{\vec{e_z}} &= \vec{\Omega} \times \vec{e_z}; \quad \ddot{\vec{e_z}} = \dot{\vec{\Omega}} \times \vec{e_z} + \vec{\Omega} \times \dot{\vec{e_z}} \end{aligned} \tag{2.4}$$

2.4.4 Position Vector and Force Vector

Since the readout electrodes can only sense the displacement information of the shell resonator along the readout axes, it is quite straightforward to decompose the position vector of the point mass into the readout axes:

$$\begin{aligned} \vec{p} &= \vec{r} + x\vec{e_x} + y\vec{e_y} \\ \dot{\vec{p}} &= \dot{\vec{r}} + \dot{x}\vec{e_x} + \dot{y}\vec{e_y} + x\dot{\vec{e_x}} + y\dot{\vec{e_y}} \\ \ddot{\vec{p}} &= \ddot{\vec{r}} + \ddot{x}\vec{e_x} + \ddot{y}\vec{e_y} + 2\dot{x}\dot{\vec{e_x}} + 2\dot{y}\dot{\vec{e_y}} + x\ddot{\vec{e_x}} + y\ddot{\vec{e_y}} \end{aligned} \tag{2.5}$$

where $\vec{r}$ is the position vector of the shell center and $\ddot{\vec{r}}$ is the linear acceleration.

There are five types of forces acting on the point mass: gravity, normal force from the plate, spring induced forces, damper induced forces and control forces produced by the electrodes. Since the point mass is restricted to vibrate within the plane of $\vec{e_x}O\vec{e_y}$, the normal force cancels gravity, resulting in a total force as follows

$$\vec{F} = \vec{f} - k_x x'\vec{e_x}' - k_y y'\vec{e_y}' - d_x v_x''\vec{e_x}'' - d_y v_y''\vec{e_y}'' \tag{2.6}$$

where $\vec{f}$ is the control force applied on the point mass; x' and y' are respectively the $\vec{e_x}'$ and $\vec{e_y}'$ components of the relative position vector of the point mass to the shell center; v_x'' and v_y'' are respectively the $\vec{e_x}''$ and $\vec{e_y}''$ components of the relative velocity vector of the point mass to the shell center. Therefore, they are respectively subject to

$$\begin{bmatrix} x' \\ y' \end{bmatrix} = \begin{bmatrix} \cos(\theta_\omega) & \sin(\theta_\omega) \\ -\sin(\theta_\omega) & \cos(\theta_\omega) \end{bmatrix} \begin{bmatrix} x \\ y \end{bmatrix} \tag{2.7}$$

and

$$\begin{bmatrix} v_x'' \\ v_y'' \end{bmatrix} = \begin{bmatrix} \cos(\theta_\tau) & \sin(\theta_\tau) \\ -\sin(\theta_\tau) & \cos(\theta_\tau) \end{bmatrix} \begin{bmatrix} \dot{x} \\ \dot{y} \end{bmatrix} \tag{2.8}$$

2.4.5 Dynamics

Applying Newton's second law to the point mass yields

$$m\ddot{\vec{p}} = \vec{F} \tag{2.9}$$

Substituting Eq. (2.5) into the left hand side of Eq. (2.9), and Eq. (2.7), Eq. (2.8), Eq. (2.1) and Eq. (2.2) into the right hand side of Eq. (2.9) yields

$$\begin{aligned} &\ddot{x} - 2\Omega_z\dot{y} + \left(\Omega_x\Omega_y - \dot{\Omega}_z\right)y + \left(\tfrac{\frac{k_x}{m}+\frac{k_y}{m}}{2} - \Omega_y^2 - \Omega_z^2\right)x + \ddot{r}_x \\ &\quad + \tfrac{\frac{d_x}{m}+\frac{d_y}{m}}{2}\dot{x} + \tfrac{\frac{d_x}{m}-\frac{d_y}{m}}{2}\left(\dot{x}\cos 2\theta_\tau + \dot{y}\sin 2\theta_\tau\right) + \tfrac{\frac{k_x}{m}-\frac{k_y}{m}}{2}\left(x\cos 2\theta_\omega + y\sin 2\theta_\omega\right) &&= \tfrac{f_x}{m} \\ &\ddot{y} + 2\Omega_z\dot{x} + \left(\Omega_x\Omega_y + \dot{\Omega}_z\right)x + \left(\tfrac{\frac{k_x}{m}+\frac{k_y}{m}}{2} - \Omega_x^2 - \Omega_z^2\right)y + \ddot{r}_y \\ &\quad + \tfrac{\frac{d_x}{m}+\frac{d_y}{m}}{2}\dot{y} + \tfrac{\frac{d_x}{m}-\frac{d_y}{m}}{2}\left(\dot{x}\sin 2\theta_\tau - \dot{y}\cos 2\theta_\tau\right) + \tfrac{\frac{k_x}{m}-\frac{k_y}{m}}{2}\left(x\sin 2\theta_\omega - y\cos 2\theta_\omega\right) &&= \tfrac{f_y}{m} \end{aligned} \tag{2.10}$$

where $\ddot{r}_x$ and $\ddot{r}_y$ are respectively the $\vec{e_x}$ and $\vec{e_y}$ components of the linear acceleration; Ω_x, Ω_y and Ω_z are respectively the $\vec{e_x}, \vec{e_y}$ and $\vec{e_z}$ components of the rotation rate vector $\vec{\Omega}$, as seen in the first part of Eq. (2.3).

Re-parameterizing Eq. (2.10) using parameters summarized in Table 2.2 yields

$$\begin{aligned}
&\ddot{x} - 2\Omega_z\dot{y} + \left(\Omega_x\Omega_y - \dot{\Omega}_z\right) y + \left(\omega^2 - \Omega_y^2 - \Omega_z^2\right) x \\
&\quad + \frac{2}{\tau}\dot{x} + \Delta\left(\frac{1}{\tau}\right)\left(\dot{x}\cos 2\theta_\tau + \dot{y}\sin 2\theta_\tau\right) - \omega\Delta\omega\left(x\cos 2\theta_\omega + y\sin 2\theta_\omega\right) = g_x + \frac{f_x}{m} \\
&\ddot{y} + 2\Omega_z\dot{x} + \left(\Omega_x\Omega_y + \dot{\Omega}_z\right) x + \left(\omega^2 - \Omega_x^2 - \Omega_z^2\right) y \\
&\quad + \frac{2}{\tau}\dot{y} - \Delta\left(\frac{1}{\tau}\right)\left(-\dot{x}\sin 2\theta_\tau + \dot{y}\cos 2\theta_\tau\right) - \omega\Delta\omega\left(x\sin 2\theta_\omega - y\cos 2\theta_\omega\right) = g_y + \frac{f_y}{m}
\end{aligned} \tag{2.11}$$

Table 2.2: Summary of parameters in Eq. (2.11)

Parameter	Description	Unit
x	Position in the x direction	m
y	Position in the y direction	m
f_x	Control force in the x direction	N
f_y	Control force in the y direction	N
ω_x	Resonance frequency in the x direction, $\omega_x = \sqrt{\frac{k_x}{m}}$	rad/s
ω_y	Resonance frequency in the y direction, $\omega_y = \sqrt{\frac{k_y}{m}}$	rad/s
ω	Resonance frequency, $\omega = \sqrt{\frac{\omega_y^2+\omega_x^2}{2}}$	rad/s
$\Delta\omega$	Frequency mismatch, $\Delta\omega = \frac{\omega_y^2-\omega_x^2}{2\omega}$	rad/s
$\frac{1}{\tau_x}$	Decay rate in the x direction, $\frac{1}{\tau_x} = \frac{d_x}{2m}$	$1/s$
$\frac{1}{\tau_y}$	Decay rate in the y direction, $\frac{1}{\tau_y} = \frac{d_y}{2m}$	$1/s$
$\frac{2}{\tau}$	Decay rate, $\frac{2}{\tau} = \frac{1}{\tau_x} + \frac{1}{\tau_y}$	$1/s$
$\Delta\left(\frac{1}{\tau}\right)$	Damping mismatch, $\Delta\left(\frac{1}{\tau}\right) = \frac{1}{\tau_x} - \frac{1}{\tau_y}$	$1/s$
g_x	Deceleration in the x direction	m^2/s
g_y	Deceleration in the y direction	m^2/s

where the x and y directions refer to the two perpendicular readout axes in the equivalent model. In the real shell resonator, the x direction refers to the Cartesian x and y axes, while the y direction refers to the Cartesian x' and y' axes, as seen in Fig. 2.4.

Noticing that in all applications the magnitude of the input rate $\vec{\Omega}$ is much smaller than the resonance frequency ω, the quadratic terms (i.e. $\Omega_x\Omega_y, \Omega_x^2, \Omega_y^2$ and Ω_z^2) can be considered as negligible. In addition, the linear decelerations g_x and g_y are usually far off the resonance frequency ω, producing no significant effect on the system's response. Changing the notation Ω_z to Ω yields the simplified shell resonator dynamics

$$\begin{aligned}
&\ddot{x} - 2\kappa\Omega\dot{y} - \kappa\dot{\Omega}y + \left(\omega^2 - \kappa^2\Omega^2\right)x \\
&\quad + \frac{2}{\tau}\dot{x} + \Delta\left(\frac{1}{\tau}\right)\left(\dot{x}\cos 2\theta_\tau + \dot{y}\sin 2\theta_\tau\right) - \omega\Delta\omega\left(x\cos 2\theta_\omega + y\sin 2\theta_\omega\right) = \frac{f_x}{m} \\
&\ddot{y} + 2\kappa\Omega\dot{x} + \kappa\dot{\Omega}x + \left(\omega^2 - \kappa^2\Omega^2\right)y \\
&\quad + \frac{2}{\tau}\dot{y} - \Delta\left(\frac{1}{\tau}\right)\left(-\dot{x}\sin 2\theta_\tau + \dot{y}\cos 2\theta_\tau\right) - \omega\Delta\omega\left(x\sin 2\theta_\omega - y\cos 2\theta_\omega\right) = \frac{f_y}{m}
\end{aligned} \tag{2.12}$$

where κ is a dimensionless gain factor that represents the ratio between the real external rotation rate and the gyro rotation rate. This gain is usually calibrated prior to the gyro operation. Ω refers to the rotation rate along the $\vec{e_z}$ axis.

Eq. (2.12) is the gyro model based on which the controller and compensation scheme will be designed. In Eq. (2.12), terms $2\kappa\Omega\dot{x}$ and $2\kappa\Omega\dot{y}$ are the well known Coriolis accelerations, which are proportional to the input rotation rate Ω. This is not surprising as the variables x and y being considered are the positions relative to the body frame $\{O, \vec{e_x}, \vec{e_y}, \vec{e_z}\}$,which is a non-inertial frame. It can be seen from Eq. (2.12) that the Coriolis accelerations $2\kappa\Omega\dot{x}$ and $2\kappa\Omega\dot{y}$ couple the x and y motions. This coupling phenomenon is called Coriolis effect, which is the fundamental operating principle of vibratory gyroscopes where the input rate or angle is measured by detecting this amount of coupling motion.

It is worth mentioning that, the cross damping effect between x and y produces the forces $d_{yx}\dot{x}$ and $d_{xy}\dot{y}$ that have the same form as the Coriolis acceleration. This can potentially produce an alias of the input rate. Mathematically, by grouping terms $\ddot{x}$, $\dot{x}$, x, $\ddot{y}$, $\dot{y}$ and y in Eq. (2.12), we can obtain

$$\begin{aligned}
&\ddot{x} + \left(\frac{2}{\tau} + \Delta\left(\frac{1}{\tau}\right)\cos 2\theta_\tau\right)\dot{x} + \left(\omega^2 - \kappa^2\Omega^2 - \omega\Delta\omega\cos 2\theta_\omega\right)x \\
&\quad \underbrace{- \left(2\kappa\Omega - \Delta\left(\frac{1}{\tau}\right)\sin 2\theta_\tau\right)\dot{y}}_{\text{disturbed Coriolis acceleration}} - \left(\kappa\dot{\Omega} + \omega\Delta\omega\sin 2\theta_\omega\right)y = \frac{f_x}{m} \\
&\ddot{y} + \left(\frac{2}{\tau} - \Delta\left(\frac{1}{\tau}\right)\cos 2\theta_\tau\right)\dot{y} + \left(\omega^2 - \kappa^2\Omega^2 + \omega\Delta\omega\cos 2\theta_\omega\right)y \\
&\quad \underbrace{+ \left(2\kappa\Omega + \Delta\left(\frac{1}{\tau}\right)\sin 2\theta_\tau\right)\dot{x}}_{\text{disturbed Coriolis acceleration}} + \left(\kappa\dot{\Omega} - \omega\Delta\omega\sin 2\theta_\omega\right)x = \frac{f_y}{m}
\end{aligned} \tag{2.13}$$

Fortunately, as shown in Eq. (2.13), the damping mismatch term $\Delta\left(\frac{1}{\tau}\right)\sin 2\theta_\tau$ decreases the Coriolis acceleration on the x direction while increasing the Coriolis acceleration on the y direction. Such a different effect on Coriolis accelerations makes it possible to distinguish and compensate the damping mismatch.

2.5 Electrostatic Sensing and Actuation

The sensing and actuation mechanisms used for detecting and driving the shell vibration usually include electrostatic, electromagnetic or piezoresisitive sensing and actuation. Among them, electrostatic sensing and actuation outperforms the other two mechanisms due to its low cost and power usage, and good stability, speed and resolution. Moreover, electrostatic electrodes are easy to integrate into Integrated Circuits (ICs) [7].

2.5.1 Electrostatic Sensing

Electrostatic sensing is based on parallel plate capacitance where the two movable plates will charge or discharge, hence producing a measurable current on the conditioning circuits.

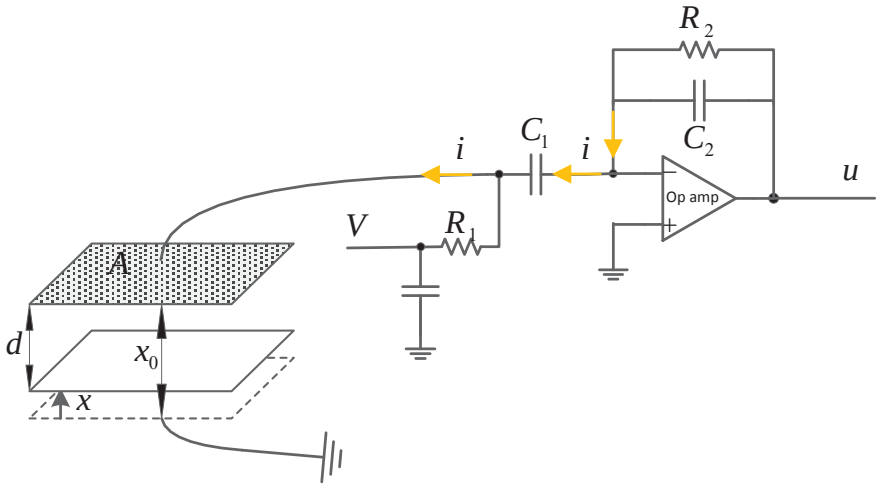

Figure 2.6: A parallel plate capacitor used as a sensor. A is the area of the plates; x_0 is the initial gap between plates; x is the displacement of the bottom plate; $d = x_0 - x$ is the actual gap; V is the bias voltage; $R_1 \gg \frac{1}{\omega C_1}$ in order to direct the current i to the integrating op-amp.

Fig. 2.6 shows a parallel plate capacitor and its integrating circuits. Based on the parallel plate capacitance theory presented in [57], the capacitance for a parallel plate capacitor is

$$C = \frac{\epsilon A}{d} = \frac{\epsilon A}{x_0 - x} \tag{2.14}$$

where ϵ is the permittivity of the material between plates.

Charges on the plates are

$$Q = CV \tag{2.15}$$

If the plates are moving towards to each other, the capacitance C is increased. Given a constant bias voltage, the plates will charge by Eq. (2.15), creating a current i

$$i = \frac{dQ}{dt} \tag{2.16}$$

Since the applied bias voltage V is usually constant, substituting Eq. (2.14) and Eq. (2.15) into Eq. (2.16) yields

$$i = \frac{dC}{dx}\frac{dx}{dt}V = \frac{\epsilon A}{(x_0 - x)^2}V\dot{x} \tag{2.17}$$

The series expansion of the current i around $x = 0$ is

$$i = \frac{\epsilon A}{x_0^2}V\dot{x} + 2\frac{\epsilon A}{x_0^3}Vx\dot{x} + o(x^2) \tag{2.18}$$

Since the magnitude of the shell deformation x is far less than the static gap x_0, the higher order terms $o(x^2)$ are negligible. In addition, since both of x and $\dot{x}$ are at the frequency of the resonance frequency ω, the cross term $x\dot{x}$ splits into a DC component and a 2ω frequency component, which can both be eliminated by the conditioning circuits, making their effect on the readout signal negligible. The simplified current is

$$i = \left(\frac{dC}{dx}\right)_{x=0} V\dot{x} \tag{2.19}$$

Since the resistor R_1 and capacitor are selected such that most of the current is directed to the integrating circuits, the output voltage is

$$u = \frac{R_2}{sR_2C_2 + 1}i \tag{2.20}$$

Substituting Eq. (2.19) into Eq. (2.20) yields

$$u = \left(\frac{dC}{dx}\right)_{x=0} V\frac{sR_2}{sR_2C_2 + 1}x \tag{2.21}$$

That is, the transfer function from the plate displacement to the measured voltage is

$$G_1(s) = \left(\frac{dC}{dx}\right)_{x=0} V\frac{sR_2}{sR_2C_2 + 1} \tag{2.22}$$

It can be seen that the readout circuit is essentially a high pass filter with corner frequency of $\frac{1}{R_2C_2}$. This implies that adding the resistor R_2 outperforms the pure integrator where $R_2 = \infty$, as it can effectively eliminate the DC disturbance in the readout signals.

2.5.2 Electrostatic Actuation

Electrostatic actuation is based on parallel plate capacitance where the two charged parallel plates produce an attractive force. The amount of attractive force produced is determined by the charge on the plates.

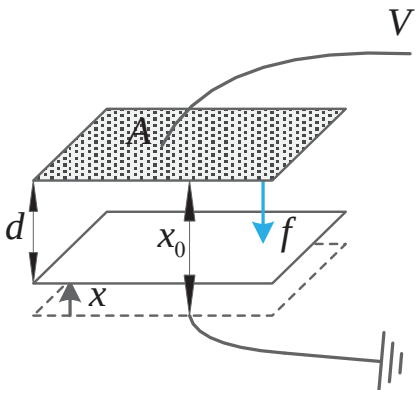

Figure 2.7: A parallel plate capacitor used as an actuator. V is the applied voltage; f is the attractive force produced on the plates.

The potential energy of a capacitor shown in Fig. 2.7 is [64]

$$E = \frac{1}{2}CV^2 \tag{2.23}$$

The resulting attractive force is

$$f = -\frac{\partial E}{\partial d} = -\frac{1}{2}\left(\frac{\partial C}{\partial d}\right)V^2 \tag{2.24}$$

Substituting Eq. (2.14) into Eq. (2.24) yields

$$f = \frac{1}{2}\frac{\epsilon A}{d^2}V^2 = \frac{1}{2}\frac{\epsilon A}{(x_0 - x)^2}V^2 \tag{2.25}$$

Performing a Taylor expansion and ignoring higher order terms yields the force produced by the plates

$$f = \frac{1}{2}\left(\frac{dC}{dx}\right)_{x=0}V^2 + \frac{1}{2}\left(\frac{d^2C}{dx^2}\right)_{x=0}V^2 x \tag{2.26}$$

It can be seen that the desired electrostatic force can be obtained by applying appropriate voltage on the electrodes.

2.6 Electrodes Configurations

Fig. 2.1 shows the electrodes configuration in a real gyro. Mechanically, electrodes are usually placed inside the shell resonator, right next to the shell rim, to form a parallel plate capacitor with the shell. The electrodes are fixed while the shell rim is deformable like a moving plate. Electronically, the whole shell resonator is grounded while the electrodes are connected to voltage sources that can be adjusted by controllers running on a processor.

A real gyro usually has multiple actuation and sensing electrodes that are respectively used to actuate and sense the displacement of the shell resonator from different directions. Fig. 2.8 shows a shell resonator with 16 electrodes, whose electrical configuration is depicted in Fig. 2.9.

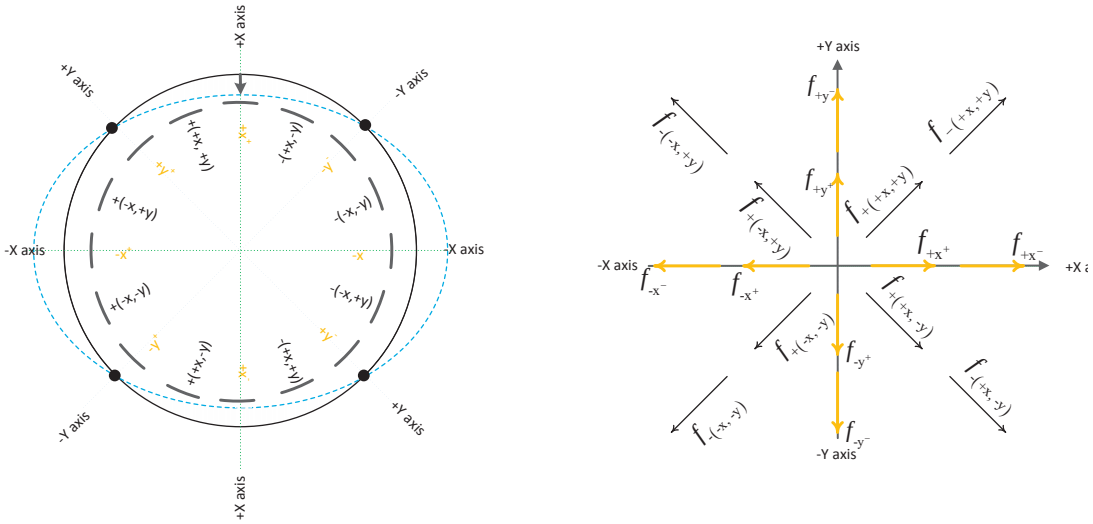

Figure 2.8: A shell resonator with 16 electrodes (left) and its equivalent model (right). Electrodes labeled with texts in orange color are readout electrodes while the remaining are used for actuation. Note that the readout electrodes also produce electrostatic forces. A positive displacement in the x direction refers to a rim deformation where the principal axis is horizontal while a negative one refers to a deformation where the principal axis is vertical. A positive force in the x direction refers to a force that attempts to produce a positive displacement in the x direction.

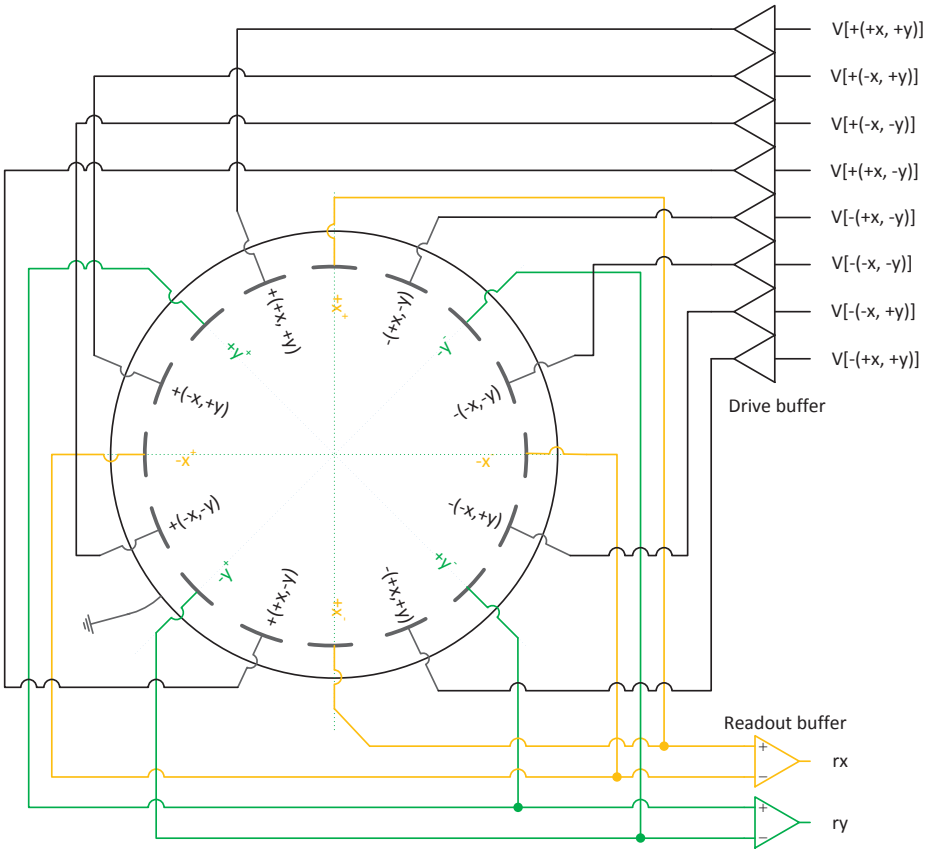

Figure 2.9: Electrical configurations of a shell resonator with 16 electrodes.

By Eq. (2.21), the voltages showing on the readout buffers are

$$\begin{aligned} r_x &= \left(\tfrac{dC}{dx}\right)_{x=0} \tfrac{sR_2}{sR_2C_2+1} \cdot \begin{pmatrix} + & V[+x^+]x[+x^+] + V[+x^-]x[+x^-] \\ + & V[-x^+]x[-x^+] + V[-x^-]x[-x^-] \end{pmatrix} \\ r_y &= \left(\tfrac{dC}{dx}\right)_{x=0} \tfrac{sR_2}{sR_2C_2+1} \cdot \begin{pmatrix} + & V[+y^+]x[+y^+] + V[+y^-]x[+y^-] \\ + & V[-y^+]x[-y^+] + V[-y^-]x[-y^-] \end{pmatrix} \end{aligned} \tag{2.27}$$

where $x[i]$ represents the displacement of the shell rim at i-th electrode; $V[i]$ represents the voltage applied on i-th electrode.

2.6.1 Geometry

Assume that x is the displacement of the shell deformation in the x direction and y is the displacement of the shell deformation in the y direction. Then the displacement at each of the sensing electrodes are

$$\begin{array}{rcl} x[+x^+] & = & x \\ x[+x^-] & = & x \\ x[-x^+] & = & -x \\ x[-x^-] & = & -x \\ x[+y^+] & = & y \\ x[+y^-] & = & y \\ x[-y^+] & = & -y \\ x[-y^-] & = & -y \end{array} \tag{2.28}$$

The displacement at each of the actuation electrodes is

$$\begin{array}{rcl} x[+(+x,+y)] & = & \frac{\sqrt{2}}{2}(x+y) \\ x[-(+x,+y)] & = & \frac{\sqrt{2}}{2}(x+y) \\ x[+(-x,+y)] & = & \frac{\sqrt{2}}{2}(-x+y) \\ x[-(-x,+y)] & = & \frac{\sqrt{2}}{2}(-x+y) \\ x[+(-x,-y)] & = & \frac{\sqrt{2}}{2}(-x-y) \\ x[-(-x,-y)] & = & \frac{\sqrt{2}}{2}(-x-y) \\ x[+(+x,-y)] & = & \frac{\sqrt{2}}{2}(x-y) \\ x[-(+x,-y)] & = & \frac{\sqrt{2}}{2}(x-y) \end{array} \tag{2.29}$$

Assume f_x is the total force on x direction while f_y is the total force on y direction, then

$$\begin{array}{rcl} f_x & = & \frac{\sqrt{2}}{2}\{f[+(+x,+y)] + f[-(+x,+y)] - f[+(-x,+y)] - f[-(-x,+y)] \\ & + & f[+(+x,-y)] + f[-(+x,-y)] - f[+(-x,-y)] - f[-(-x,-y)]\} \\ & + & f[+x^+] + f[+x^-] - f[-x^+] - f[-x^-] \\ f_y & = & \frac{\sqrt{2}}{2}\{f[+(+x,+y)] + f[-(+x,+y)] + f[+(-x,+y)] + f[-(-x,+y)] \\ & - & f[+(+x,-y)] - f[-(+x,-y)] - f[+(-x,-y)] - f[-(-x,-y)]\} \\ & + & f[+y^+] + f[+y^-] - f[-y^+] - f[-y^-] \end{array} \tag{2.30}$$

where $f[i]$ denotes the attractive force produced by i-th electrode.

2.6.2 Electrostatics

Combing Eq. (2.26) and Eq. (2.28) yields the forces produced by the readout electrodes

$$\begin{aligned}
f[+x^+] &= \tfrac{1}{2}\left(\tfrac{dC}{dx}\right)_{x=0}\cdot(V[+x^+])^2 + \tfrac{1}{2}\left(\tfrac{d^2C}{dx^2}\right)_{x=0}\cdot(V[+x^+])^2\cdot x \\
f[+x^-] &= \tfrac{1}{2}\left(\tfrac{dC}{dx}\right)_{x=0}\cdot(V[+x^-])^2 + \tfrac{1}{2}\left(\tfrac{d^2C}{dx^2}\right)_{x=0}\cdot(V[+x^-])^2\cdot x \\
f[-x^+] &= \tfrac{1}{2}\left(\tfrac{dC}{dx}\right)_{x=0}\cdot(V[-x^+])^2 - \tfrac{1}{2}\left(\tfrac{d^2C}{dx^2}\right)_{x=0}\cdot(V[-x^+])^2\cdot x \\
f[-x^-] &= \tfrac{1}{2}\left(\tfrac{dC}{dx}\right)_{x=0}\cdot(V[-x^-])^2 - \tfrac{1}{2}\left(\tfrac{d^2C}{dx^2}\right)_{x=0}\cdot(V[-x^-])^2\cdot x \\
f[+y^+] &= \tfrac{1}{2}\left(\tfrac{dC}{dx}\right)_{x=0}\cdot(V[+y^+])^2 + \tfrac{1}{2}\left(\tfrac{d^2C}{dx^2}\right)_{x=0}\cdot(V[+y^+])^2\cdot y \\
f[+y^-] &= \tfrac{1}{2}\left(\tfrac{dC}{dx}\right)_{x=0}\cdot(V[+y^-])^2 + \tfrac{1}{2}\left(\tfrac{d^2C}{dx^2}\right)_{x=0}\cdot(V[+y^-])^2\cdot y \\
f[-y^+] &= \tfrac{1}{2}\left(\tfrac{dC}{dx}\right)_{x=0}\cdot(V[-y^+])^2 - \tfrac{1}{2}\left(\tfrac{d^2C}{dx^2}\right)_{x=0}\cdot(V[-y^+])^2\cdot y \\
f[-y^-] &= \tfrac{1}{2}\left(\tfrac{dC}{dx}\right)_{x=0}\cdot(V[-y^-])^2 - \tfrac{1}{2}\left(\tfrac{d^2C}{dx^2}\right)_{x=0}\cdot(V[-y^-])^2\cdot y
\end{aligned} \tag{2.31}$$

Since the bias voltage for electrodes are always static, the first terms $\frac{1}{2}\left(\frac{dC}{dx}\right)_{x=0}\cdot V^2$ in Eq. (2.31) are always DC terms, showing no effect on the $n = 2$ mode of vibration that is at the resonance frequency of ω. Therefore, this term will be removed from the effective control forces in the subsequent analysis.

Combing Eq. (2.26) and Eq. (2.29) yields the forces produced by the actuation electrodes

$$
\begin{aligned}
f[+(+x,+y)] &= \tfrac{1}{2}\left(\tfrac{dC}{dx}\right)_{x=0}\cdot(V[+(+x,+y)])^2 \\
&\quad +\tfrac{\sqrt{2}}{4}\left(\tfrac{d^2C}{dx^2}\right)_{x=0}\cdot(V[+(+x,+y)])^2\cdot(x+y) \\
f[-(+x,+y)] &= \tfrac{1}{2}\left(\tfrac{dC}{dx}\right)_{x=0}\cdot(V[-(+x,+y)])^2 \\
&\quad +\tfrac{\sqrt{2}}{4}\left(\tfrac{d^2C}{dx^2}\right)_{x=0}\cdot(V[-(+x,+y)])^2\cdot(x+y) \\
f[+(-x,+y)] &= \tfrac{1}{2}\left(\tfrac{dC}{dx}\right)_{x=0}\cdot(V[+(-x,+y)])^2 \\
&\quad +\tfrac{\sqrt{2}}{4}\left(\tfrac{d^2C}{dx^2}\right)_{x=0}\cdot(V[+(-x,+y)])^2\cdot(-x+y) \\
f[-(-x,+y)] &= \tfrac{1}{2}\left(\tfrac{dC}{dx}\right)_{x=0}\cdot(V[-(-x,+y)])^2 \\
&\quad +\tfrac{\sqrt{2}}{4}\left(\tfrac{d^2C}{dx^2}\right)_{x=0}\cdot(V[-(-x,+y)])^2\cdot(-x+y) \\
f[+(-x,-y)] &= \tfrac{1}{2}\left(\tfrac{dC}{dx}\right)_{x=0}\cdot(V[+(-x,-y)])^2 \\
&\quad +\tfrac{\sqrt{2}}{4}\left(\tfrac{d^2C}{dx^2}\right)_{x=0}\cdot(V[+(-x,-y)])^2\cdot(-x-y) \\
f[-(-x,-y)] &= \tfrac{1}{2}\left(\tfrac{dC}{dx}\right)_{x=0}\cdot(V[-(-x,-y)])^2 \\
&\quad +\tfrac{\sqrt{2}}{4}\left(\tfrac{d^2C}{dx^2}\right)_{x=0}\cdot(V[-(-x,-y)])^2\cdot(-x-y) \\
f[+(+x,-y)] &= \tfrac{1}{2}\left(\tfrac{dC}{dx}\right)_{x=0}\cdot(V[+(+x,-y)])^2 \\
&\quad +\tfrac{\sqrt{2}}{4}\left(\tfrac{d^2C}{dx^2}\right)_{x=0}\cdot(V[+(+x,-y)])^2\cdot(x-y) \\
f[-(+x,-y)] &= \tfrac{1}{2}\left(\tfrac{dC}{dx}\right)_{x=0}\cdot(V[-(+x,-y)])^2 \\
&\quad +\tfrac{\sqrt{2}}{4}\left(\tfrac{d^2C}{dx^2}\right)_{x=0}\cdot(V[-(+x,-y)])^2\cdot(x-y)
\end{aligned}
\tag{2.32}
$$

2.6.3 Effective Control Forces

A commonly used driving strategy is biasing all the readout electrodes at the same voltage

$$\begin{array}{llll} V[+x^+] & = V[+x^-] & = V_b \\ V[-x^+] & = V[-x^-] & = -V_b \\ V[+y^+] & = V[+y^-] & = V_b \\ V[-y^+] & = V[-y^-] & = -V_b \end{array} \tag{2.33}$$

Substituting Eq. (2.33) and Eq. (2.28) into Eq. (2.27) yields the readout signals

$$\begin{array}{rcl} r_x & = & 4\left(\frac{dC}{dx}\right)_{x=0} V_b \frac{sR_2}{sR_2C_2+1} x \\ r_y & = & 4\left(\frac{dC}{dx}\right)_{x=0} V_b \frac{sR_2}{sR_2C_2+1} y \end{array} \tag{2.34}$$

The gain and phase delay at the resonance frequency ω are respectively

$$\begin{array}{rl} g & = 4\left(\frac{dC}{dx}\right)_{x=0} V_b \frac{\omega R_2}{\sqrt{(\omega R_2 C_2)^2+1}} \\ \phi & = \frac{\pi}{2} - \tan^{-1}\left(\omega R_2 C_2\right) \end{array} \tag{2.35}$$

For the actuation electrodes, the first terms of electrostatic force in Eq. (2.32), i.e. $\frac{1}{2}\left(\frac{dC}{dx}\right)_{x=0} \cdot (V[i])^2$, are utilized to excite the $n = 2$ mode of vibration. Hence, the squared voltage $(V[i])^2$ at electrode i is modulated to the frequency of ω. Since both of $(V[i])^2$ and x or y are at the frequency of ω, terms like $(V[i])^2 x$ and $(V[i])^2 y$ will split into two components: a DC component and a 2ω frequency component. Fortunately, neither of these two components show any effect on the $n = 2$ mode of vibration. As a result, the forces in the x and y directions can be simplified as

$$\begin{array}{rcl} f_x & = & \frac{\sqrt{2}}{4}\left(\frac{dC}{dx}\right)_{x=0} \cdot \left\{ \begin{array}{cl} & (V[+(+x,+y)])^2 + (V[-(+x,+y)])^2 \\ - & (V[+(-x,+y)])^2 - (V[-(-x,+y)])^2 \\ + & (V[+(+x,-y)])^2 + (V[-(+x,-y)])^2 \\ - & (V[+(-x,-y)])^2 - (V[-(-x,-y)])^2 \end{array} \right\} \\ & + & 2\left(\frac{d^2C}{dx^2}\right)_{x=0} V_b^2 x \\ f_y & = & \frac{\sqrt{2}}{4}\left(\frac{dC}{dx}\right)_{x=0} \cdot \left\{ \begin{array}{cl} & (V[+(+x,+y)])^2 + (V[-(+x,+y)])^2 \\ + & (V[+(-x,+y)])^2 + (V[-(-x,+y)])^2 \\ - & (V[+(+x,-y)])^2 - (V[-(+x,-y)])^2 \\ - & (V[+(-x,-y)])^2 - (V[-(-x,-y)])^2 \end{array} \right\} \\ & + & 2\left(\frac{d^2C}{dx^2}\right)_{x=0} V_b^2 y \end{array} \tag{2.36}$$

It is interesting to observe that the last terms in Eq. (2.36), i.e. $2\left(\frac{d^2C}{dx^2}\right)_{x=0} V_b^2 x$ and $2\left(\frac{d^2C}{dx^2}\right)_{x=0} V_b^2 y$, respectively soften the stiffness in the x and y directions by an amount of

of $2\left(\frac{d^2C}{dx^2}\right)_{x=0} V_b^2$. Lumping the stiffness softening terms into the resonance frequency yields the effective resonance frequency

$$\bar{\omega} = \sqrt{\omega^2 - 2\left(\frac{d^2C}{dx^2}\right)_{x=0} V_b^2} \tag{2.37}$$

and effective control forces

$$\begin{aligned}
\bar{f}_x &= \tfrac{\sqrt{2}}{4}\left(\tfrac{dC}{dx}\right)_{x=0} \cdot \left\{ \begin{array}{cc} & (V[+(+x,+y)])^2 + (V[-(+x,+y)])^2 \\ - & (V[+(-x,+y)])^2 - (V[-(-x,+y)])^2 \\ + & (V[+(+x,-y)])^2 + (V[-(+x,-y)])^2 \\ - & (V[+(-x,-y)])^2 - (V[-(-x,-y)])^2 \end{array} \right\} \\
\bar{f}_y &= \tfrac{\sqrt{2}}{4}\left(\tfrac{dC}{dx}\right)_{x=0} \cdot \left\{ \begin{array}{cc} & (V[+(+x,+y)])^2 + (V[-(+x,+y)])^2 \\ + & (V[+(-x,+y)])^2 + (V[-(-x,+y)])^2 \\ - & (V[+(+x,-y)])^2 - (V[-(+x,-y)])^2 \\ - & (V[+(-x,-y)])^2 - (V[-(-x,-y)])^2 \end{array} \right\}
\end{aligned} \tag{2.38}$$

In practice, the controller is designed with respect to the effective force acting in the x and y directions, i.e. $\bar{f}_x$ and $\bar{f}_y$. In order to produce the required control force computed by the controller, the voltage applied on each electrode can be

$$\begin{aligned}
V[+(+x,+y)] &= \sqrt{\frac{\max\{\bar{f}_x+\bar{f}_y,0\}}{\frac{\sqrt{2}}{2}\left(\frac{dC}{dx}\right)_{x=0}}} \\
V[-(+x,+y)] &= \sqrt{\frac{\max\{\bar{f}_x+\bar{f}_y,0\}}{\frac{\sqrt{2}}{2}\left(\frac{dC}{dx}\right)_{x=0}}} \\
V[+(-x,+y)] &= \sqrt{\frac{\max\{-\bar{f}_x+\bar{f}_y,0\}}{\frac{\sqrt{2}}{2}\left(\frac{dC}{dx}\right)_{x=0}}} \\
V[-(-x,+y)] &= \sqrt{\frac{\max\{-\bar{f}_x+\bar{f}_y,0\}}{\frac{\sqrt{2}}{2}\left(\frac{dC}{dx}\right)_{x=0}}} \\
V[+(+x,-y)] &= \sqrt{\frac{\max\{\bar{f}_x-\bar{f}_y,0\}}{\frac{\sqrt{2}}{2}\left(\frac{dC}{dx}\right)_{x=0}}} \\
V[-(+x,-y)] &= \sqrt{\frac{\max\{\bar{f}_x-\bar{f}_y,0\}}{\frac{\sqrt{2}}{2}\left(\frac{dC}{dx}\right)_{x=0}}} \\
V[+(-x,-y)] &= \sqrt{\frac{\max\{-\bar{f}_x-\bar{f}_y,0\}}{\frac{\sqrt{2}}{2}\left(\frac{dC}{dx}\right)_{x=0}}} \\
V[-(-x,-y)] &= \sqrt{\frac{\max\{-\bar{f}_x-\bar{f}_y,0\}}{\frac{\sqrt{2}}{2}\left(\frac{dC}{dx}\right)_{x=0}}}
\end{aligned} \tag{2.39}$$

Notice that in principle, there are an infinity number of ways to produce the required control forces, by properly choosing the electrodes voltage according to Eq. (2.38). Among them, Eq. (2.39) is the one that attempts to distribute the actuation effort among all the 8 actuation electrodes as even as possible.

2.7 MEMS Units

Since the vibration scale of the shell resonator is very small, usually in microns, the commonly used MKS units cause big numerical problems with such small numbers. Hence, the MEMS units are widely used when analyzing MRIGs. A comparison between MKS units and MEMS units is summarized in Table 2.3. It can be proven that all the aforementioned physical laws still hold under the MEMS units, therefore requiring no modification on the gyro dynamics.

Table 2.3: MKS units versus MEMS units

Variables	MKS units	MEMS units
Length	Meter	Microns
Mass	Kilograms	Kilograms
Time	Seconds	Seconds
Energy	Joule	pico-Joule
Force	Newtons	micro-Newtons
Electric potential	Volts	Volts
Capacitance	Fara	pico-Fara

2.8 Precession of Ideal MRIGs

Ideal MRIGs refer to the class of MRIGs that are perfectly fabricated and trimmed to get rid of all the damping, frequency mismatch and misalignments between the stiffness principal axes and readout axes. Hence, an ideal MRIG is symmetric and free from energy dissipation. Ideal MRIGs are usually introduced for the purpose of analyzing the gyro behaviors. In practice, due to the fabrication imperfections, a real MRIG usually suffers from a significant level of frequency mismatch and energy dissipation.

Setting the damping term $\frac{1}{\tau}$, damping mismatch term $\Delta(\frac{1}{\tau})$, and frequency mismatch term $\Delta\omega$ in Eq. (2.12) to zeros yields the dynamics of ideal MRIGs

$$\begin{aligned} \ddot{x} - 2\kappa\Omega\dot{y} - \kappa\dot{\Omega}y + \left(\omega^2 - \kappa^2\Omega^2\right)x &= \frac{f_x}{m} \\ \ddot{y} + 2\kappa\Omega\dot{x} + \kappa\dot{\Omega}x + \left(\omega^2 - \kappa^2\Omega^2\right)y &= \frac{f_y}{m} \end{aligned} \tag{2.40}$$

Since ideal MRIGs have no energy dissipation, they require no energy injection (i.e. control forces) once excited. Setting all the control forces to zeros in Eq. (2.40) yields the free response of ideal MRIGs

$$\begin{aligned} x &= a\cos\theta\cos\left(\omega t + \phi_0\right) - q\sin\theta\sin\left(\omega t + \phi_0\right) \\ y &= a\sin\theta\cos\left(\omega t + \phi_0\right) + q\cos\theta\sin\left(\omega t + \phi_0\right) \end{aligned} \tag{2.41}$$

It can be verified that, Eq. (2.41) is indeed the solution trajectory of ideal MRIGs, by substituting it into the dynamics Eq. (2.40). In Eq. (2.41), $\theta = \theta_0 - \kappa \int_0^t \Omega(\tau)\, d\tau$ is the pattern angle, a is the oscillation amplitude and q is the quadrature motion. a, q, θ_0 and ϕ_0 are determined from the initial deformations of the MRIG shell resonator.

The solution trajectory described by Eq. (2.41) is plotted in Fig. 2.10. It can be seen that the gyro's principal axis of vibration (semi-major axis of the ellipse) is precessing in the opposite direction to the input rate. The magnitude of the precession rate is proportional to the input rate by gain factor κ. Hence, the pattern angle is also called precession angle in this case. Aligning the initial precession angle θ_0 with zero yields

$$\theta = -\kappa \int_0^t \Omega(\tau)\, d\tau = -\kappa\theta_{ext} \tag{2.42}$$

That is, the precession angle is proportional to the input rotation angle θ_{ext}. As a result, measuring the input rotation angle is no more than detecting the precession angle θ of the gyro's principal axis of vibration, which can indeed be achieved by demodulating the x and y signals in Eq. (2.41). Notice that the magnitude of the input rate Ω is far smaller than the resonance frequency ω. Such a frequency divergence makes the low frequency precession angle separable from the high frequency x and y signals [87]. It is also worth mentioning that, the demodulation techniques in turn place a bandwidth limit on the input rate in order to achieve good Signal to Noise Ratio (SNR).

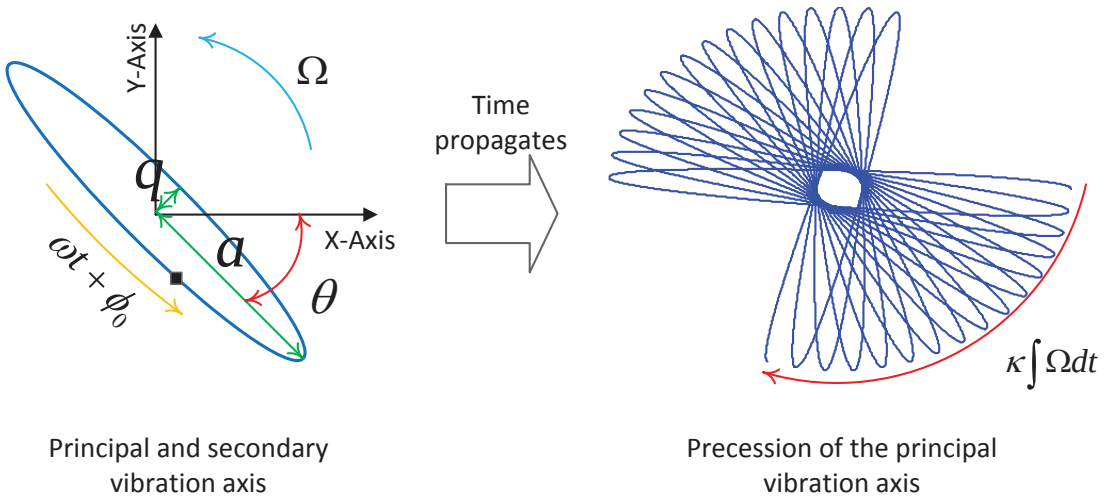

Figure 2.10: An ideal MRIG is a natural rate integrating gyro requiring no control action. The principal axis of vibration precess at a rate proportional to the input rate, at a constant amplitude and quadrature that are determined by shell initial states.

Notice that the precession angle shown in Fig. 2.10 does not represent the physical rotation angle of the vibration mode in a shell resonator. This is because the the primary and secondary vibration modes are not perpendicular as presented in Fig. 2.10, but intersect at an angle of 45 degrees. As shown in Fig. 2.11, the physical rotation angle of the vibration mode is half of the the precession angle demodulated from the readout signals x and y. However, since the precession angle immediately implies the external rotation angle, thus achieving the gyro goal, the physical rotation angle of the vibration mode is not of much interest.

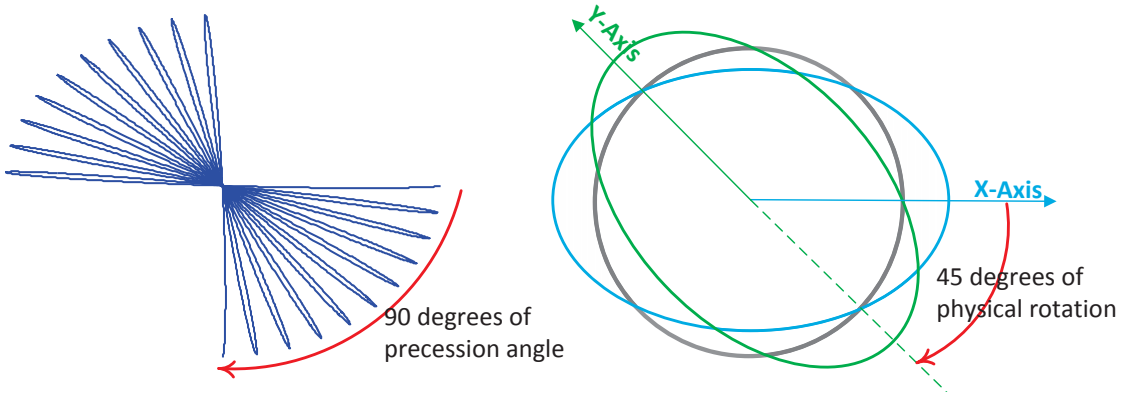

Figure 2.11: Physical rotation angle of the $n = 2$ vibration mode is half of the precession angle sensed from readout signals.

2.9 MRIG Control Objectives

As discussed in the preceding section, ideal MRIGs can persistently precess at a rate proportional to the input rate, requiring no control action. Hence, they are natural rate integrating gyroscopes. However, actual MRIGs usually do not behave in this manner. For example, the damping effect in the MRIG resonator will cause a constant energy loss and therefore the resonator will eventually stop vibrating. Even during the vibration phase, the damping mismatch $\Delta\left(\frac{1}{\tau}\right)$ and the frequency mismatch $\Delta\omega$ (see Eq. (2.12)) of the MRIG resonator will cause the gyro's principal axis of vibration not to precess correctly.

In this case, an active control scheme is required to enable the MRIG to operate in the rate integrating mode. As is the case of ideal MRIGs, a well controlled MRIG should have: (1) its vibration energy is maintained at a constant level; (2) its principal axis of vibration should precess at a rate proportional to the input rate and (3) the gyro should exhibit zero quadrature motion. Zero quadrature motion is preferred because it maximizes the Signal to Noise Ratio (SNR) when demodulating the sensed x and y signals. Fig. 2.12 depicts the desired trajectory of vibration for general MRIGs.

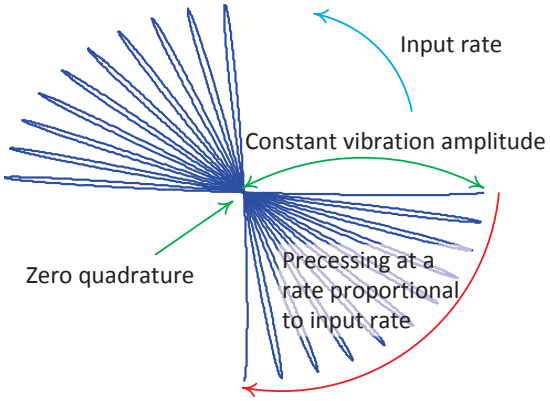

Figure 2.12: The desired trajectory of vibration for a general MRIG.

2.10 Summary

In this chapter, the basic configurations of MRIGs were presented. Topics covered included vibration modes of MRIG shell resonator, theory of electrostatic sensing and actuation, MRIG conditioning circuits and electrodes configurations. A comprehensive model of the $n = 2$ mode of vibration was derived by introducing an equivalent two dimensional harmonic oscillator. The derived model takes into account the stiffness mismatch and damping effect, provides the basic model for controller designs in the subsequent chapters. Then the class of ideal MRIGs was studied in detail to show the gyro precession, which is the fundamental principle of vibratory gyroscopes operating in the rate integrating mode. Finally, control objectives of general MRIGs were casted.

Chapter 3

A Linear Time Invariant Feedback Controller Design Approach for MRIGs

This chapter considers the feedback controller design for MRIGs. Three main control strategies have been developed so far for different types of gyroscopes. The first category of control strategies is the so called conventional mode of operation [60]. The basic idea behind this strategy is driving one of the vibration modes (i.e. the drive mode) to a known oscillatory motion and detecting the Coriolis acceleration coupled on the other vibration mode (i.e. the sense mode) [18]. Since the Coriolis acceleration is linear to the input rate by a known factor κ, the detected Coriolis acceleration immediately implies the input rate. The conventional mode of opertation can be classified into the open-loop mode and the closed-loop mode. The main difference between them is that in the latter one the sense mode is also actively controlled to zero while the former one is free to oscillate with no applied control force. In the open-loop mode of operation, the Coriolis acceleration couples the oscillations on drive mode to the sense mode. The resulting oscillation amplitude on the sense mode is proportional to that of drive mode. The proportional gain is linear to the input rate by a factor that is determined by the gyro characteristics like Q-factor, frequency mismatch, etc. [60, 1, 72] and [75]. Hence the input rate can be measured by detecting the oscillation amplitude on the sense mode. Since the open-loop mode of operation is very simple and easy to implement on circuitry, it has been widely used in MEMS rate gyroscopes. In the closed-loop mode of operation, the oscillation amplitude on the sense mode is continuously monitored and suppressed at zero by a feedback controller. Hence the closed-loop mode of operation is also called force-to-rebalance mode. In addition, the amount of control action used for suppressing the oscillation on sense mode is linear to the input rate [13]. Compared with open-loop mode of operation, the closed-loop strategy has much higher bandwidth [35]. Several variants based on the conventional mode of operation have been developed to address the issue of resolution [84, 81], bandwidth [2], oscillation amplitude[44, 53], frequency mismatch [43], quadrature error [18, 83, 61], time varying input rate [24], etc.

The second category of control strategies is Lyapunov method based adaptive controller [76, 56, 36, 23, 68, 59]. In this control scheme, the input rate is viewed as an unknown parameter like stiffness and damping shown in Eq. (2.12). A Lyapunov function candidate that is associated with the parameter estimation error, such as input rate estimation error and mismatch estimation error, and variables being controlled, such as energy, quadrature, is defined. Such a Lyapunov function has a negative semidefinite time derivative. Given the Barbalat's lemma and necessary persistence of excitation, it can be shown that the input rate estimation error converges to zero, thus achieving the goal of measuring the input rate. This type of control strategy usually requires accessing both gyro displacement and velocity. In those situations where the velocity is not measurable, an additional state observer is necessary [62].

The third category of control strategies is the method of averaging developed by Lynch [50]. It decomposes the whole system into fast dynamics and slow dynamics and utilizes a group of Proportional-Integral controllers to maintain the energy level and suppress the quadrature, which are both contained in the slow dynamics. Such an approach is able to operate in either rate or rate integrating mode [51]. When operating in the rate mode, an additional control loop called rate control loop is switched on, to actively monitor the orientation of the vibration axis and keep it at a preferred angle of orientation. If the preferred angle of orientation is set to zero, the controller is essentially the force-to-rebalance mode described in the conventional mode of operation. When operating in the rate integrating mode, the rate control loop is switched off, allowing the axis of vibration to freely precess at a rate proportional to the input rate. Since the axis of vibration can travel any angle, depending on the input rotation angle, the rate integrating mode is also called the whole angle mode. By providing fundamentally unlimited input range and measurement bandwidth, the whole angle mode has been widely used in conventional Hemispherical Resonator Gyroscopes (HRGs) [46, 48, 82, 49] and micromachined rate integrating gyroscopes [65, 81, 15, 27, 26] more recently. Variants of the method of averaging were also proposed to compensate for the parameter uncertainties in [45] and [28].

Among these three control strategies, the conventional and adaptive mode of operation are both rate measuring algorithms. The method of averaging, however, fits right into the control objectives of MRIGs. Hence, it is adopted in this dissertation as the starting point for subsequent controller designs. One limitation of the method of averaging is its nonlinearity, which complicates the controller design and analysis. In addition, it requires the gyroscope to be almost ideally polished and trimmed, in order to get rid of all mismatches [67]. Unfortunately, such gyroscope cannot yet be mass produced using micro-fabrication technologies. This chapter first briefly goes through the method of averaging, then presents a new demodulation method that can eliminate the nonlinearities that occurred in the conventional method of averaging. After this, the effect of mismatches is discussed. Compensation schemes for compensating the mismatches will be covered in the following chapters.

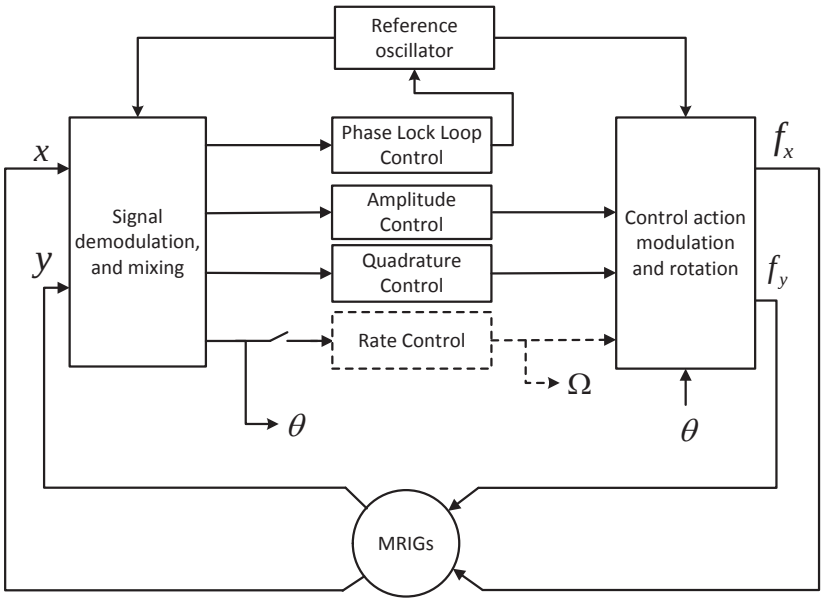

Figure 3.1: Block diagram of the method of averaging.

3.1 Review of Lynch's Method of Averaging

The method of averaging originally introduced by Lynch [50] decomposes the MRIG control objective into four sub control loops: an amplitude control loop, a quadrature control loop, a phase lock loop (PLL) and a rate control loop if the gyro is operating in the rate mode. The amplitude control loop attempts to maintain the vibration energy at a desired level. The quadrature control loop is designed to suppress the quadrature motion at zero. In addition, the method of averaging control scheme maintains a reference phase generator, which provides a reference phase for signal demodulation and control force modulation. A phase lock loop is utilized to synchronize the reference phase generator to the resonance frequency of $n = 2$ mode of vibration. The rate control loop can be switched on or off, depending on whether the rate or rate integrating mode is being activated. Fig. 3.1 shows the diagram of the method of averaging control scheme and its interaction with MRIGs.

3.1.1 Signal Demodulation and Mixing

The signal demodulation and mixing module is designated to extract the energy, quadrature and pattern angle from the sensed displacement signals x and y. Although imperfections like frequency and damping mismatches deviate the gyro trajectory from the ideal case described by Eq. (2.41), the resonance frequency ω does not change significantly. Hence, the sensed displacements in the x and y axes can be decomposed into components in phase and in quadrature with $(\omega t + \phi_0)$ as follows

$$\begin{aligned} x &= a\cos\theta\cos(\omega t+\phi_0) - q\sin\theta\sin(\omega t+\phi_0) \\ y &= a\sin\theta\cos(\omega t+\phi_0) + q\cos\theta\sin(\omega t+\phi_0) \end{aligned} \tag{3.1}$$

where a, q and θ are respectively the vibration amplitude, quadrature motion and the pattern angle (orientation angle) of the gyro's principal axis of vibration. In contrast to the ideal case, a, q are slowly varying over time and θ is not precessing at $-\kappa\Omega$. This form of representation is called canonical form. Variables a, q, ϕ_0 and θ are called canonical variables, as shown in Fig. 3.2. The solution in canonical form is essentially an ellipse with its orientation, semi-major axis and semi-minor axis that are slowly varying over time.

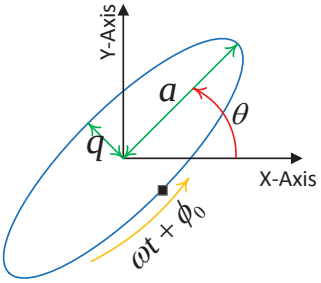

Figure 3.2: The MRIG canonical variables.

In order to extract the in phase and in quadrature components (the slowly varying components) in the sensed x and y signals, a group of intermediate variables are obtained by respectively multiplying the x and y signals by cosine and sine of the reference phase $\omega t+\phi$, which is generated by the reference phase generator.

$$\begin{aligned} x_c &= 2x\cos(\omega t+\phi) \\ x_s &= 2x\sin(\omega t+\phi) \\ y_c &= 2y\cos(\omega t+\phi) \\ y_s &= 2y\sin(\omega t+\phi) \end{aligned} \tag{3.2}$$

Then a low pass filter denoted by $G_{lpf}(s)$ is used to obtain the low frequency components in x_c, x_s, y_c and y_s

$$\begin{aligned} \hat{c}_x &= G(s)[x_c] &&= G(s)[c_x + a_1\sin(2\omega t+\phi_1)] \\ \hat{s}_x &= G(s)[x_s] &&= G(s)[s_x + a_2\sin(2\omega t+\phi_2)] \\ \hat{c}_y &= G(s)[y_c] &&= G(s)[c_y + a_3\sin(2\omega t+\phi_3)] \\ \hat{s}_y &= G(s)[y_s] &&= G(s)[s_y + a_4\sin(2\omega t+\phi_4)] \end{aligned} \tag{3.3}$$

where $a_1, a_2, a_3, a_4, \phi_1, \phi_2, \phi_3$ and ϕ_4 are determined by a, q, θ, ϕ_0. Their exact values are not of interest as they are usually eliminated by the low pass filter. c_x, s_x, c_y and s_y are respectively the in phase and in quadrature components of channel x and y, and defined as follows

$$\begin{aligned} c_x &:= a\cos\theta\cos\delta\phi + q\sin\theta\sin\delta\phi \\ s_x &:= a\cos\theta\sin\delta\phi - q\sin\theta\cos\delta\phi \\ c_y &:= a\sin\theta\cos\delta\phi - q\cos\theta\sin\delta\phi \\ s_y &:= a\sin\theta\sin\delta\phi + q\cos\theta\cos\delta\phi \end{aligned} \tag{3.4}$$

where $\delta\phi = \phi - \phi_0$ is the phase reference error that should be eliminated by the phase lock loop. It can be seen that c_x, c_y, s_x and s_y are slowly time varying variables, hence they can be effectively separated from the high frequency components at 2ω by the low pass filter $G_{lpf}(s)$. Therefore, $\hat{c}_x, \hat{s}_x, \hat{c}_y$ and $\hat{s}_y$ in Eq. (3.3) can be interpreted as the estimate of c_x, s_x, c_y and s_y respectively.

Notice that the system energy E, quadrature Q, pattern angle θ and phase reference error $\delta\phi$ are related to Eq. (3.4) as follows

$$\begin{aligned} E &:= a^2 + q^2 = c_x^2 + s_x^2 + c_y^2 + s_y^2 \\ Q &:= 2aq = 2(c_x s_y - c_y s_x) \\ R &:= (a^2 - q^2)\cos 2\theta = c_x^2 + s_x^2 - c_y^2 - s_y^2 \\ S &:= (a^2 - q^2)\sin 2\theta = 2(c_x c_y + s_x s_y) \\ L &:= (a^2 - q^2)\sin 2\delta\phi = 2(c_x s_x + c_y s_y) \end{aligned} \tag{3.5}$$

where R and S are two variables that respectively represents the cosine and sine of 2θ, and L is a variable that represents the phase reference error. Notice that the definition of L only takes the imaginary part from that of Eq. (31) in [50] because only the imaginary part is used in the subsequent controller design. In practice, the energy, quadrature, pattern angle and reference phase error are computed from the estimate of c_x, c_y, s_x and s_y

$$\begin{aligned} \hat{E} &= \hat{c}_x^2 + \hat{s}_x^2 + \hat{c}_y^2 + \hat{s}_y^2 \\ \hat{Q} &= 2(\hat{c}_x\hat{s}_y - \hat{c}_y\hat{s}_x) \\ \hat{R} &= \hat{c}_x^2 + \hat{s}_x^2 - \hat{c}_y^2 - \hat{s}_y^2 \\ \hat{S} &= 2(\hat{c}_x\hat{c}_y + \hat{s}_x\hat{s}_y) \\ \hat{\theta} &= \frac{1}{2}\tan^{-1}\left(\frac{\hat{S}}{\hat{R}}\right) \\ \hat{L} &= 2(\hat{c}_x\hat{s}_x + \hat{c}_y\hat{s}_y) \end{aligned} \tag{3.6}$$

Since $\hat{c}_x, \hat{s}_x, \hat{c}_y$ and $\hat{s}_y$ are respectively the filtered version of c_x, s_x, c_y and s_y,

$$\begin{aligned} \hat{L} &= 2\left\{\left(G_{lpf}(s)\left[c_x\right]\right)\left(G_{lpf}(s)\left[s_x\right]\right) + \left(G_{lpf}(s)\left[c_y\right]\right)\left(G_{lpf}(s)\left[s_y\right]\right)\right\} \\ L &= 2(c_x s_x + c_y s_y) \end{aligned} \tag{3.7}$$

It can be seen that the relation between L and its estimate $\hat{L}$ (and also for energy E, quadrature Q, variable R and S) is in general nonlinear. However, when the controller gains are set to low values, c_x, s_x, c_y and s_y only contain low frequency components that the low pass filter will not show an effect. As a consequence, the estimate of the in phase components, in quadrature components, energy, quadrature and pattern angle can be considered as their real values.

3.1.2 Control Action Modulation and Rotation

Part of the control objectives are to maintain the system energy while suppressing the quadrature. However, as shown in Fig. 3.2, the amplitude axis and quadrature axis are rotated from the x and y axes where the control forces are applied, by the pattern angle θ. In order to control the amplitude and quadrature independently, it is necessary to rotate the control forces by the same angle, as shown in Fig. 3.3. Mathematically,

$$\begin{aligned} f_x &= F_a \cos\theta - F_q \sin\theta \\ f_y &= F_a \sin\theta + F_q \cos\theta \end{aligned} \tag{3.8}$$

where F_a and F_q are respectively the effective forces for amplitude and quadrature.

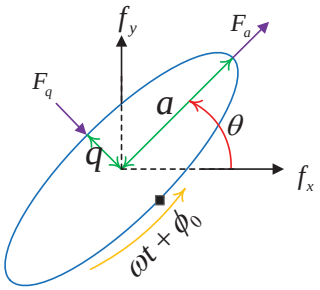

Figure 3.3: MRIG canonical variables and control forces.

Moreover, in order to excite the $n = 2$ mode of vibration, which is at the resonance frequency of ω, the control force needs to be at the same frequency. This can be achieved by modulating the control forces onto the frequency of ω. Mathematically,

$$\begin{aligned} F_a &= f_{a_c} \cos(\omega t + \phi) + f_{a_s} \sin(\omega t + \phi) \\ F_q &= f_{q_c} \cos(\omega t + \phi) + f_{q_s} \sin(\omega t + \phi) \end{aligned} \tag{3.9}$$

where $f_{a_c}, f_{a_s}, f_{q_c}$ and f_{q_s} are respectively the effective forces on amplitude and quadrature axes, in phase and in quadrature with the reference phase generator. As is the case of $E, Q, \delta\phi$ and θ, $f_{a_c}, f_{a_s}, f_{q_c}$ and f_{q_s} are also slowly time varying variables. Recall that $\omega t + \phi$ in Eq. (3.9) is the reference phase generated by the reference phase generator.

3.1.3 Dynamics of the Controlled Variables

In this section, the approximate dynamics between the control inputs $f_{a_c}, f_{a_s}, f_{q_c}$ and f_{q_s}, and the averaged outputs E, Q, θ and $\delta\phi$ is established following the results in [50]. This is achieved by substituting Eq. (3.5) into Eq. (3.1); Eq. (3.1) into the left hand side of Eq. (2.12); Eq. (3.9) into Eq. (3.8), Eq. (3.8) into the right hand side of Eq. (2.12) and equating the components of x and y, in phase and in quadrature with the $\omega t + \phi$, on both side of the Eq. (2.12) (see Eq. (40) of [50]).

$$\begin{aligned}
\dot{E} &= -\left[\frac{2}{\tau} + \Delta\left(\frac{1}{\tau}\right)\cos 2(\theta - \theta_\tau)\right] E - \frac{\sqrt{E}}{\omega} f_{a_s} \\
\dot{Q} &= -\frac{2}{\tau} Q \;-\; \Delta\omega \sin 2(\theta - \theta_\omega) E \;+\; \frac{\sqrt{E}}{\omega} f_{q_c} \\
\dot{\theta} &= -\kappa\Omega + \frac{1}{2}\Delta\left(\frac{1}{\tau}\right)\sin 2(\theta - \theta_\tau) + \frac{1}{2}\Delta\omega\cos 2(\theta - \theta_\omega)\frac{Q}{E} - \frac{f_{q_s}}{2\omega\sqrt{E}} \\
\dot{\delta\phi} &= \dot{\phi} + \frac{1}{2}\Delta\omega\cos 2(\theta - \theta_\omega) + \frac{1}{2}\Delta\left(\frac{1}{\tau}\right)\sin 2(\theta - \theta_\tau)\frac{Q}{E} + \frac{f_{a_c}}{2\omega\sqrt{E}}
\end{aligned} \tag{3.10}$$

where the control actions for E, Q, θ and $\delta\phi$ are respectively $f_{a_s}, f_{q_c}, f_{q_s}$ and f_{a_c}.

3.1.4 Controller Design

Eq. (3.10) are the state equations for the vibration energy, quadrature motion, pattern angle and phase reference error. As proposed in [50], a group of Proportional Integral (PI) feedback controllers can be used to respectively maintain the oscillation energy, suppress the quadrature motion and eliminate the phase reference error. When the gyro is operating in the whole angle mode, the pattern angle is free to precess, requiring no feedback control action

$$\begin{aligned}
f_{a_s} &= K_E\left[(E - E_0) + \frac{1}{2\tau_E}\int_0^t (E(\tau) - E_0)\, d\tau\right] \\
f_{q_c} &= -K_Q\left[Q + \frac{1}{2\tau_Q}\int_0^t Q(\tau) d\tau\right] \\
f_{q_s} &= 0 \\
f_{a_c} &= 0 \\
\dot{\phi} &= -K_L\left[L + \frac{1}{2\tau_L}\int_0^t L(\tau) d\tau\right], \text{where} \;\; L = (a^2 - q^2)\sin 2\delta\phi
\end{aligned} \tag{3.11}$$

Transition from the whole angle mode to the rate mode is accomplished by enabling the rate control loop, which actively maintains the orientation of the vibration axis at a desired angle θ_0

$$f_{q_s} = K_S\left[(\theta - \theta_0) + \frac{1}{2\tau_S}\int_0^t (\theta(\tau) - \theta_0)\, d\tau\right] \tag{3.12}$$

3.2 A Linear Time Invariant Feedback Controller Design Approach for MRIGs

It has been pointed out in preceding sections that the relation between the real energy, quadrature, phase reference error and their estimates are in general nonlinear. Such a nonlinearity limits the controller bandwidth and moreover makes the design and analysis of more sophisticated controllers, that are used to address the issue of mismatch, noise, etc. more difficult.

In this section, an alternative demodulation scheme is proposed, which results in linear energy, quadrature and phase lock loop dynamics. Based on these liner dynamics, a number of tools from well studied linear systems thereby can be utilized to design the controllers and analyze the performance of MRIGs. Such a methodology also enables the use of more sophisticated strategies, beyond the Proportional-Integral (PI) controller proposed in Lynch's paper [50].

3.2.1 A New Demodulation Scheme

As shown in Eq. (3.7), the nonlinearity in the conventional method of averaging lies in the product between two filtered signals. Hence, in order to eliminate such a nonlinearity, the basic idea behind the new demodulation scheme is, exchanging the order between multiplication and low pass filtering. First, signals x_c, x_s, y_c and y_s in Eq. (3.2) are manipulated as follows, to produce the energy, cosine and sine of pattern angle, and phase reference error signals that are contaminated by some high frequency noise, which will be filtered subsequently.

$$\begin{array}{rcl} E_h & = & \frac{x_c^2+x_s^2+y_c^2+y_s^2}{2} \\ R_h & = & \frac{x_c^2+x_s^2-y_c^2-y_s^2}{2} \\ S_h & = & x_c y_c + x_s y_s \\ L_h & = & 2(x_c x_s + y_c y_s) \end{array} \tag{3.13}$$

As shown in Appendix A, these variables are related to E, R, S and L as follows

$$\begin{array}{rcl} E_h & = & E + a_E \sin(2\omega t + \phi_E) \\ R_h & = & R + a_R \sin(2\omega t + \phi_R) \\ S_h & = & S + a_S \sin(2\omega t + \phi_S) \\ L_h & = & L + a_L^1 \sin(2\omega t + \phi_L^1) + a_L^2 \sin(4\omega t + \phi_L^2) \end{array} \tag{3.14}$$

where $a_E, a_R, a_S, a_L^1, a_L^2, \phi_E, \phi_R, \phi_S, \phi_L^1$ and ϕ_L^2 are determined by a, q, θ, ϕ_0 and ϕ. Again, their exact values are not of interest because these signals will be eliminated by the subsequent low pass filtering. These residual signals after low pass filtering are at the same frequency of 2ω or 4ω and are called nuisance noise.

Then a low pass filter denoted by $G_{lpf}(s)$ is utilized to extract the low frequency energy, pattern angle and phase reference error

$$\begin{array}{rcl} \hat{E} & = & G_{lpf}(s)\,[E_h] \\ \hat{R} & = & G_{lpf}(s)\,[R_h] \\ \hat{S} & = & G_{lpf}(s)\,[S_h] \\ \hat{\theta} & = & \frac{1}{2}\tan^{-1}\left(\frac{\hat{S}}{\hat{R}}\right) \\ \hat{L} & = & G_{lpf}(s)\,[L_h] \end{array} \tag{3.15}$$

The quadrature can be determined as follows

$$\begin{array}{rcl} Q_h & = & 2(y_c y_s - x_c x_s)\sin 2\hat{\theta} + 2(x_s y_c + x_c y_s)\cos 2\hat{\theta} \\ \hat{Q} & = & G_{lpf}\,[Q_h] \end{array} \tag{3.16}$$

As shown in Appendix A, assuming the convergence of the phase lock loop (i.e. $\delta\phi = 0$) and the correct pattern angle estimate (i.e. $\hat{\theta} = \theta$), the quadrature estimate is essentially the real quadrature filtered by the low pass filter G_{lpf}.

$$Q_h = Q + a_Q \sin(4\omega t + \phi_Q) \tag{3.17}$$

In summary, the new demodulation scheme has related the real energy, quadrature and phase reference error to their estimates by the low pass filter G_{lpf}, which is a linear time invariant system. Hence, the resulting energy control loop, quadrature control loop and phase lock loop all have linear dynamics.

3.2.2 Demonstration on Ideal MRIGs

In this section, the proposed demodulation scheme is verified by demonstrating the phase lock loop on ideal MRIGs. Recall the solution of ideal MRIGs

$$\begin{array}{rcl} x & = & a\cos(\theta)\cos(\phi) - q\sin(\theta)\sin(\phi) \\ y & = & a\sin(\theta)\cos(\phi) + q\cos(\theta)\sin(\phi) \\ & & \theta = \theta_0 - \kappa\int_{t_0}^{t}\Omega d\tau \\ & & \phi = \omega t + \phi_0 \end{array} \tag{3.18}$$

Since ideal MRIGs have no energy dissipation, requiring no energy or quadrature control loop, only the phase lock loop in Eq. (3.11) needs to be enabled, in order to estimate the resonance frequency, oscillation phase, amplitude, quadrature and precession angle. Also note that the phase lock loop runs inside the controller, sending no control action to the gyroscope. Hence, the control forces f_x and f_y are essentially zeros. The low pass filter used in this example is a first order Butterworth filter [12, 8].

$$G_{lpf}(s) = \frac{1}{1 + \frac{s}{\omega_c}} \tag{3.19}$$

where ω_c is the corner frequency.

Parameters for the MRIG and phase lock loop are summarized in Table 3.1.

Table 3.1: Parameters for the simulated MRIG and phase lock loop

Symbol	Description	Value	Unit
ω	Resonance frequency	10000	Hertz
Ω	Input rate	1	Hertz
κ	Gain factor	1	N/A
a	Amplitude	1.0	Microns
q	Quadrature	0.1	Microns
θ_0	Initial precession phase	0	Radians
ϕ_0	Initial oscillation phase	0	Radians
ω_n	Nominal frequency	10010	Hertz
K_P	Proportional gain	60	N/A
K_I	Integral gain	2030	N/A
ω_c	Corner frequency	100	Hertz

Fig. 3.4 shows the phase lock loop response. It can be seen that the PLL converges to the real resonance frequency (upper left figure); reference phase generated by the phase reference generator converges to the real oscillation phase (upper right figure); and energy, quadrature converge to their correct values as shown by lower figures. The small DC bias between the measured precession angle and its real value is caused by the phase delay of the low pass filter. In particular, the upper right figure shows good match to the model predicted response, except a slight difference taking place when the phase error becomes large. This residual nonlinearity comes from the sine function in $L = \sin 2\delta\phi$, which essentially distorted the linear gain and slowed down the system response. Another interesting phenomenon to observe is the quadrature estimate as shown in the lower left figure. It can be seen that there is a significant transient distortion before converging to the true value. This is because of the transient response of the PLL (note that the distortion on $\hat{Q}$ takes place at the same time as $\hat{L}$). However, such a transient distortion is not a problem in gyro control since the phase lock loop converges much faster than the quadrature loop. Note that the PLL runs inside the controller, involving no physical control actions, thus it is not susceptible to any channel delays, gain mismatches, etc. Hence, gains for the PLL can usually be set to large values that result in a fast-converging phase lock loop.

In order to show the superiority of the new demodulation scheme over the conventional one, the stability of the two methods is investigated. Since the new demodulation scheme results in a linear phase lock loop, the Routh-Hurwitz [40] criterion can be utilized to determine its stability. It can be shown that the characteristic polynomial of the phase lock loop is

$$C(s) = \frac{1}{\omega_c}s^3 + s^2 + 2(a^2 - q^2)K_P s + 2(a^2 - q^2)K_I \tag{3.20}$$

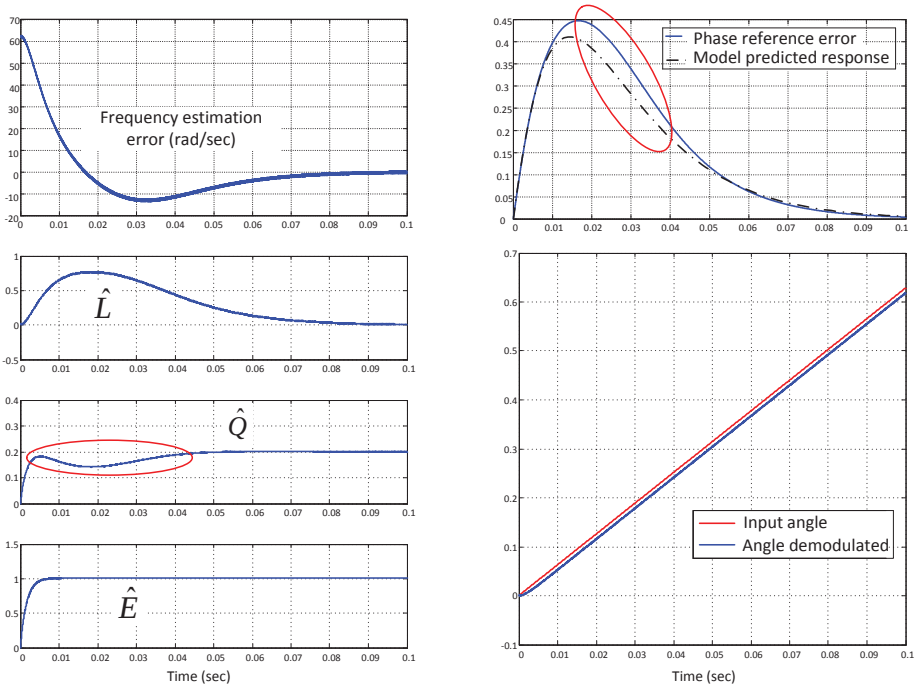

Figure 3.4: Demonstration of the phase lock loop on an ideal MRIG, using the new demodulation scheme.Upper figures show the estimation error of the oscillation frequency and phase; Lower figures show the time response of the demodulation variables: phase reference error, quadrature, energy and pattern angle.

By the Routh-Hurwitz criterion, the sufficient and necessary condition for a stable phase lock loop is

$$\omega_c K_P > K_I > 0 \tag{3.21}$$

Fig. 3.5 shows the empirical stability versus the stability criterion over different K_P and K_I values, on both demodulation schemes. Empirical stability is obtained by simulating the system with sufficient long time and observing whether the PLL blows up or not. It can be seen that for the new demodulation scheme, the empirical stability fits right into the Routh-Hurwitz stability criterion. The conventional demodulation scheme, on the other hand, has many unstable points crossing the stability boundary predicted by Routh-Hurwitz criterion, hence providing a more conservative and unpredictable stability margin. In addition, the new demodulation scheme's performance, such as noise rejection, disturbance attenuation, etc., is predictable by linear system theory while the conventional scheme has no system theoretic performance guarantees.

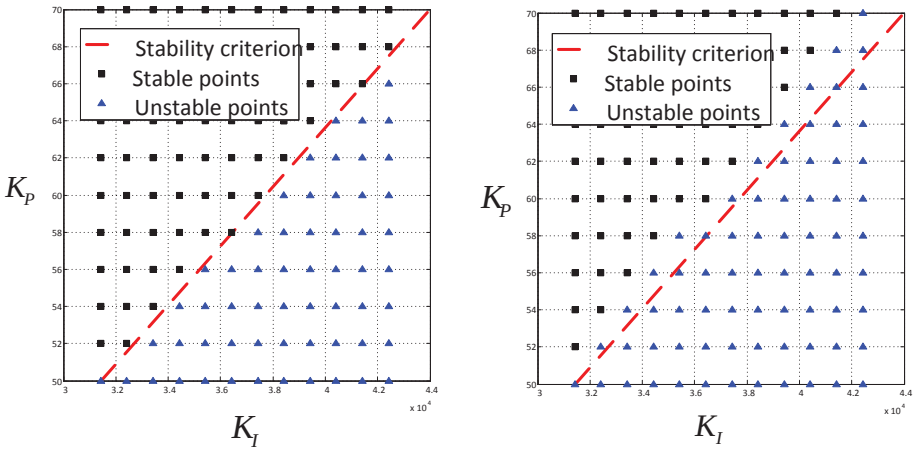

Figure 3.5: Empirical stability over different K_P and K_I values, for the new demodulation scheme (left) and the conventional demodulation scheme (right).

3.2.3 The Gyro Phase Lock Loop

Recall that the phase reference error $\delta\phi$, which is defined as

$$\delta\phi := \phi - (\omega t + \phi_0) \tag{3.22}$$

where $\omega t + \phi_0$ is the real oscillation phase while ϕ is the reference phase put out by the reference phase generator, is subject to

$$\dot{\delta\phi} = \dot{\phi} - \omega + \frac{1}{2}\Delta\omega\cos 2(\theta - \theta_\omega) + \frac{1}{2}\Delta\left(\frac{1}{\tau}\right)\sin 2(\theta - \theta_\tau)\frac{Q}{E} + \frac{f_{a_c}}{2\omega\sqrt{E}} \tag{3.23}$$

In the method of averaging scheme proposed in [50], f_{a_c} is set to zero. The phase reference error is eliminated by adjusting the phase estimate inside the controller

$$\dot{\phi} = -K_p^L\hat{L} - K_i^L\int\hat{L}d\tau + \omega_n \tag{3.24}$$

where K_p^L and K_i^L are respectively the proportional and integral gains for the phase lock loop; ω_n is the nominal resonance frequency, which is characterized prior to the gyro operation; $\hat{L}$ is the phase reference error computed by

$$\hat{L} \;=\; G_{lpf}(s)\,[L_h] \tag{3.25}$$

Fig. 3.6 shows the system interconnections. Parameters in this figure are summarized in Table 3.2. It can be seen that such a system is almost a LTI system except the $\sin 2x$ component, which is nonlinear, and the output gain $g_L = a^2 - q^2$, which is time varying, being adjusted by the energy and quadrature control loops.

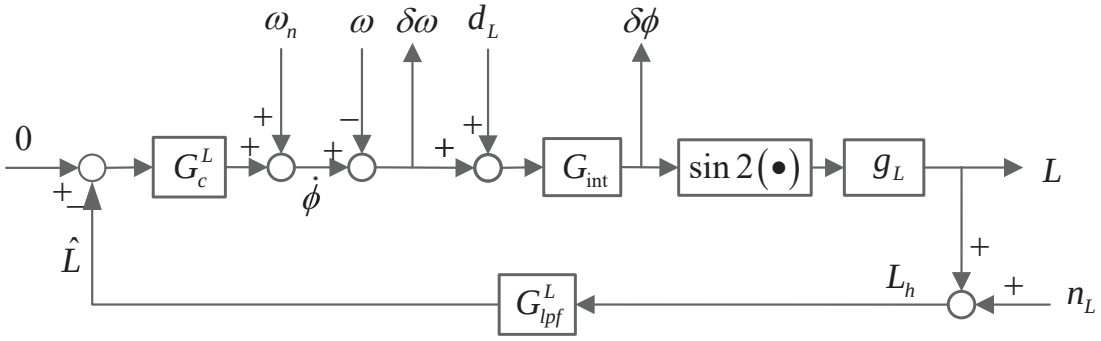

Figure 3.6: Block diagram of the phase lock loop

Table 3.2: Summary of Signals and Symbols in Fig. 3.6

Symbol	Description	Comments
G_{int}	Integrator	$G_{int}(s) = \frac{1}{s}$
g_L	Output gain	$g_L = a^2 - q^2$
G_c^L	PI Controller for PLL	$G_c^L(s) = K_p^L + K_i^L \frac{1}{s}$
G_{lpf}^L	Low Pass filter for PLL	N/A
d_L	Mismatch disturbance	$d_L = \frac{1}{2}\Delta\omega \cos 2(\theta - \theta_\omega)$ $+ \frac{1}{2}\Delta\left(\frac{1}{\tau}\right) \sin 2(\theta - \theta_\tau)\frac{Q}{E}$
n_L	Measurement noise	$n_L = a_L^1 \sin(2\omega t + \phi_L^1)$ $+a_L^2 \sin(4\omega t + \phi_L^2)$
ω_n	Nominal frequency	N/A
$\omega_n - \omega$	Frequency bias	DC bias
$\delta\omega$	Frequency estimation error	$\delta\omega = \dot{\phi} - \omega$
$\delta\phi$	Phase estimation error	N/A

In most cases, the stability and steady performance, such as disturbance and noise rejection, are of concern when designing the PLL. This can be analyzed using linear system theory, by approximating $\sin 2x$ with $2x$. In addition, under ideal operating conditions, $q \approx 0$, it is reasonable to approximate g_L with E_0, which is the desired energy level. The resulting disturbance and noise rejection functions are

$$G_{d2L} = \frac{G_p^L}{1 + G_{lpf} G_c^L G_p^L} \tag{3.26}$$

$$G_{n2L} = \frac{G_{lpf} G_c^L G_p^L}{1 + G_{lpf} G_c^L G_p^L} \tag{3.27}$$

where $G_p^L = 2E_0 G_{int}$ is viewed as the system plant to be controlled.

It can be seen from the disturbance and noise rejection functions that, (1) Disturbances degrade the phase reference error via the system sensitivity function. Since the disturbances that contain the DC bias $\omega_n - \omega$ and the mismatch induced disturbance d_L, are concentrated on the low frequency range, a relative large proportional and integral gains are suggested, in order to achieve large attenuation over the low frequency range on the sensitivity function. (2) Noise degrades the phase reference error via the complementary sensitivity function. Since the complementary sensitivity function has a very large attenuation gain over the high frequency range due to the low pass filter, the noise can be effectively eliminated. Also note that the noise is at a known frequency of 2ω and 4ω, notch filters can be utilized to achieve improved filtering performance [90].

The disturbance and noise rejection for the frequency estimation error are

$$G_{d2\delta\omega} = \frac{G_{lpf}G_c^L G_p^L}{1 + G_{lpf}G_c^L G_p^L} \tag{3.28}$$

$$G_{n2\delta\omega} = \frac{G_{lpf}G_c^L}{1 + G_{lpf}G_c^L G_p^L} \tag{3.29}$$

It can be seen that the DC disturbance $\omega_n - \omega$ affects the frequency estimation error via the system sensitivity function, which has a significant low gain at the low frequency range. Hence the initial bias on frequency estimate causes no steady error; However, the frequency mismatch induced disturbance d_L degrades the frequency estimate via the complementary sensitivity function, which has gain of one at the low frequency range. Therefore, the frequency mismatch will cause the frequency estimate to oscillate around its real value, the oscillation amplitude is $\frac{1}{2}\Delta\omega$, as indicated by Eq. (3.10);

3.2.4 The Gyro Energy Loop

Recall that the dynamics of the gyro's averaged energy is given by

$$\dot{E} = -\left[\frac{2}{\tau} + \Delta\left(\frac{1}{\tau}\right)\cos 2(\theta - \theta_\tau)\right] E - \frac{\sqrt{E}}{\omega} f_{a_s} \tag{3.30}$$

and the proposed energy controller in the method of averaging [50] is

$$f_{a_s} = K_p^E \left(E - E_0\right) + K_i^E \int_0^t \left(E(\tau) - E_0\right) d\tau \tag{3.31}$$

The resulting close loop system interconnection is shown in Fig. 3.7. Parameters are summarized in Table 3.3. When designing the controller, the output gain is set to its nominal value $\frac{\sqrt{E_0}}{\omega}$ and the damping mismatch $\Delta\left(\frac{1}{\tau}\right)$ is set to zero. This technique consequently produces a LTI system with a gain mismatch on the output channel and a variation on the system loop transfer function's pole. Such a gain mismatch and pole variation can, however, be easily analyzed in frequency domain when designing the feedback controller.

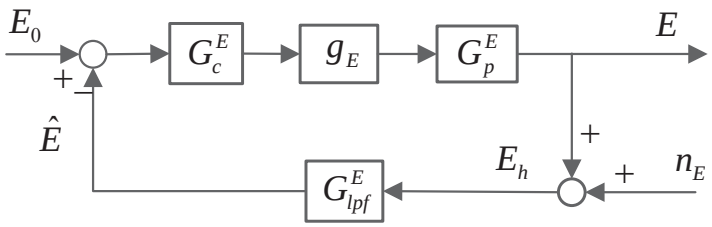

Figure 3.7: Block diagram of the energy control loop

Table 3.3: Summary of Signals and Symbols in Fig. 3.7

Symbol	Description	Comments
G_p^E	Controlled Plant	$G_p^E = \frac{1}{s+\frac{2}{\tau}+\Delta\left(\frac{1}{\tau}\right)\cos 2(\theta-\theta_\tau)}$
g_E	Output gain	$g_E = \frac{\sqrt{E}}{\omega}$
G_c^E	PI Controller for energy loop	$G_c^E(s) = K_p^E + K_i^E \frac{1}{s}$
G_{lpf}^E	Low Pass filter for energy loop	N/A
n_E	Measurement noise	$n_E = a_E \sin(2\omega t + \phi_E)$

3.2.5 The Gyro Quadrature Loop

Recall that the quadrature dynamics is given by

$$\dot{Q} = -\frac{2}{\tau}Q \; - \; \Delta\omega \sin 2(\theta - \theta_\omega)E \; + \; \frac{\sqrt{E}}{\omega} f_{q_c} \tag{3.32}$$

The quadrature dynamics differs from the energy dynamics in that the mismatch disturbs the quadrature as an external disturbance instead of altering its damping. The resulting system block diagram is shown in Fig. 3.8 with parameters summarized in Table 3.4. Again, the output gain g_Q is set to $\frac{\sqrt{E_0}}{\omega}$ in order to produce a LTI system. Lumping the output gain $\frac{\sqrt{E_0}}{\omega}$ into the system plant yields the disturbance attenuation transfer function for quadrature control loop

$$G_{d2Q} = \frac{G_p^Q}{1 + G_c^Q G_p^Q G_{lpf}^Q} \tag{3.33}$$

Similar to the phase lock loop (PLL), the disturbance, usually induced by frequency mismatch, affects the quadrature via the system sensitivity function. However, since the control action for quadrature is applied to the gyro resonator via physical actuator (i.e. electrostatic actuation mechanism), controller gains are usually set to low values in order to attain sufficient robustness. The resulting bandwidth is much smaller than that of the PLL. As a consequence, a significant disturbance resides in quadrature and degrades the gyro performance.

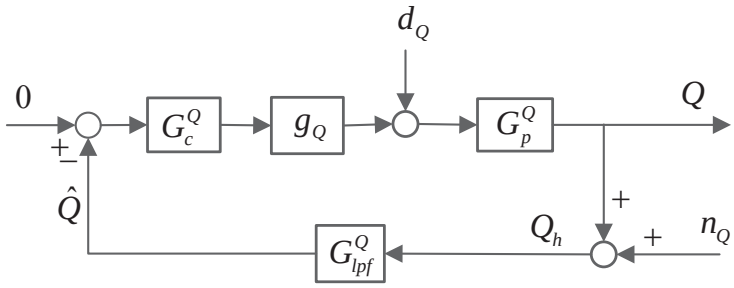

Figure 3.8: Block diagram of the quadrature control loop

Table 3.4: Summary of Signals and Symbols in Fig. 3.8

Symbol	Description	Comments
g_Q	Output gain	$g_Q = \frac{\sqrt{E_0}}{\omega}$
G_p^Q	Controlled Plant	$G_p^Q = \frac{1}{s+\frac{2}{\tau}}$
G_c^Q	PI Controller for quadrature loop	$G_c^Q(s) = K_p^Q + K_i^Q \frac{1}{s}$
G_{lpf}^Q	Low Pass filter for quadrature loop	N/A
d_Q	Mismatch disturbance	$d_Q = -\Delta\omega \sin 2(\theta - \theta_\omega)E$

3.3 Effects of Mismatch On the Feedback Controller

When the gyro resonator is ideally fabricated with identical primary and secondary modes of vibration, as shown in Eq. (3.10), the feedback controller presented in preceding sections can effectively compensate the energy dissipation, suppress the quadrature and produce a precession rate on the principal axis of vibration. However, actual MRIGs usually have asymmetric primary and secondary vibration modes, which produce significant damping and frequency mismatches, as shown in Eq. (2.12). Since the frequency and damping mismatch behave as disturbances, they can, in principle, be attenuated by the feedback controller discussed in preceding sections. The amount of attenuation is determined by the controller gains. However, feedback controller gains, especially those in the energy and quadrature controllers, are usually set to low values, in order to gain sufficient robustness. This results in a poor disturbance rejection performance.

As shown in the energy dynamics in Eq. (3.30), the damping mismatch $\Delta\left(\frac{1}{\tau}\right)$ alters the damping ratio of the energy loop. Variations in the damping ratio do not change the steady energy level, but either prolong or shorten the transient response. As a consequence, the vibration energy can be effectively maintained at the desired level by the feedback controller in spite of the damping mismatches. For the quadrature dynamics in Eq. (3.32), the frequency mismatch $\Delta\omega$ introduces an external disturbance at the frequency of $2\kappa\Omega$. This causes the quadrature to oscillate around zero, at the frequency of $2\kappa\Omega$.

The effect of mismatches on pattern angle response is more complicated than that of quadrature and energy. Recall that the pattern angle dynamics is given by

$$\dot{\theta} = -\kappa\Omega + \frac{1}{2}\Delta\left(\frac{1}{\tau}\right)\sin 2(\theta - \theta_\tau) + \frac{1}{2}\Delta\omega\cos 2(\theta - \theta_\omega)\frac{Q}{E} - \frac{f_{q_s}}{2\omega\sqrt{E}} \tag{3.34}$$

First, the damping mismatch $\Delta\left(\frac{1}{\tau}\right)$ introduces an external disturbance at the frequency of $2\kappa\Omega$, with an amplitude of $\frac{1}{2}\Delta\left(\frac{1}{\tau}\right)$. Such a sinusoidal disturbance causes the pattern angle to oscillate around the input rotation angle. In addition, since both $\cos 2(\theta - \theta_\omega)$ and Q are oscillating at the frequency of $2\kappa\Omega$, the mismatch term $\frac{1}{2}\Delta\omega\cos 2(\theta-\theta_\omega)\frac{Q}{E}$ in Eq. (3.34) produces a DC bias on the precession rate. This in turn results in a ramp drift in the precession angle. Finally, when the damping mismatch $\Delta\left(\frac{1}{\tau}\right)$ is larger than $2\kappa\Omega$, the precession angle θ stalls at one of $\theta_\tau + \frac{1}{2}\left[2m\pi + \sin^{-1}\frac{2\kappa\Omega}{\Delta\left(\frac{1}{\tau}\right)}\right]$ or $\theta_\tau + \frac{1}{2}\left[2m\pi + \pi - \sin^{-1}\frac{2\kappa\Omega}{\Delta\left(\frac{1}{\tau}\right)}\right]$, as shown in Lemma 1, Appendix B. As a consequence, the gyro's principal axis of oscillation fails to precess. The stall condition in turn places a lower bound on the input rate for the gyro to operate in the rate integrating mode.

$$|\Omega| > \left|\frac{\Delta\left(\frac{1}{\tau}\right)}{2\kappa}\right| \tag{3.35}$$

3.4 Simulation Study

3.4.1 Simulation Setup

In this section, a simulation study is performed on a MRIG model to verify the efficacy of the new demodulation scheme and the effects of mismatches. The simulated MRIG model parameters are drawn from an actual MRIG fabricated by Honeywell, as shown in Table 3.5

3.4.2 Warm Start

The transient response of the energy control loop usually causes a phase delay on the gyro precession. This is because the gyro's vibration axis does not precess correctly until gaining a sufficient level of energy. In this section, we will start measuring the external rotation angle only after the gyro has gained a sufficiently large oscillating energy level.

3.4.3 Phase Delay Compensation for Pattern Angle

As discussed in previous sections, the pattern angle is demodulated from the sensed x and y signals via a low pass filter. An implementable low pass filter always has a small amount of phase delay over the low frequency range where the input rate lies. As a consequence, the

Table 3.5: Parameters for the simulated MRIG

Symbol	Description	Value	Unit
ω	Resonance frequency	8082	Hertz
κ	Gain factor	1	N/A
$\frac{1}{\tau}$	Decay rate	0.9494	sec^{-1}
Ω	Input rate	10	Hertz
f_s	Sampling frequency	96000	Hertz
$\Delta\omega$	Frequency mismatch	10	Hertz
θ_ω	Azimuthal angle of stiffness axes	0.3	Radians
$\Delta(\frac{1}{\tau})$	Decay rate	0.1402	sec^{-1}
θ_τ	Azimuthal angle of damping axes	0.2	Radians
ω_n	Nominal resonance frequency	8077	Hertz

measured pattern angle is delayed from the real one by an amount that depends on the low pass filter being used. Such a delay can be compensated by estimating the input rate $\widehat{\Omega}$ and correcting the currently measured pattern angle by an amount of $\angle G_{lpf}(j2\kappa\widehat{\Omega})$.

It can be seen that, compensating the phase delay in the pattern angle requires the knowledge of input rate, which can be estimated in real time, using a recursive least square algorithm [89]. The forgetting factor in the estimation algorithm is set to less than one, in order to account for time varying input rates.

3.4.4 Low Pass Filter Design

The structure of low pass filters used for all the signals E, Q, R, S and L is the same

$$G_{lpf}(s) = G_{Butterworth}(s) \cdot G_{Notch}(s) \tag{3.36}$$

where $G_{Butterworth}$ is the first order Butterworth filter described in Eq. (3.19) with corner frequency tuned at 620 Hertz, and G_{Notch} is a Notch filter

$$G_{Notch}(s) = \frac{s^2 + 2\alpha\omega_1 s + \omega_1^2}{s^2 + 2\beta\omega_1 s + \omega_1^2} \cdot \frac{s^2 + 2\alpha\omega_2 s + \omega_2^2}{s^2 + 2\beta\omega_2 s + \omega_2^2} \tag{3.37}$$

where ω_1 and ω_2 are the notch frequencies respectively set at 2ω and 4ω.

In practice, the real resonance frequency ω is not exactly known, the frequency estimate $\hat{\omega}$ is used instead in the notch filter. Since the frequency estimate is produced by the phase lock loop (PLL) in real time, such a notch filter is called adaptive notch filter [90]. Fig. 3.9 shows the frequency shape of the low pass filter, when the PLL has converged.

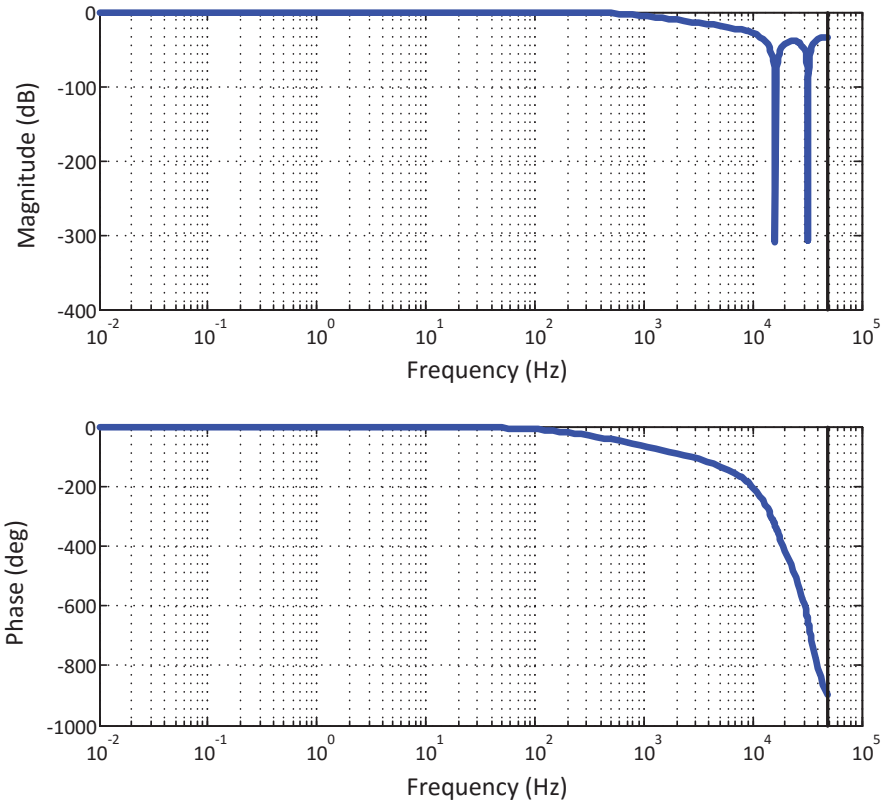

Figure 3.9: Bode plot of the low pass filter. Two notches are respectively set to 2ω and 4ω.

3.4.5 Control Loops Design

Since the phase lock loop runs inside the controller, it requires no physical control actions, and therefore it is not susceptible to any output delay or gain mismatch. As a consequence, its control gains can be set to large values in order to achieve large disturbance attenuation. The resulting loop transfer function, gain margin and phase margin are shown in Fig. 3.10. Fig. 3.11 shows the sensitivity function and complementary sensitivity function. It can be seen that the PLL has a gain margin of 24.4 decibels, and a phase margin of 60.6 degrees.

Fig. 3.12 shows the noise attenuation for the phase lock loop. The closed loop system has up to 300 decibels of attenuation on the nuisance noise, for both the phase reference error and frequency estimation error. Fig. 3.13 shows the disturbance attenuation. It can be seen that the disturbance induced by the frequency mismatch, which is concentrated on the low frequency range, directly contaminates the frequency estimate. However, for the phase reference error, the attenuation is quite large. For example, the attenuation gain at 20 Hertz is up to 60.34 decibels.

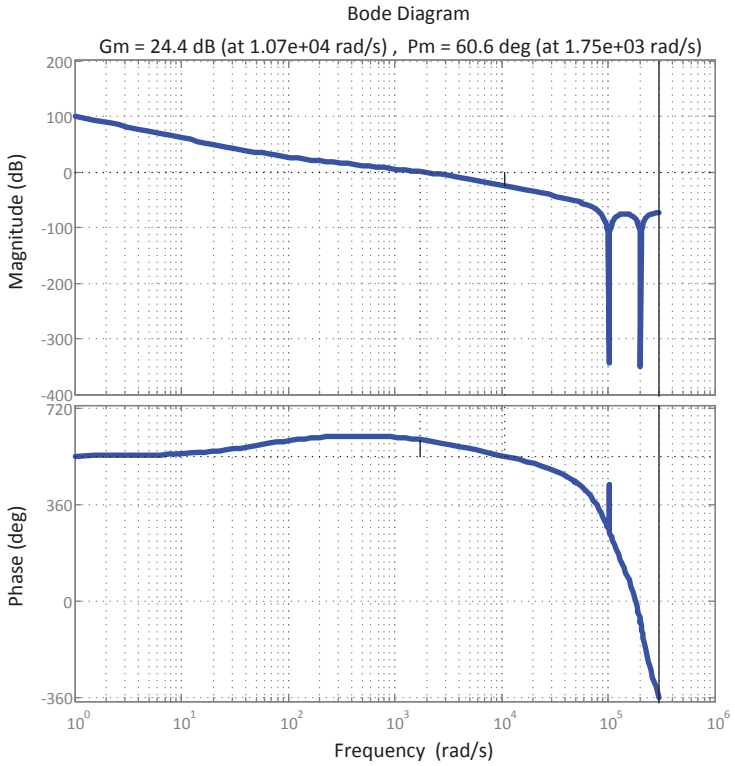

Figure 3.10: Phase lock loop (PLL) open loop transfer function and its gain and phase margins.

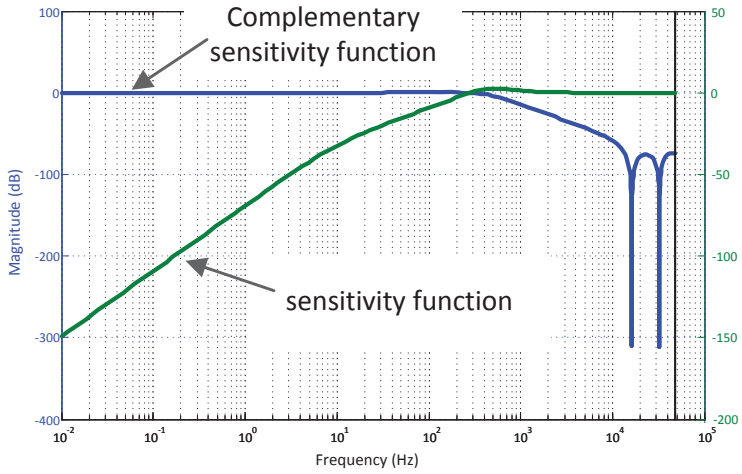

Figure 3.11: Phase lock loop (PLL) sensitivity function and complementary sensitivity function.

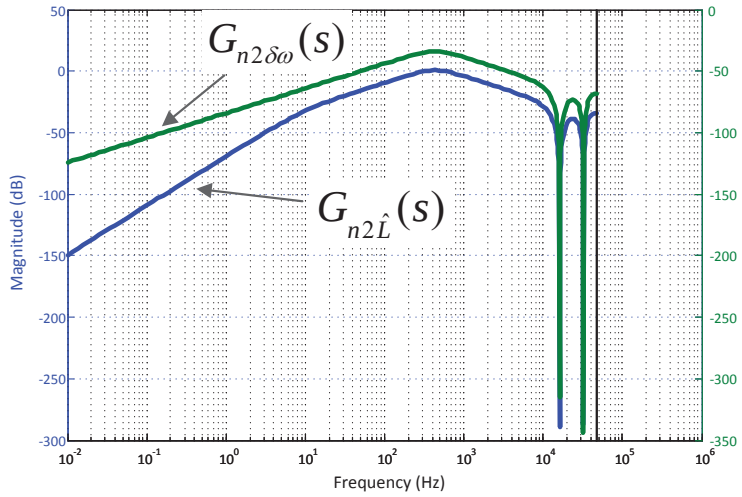

Figure 3.12: PLL noise rejection. The shown frequency estimate error has been normalized by its real value ω.

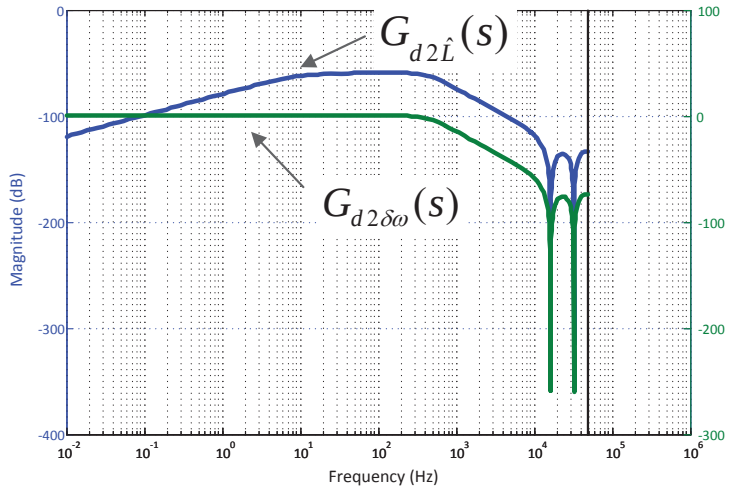

Figure 3.13: PLL disturbance rejection.

The energy and quadrature feedback loops have much lower gains than the PLL, in order to attain a sufficient level of robustness with respect to the channel delays and gain mismatches. The resulting loop transfer function for the quadrature loop is shown in Fig. 3.14. The energy controller is identical to the quadrature controller. It can be seen that the tuned controller attains 42.2 decibels of gain margin and 83.8 degrees of phase margin, which is sufficient to stabilize the system even for significant gain mismatches and output delays.

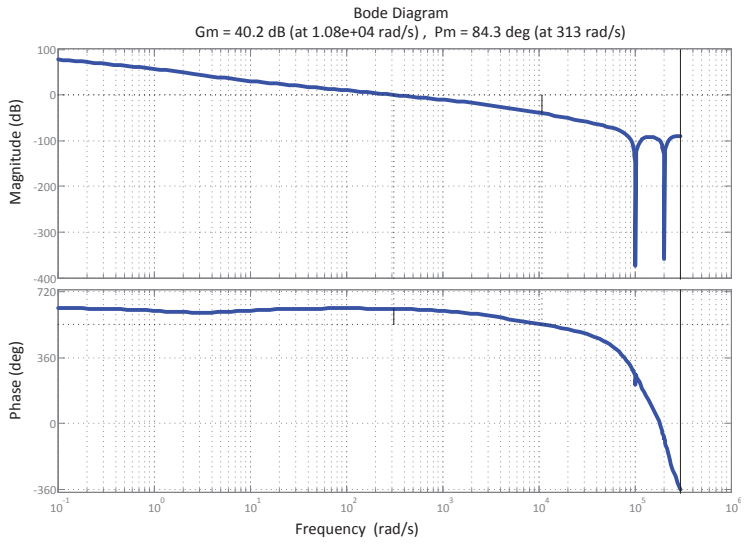

Figure 3.14: Quadrature control loop gain and phase margins.

Fig. 3.15 shows the noise and disturbance attenuation for the quadrature loop. It can be seen that the quadrature loop attains up to 50 decibels of attenuation over the low frequency disturbance. For example, the attenuation gain at 20 Hertz is up to 50.39 decibels.

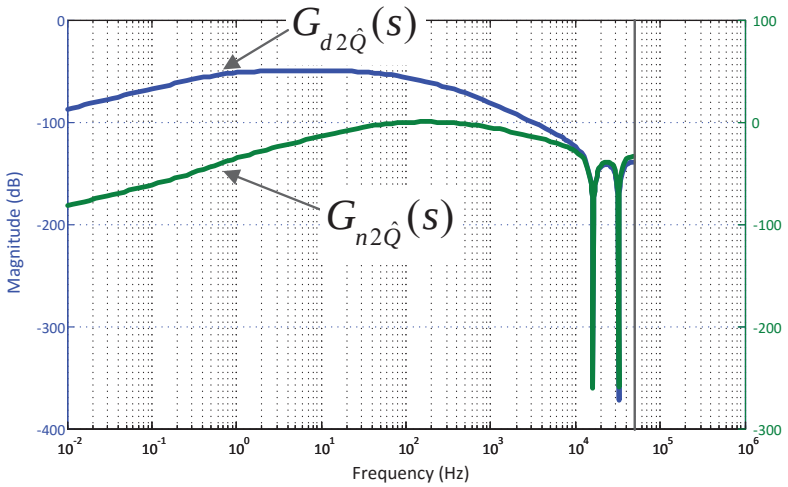

Figure 3.15: Quadrature control loop noise and disturbance rejection.

3.4.6 Simulation Results for a Symmetric MRIG

In this section, the new demodulation scheme is demonstrated on a symmetric MRIG model to validate its efficacy. A symmetric MRIG has identical primary and secondary vibration modes. Hence, is is not susceptible to frequency or damping mismatches. Damping effect, however, is taken into accounted in order to demonstrate the energy control loop.

Fig. 3.16 shows the time response of the phase lock loop. It can be seen that the frequency estimate (left) and phase reference have reached their real values, during the warm startup phase, which is set to 25 microseconds. In addition, the frequency and phase estimate at convergence is quite clean, and not susceptible to nuisance noise.

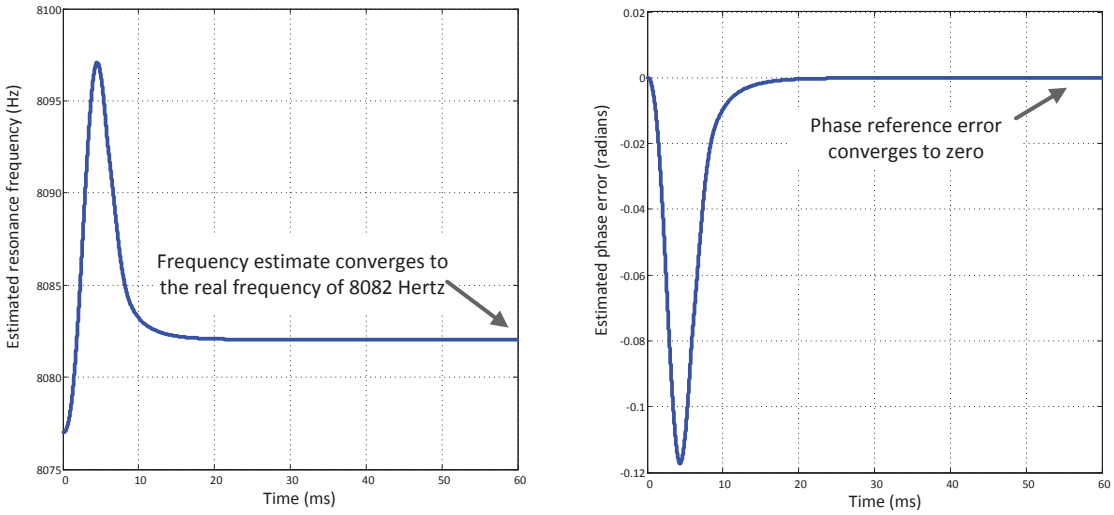

Figure 3.16: PLL time response.

Fig. 3.17 shows the energy and quadrature response. It can be seen that system energy and quadrature are successfully maintained at the desired level during the startup phase. The precession angle response is shown in Fig. 3.18. The left figure in Fig. 3.18 shows the time response of the precession angle versus the real input rotation angle. It can be seen that the precession angle precisely tracks the input rotation angle. As shown by the right figure in Fig. 3.18, the tracking error between the precession angle, which is the measured input rotation angle, and the ground true input angle is as small as 8×10^{-4} radians. This residual error is a DC bias that does not drift over time.

The left figure in Fig. 3.19 shows the input rate estimate using the aforementioned recursive least square algorithm. It can be seen that the rate estimate converges to the real one. The estimate accuracy at 60 microseconds is up to 0.1 ppm, which exceeds the required performance specifications.

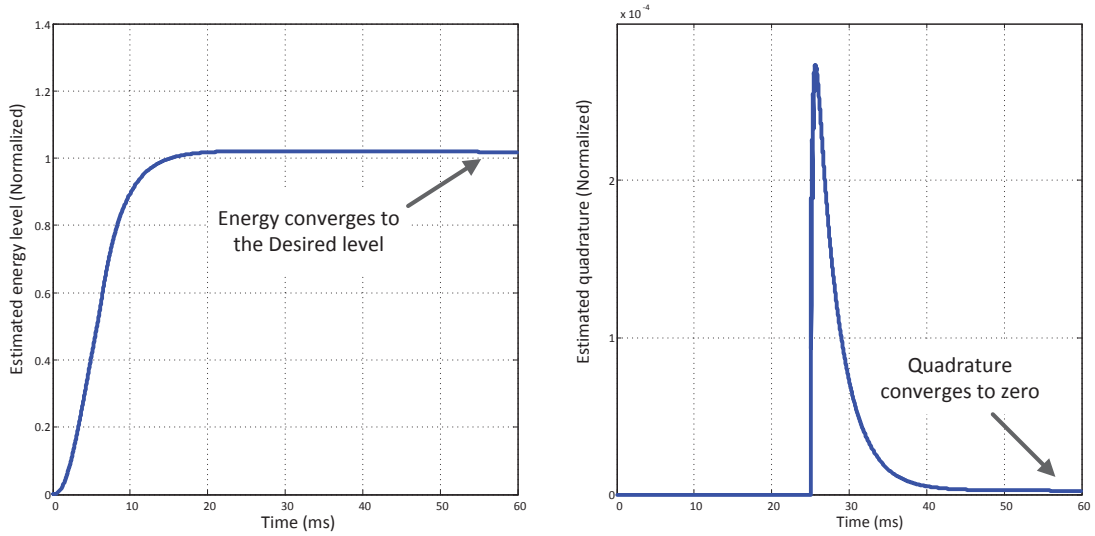

Figure 3.17: Energy and quadrature loop time response.

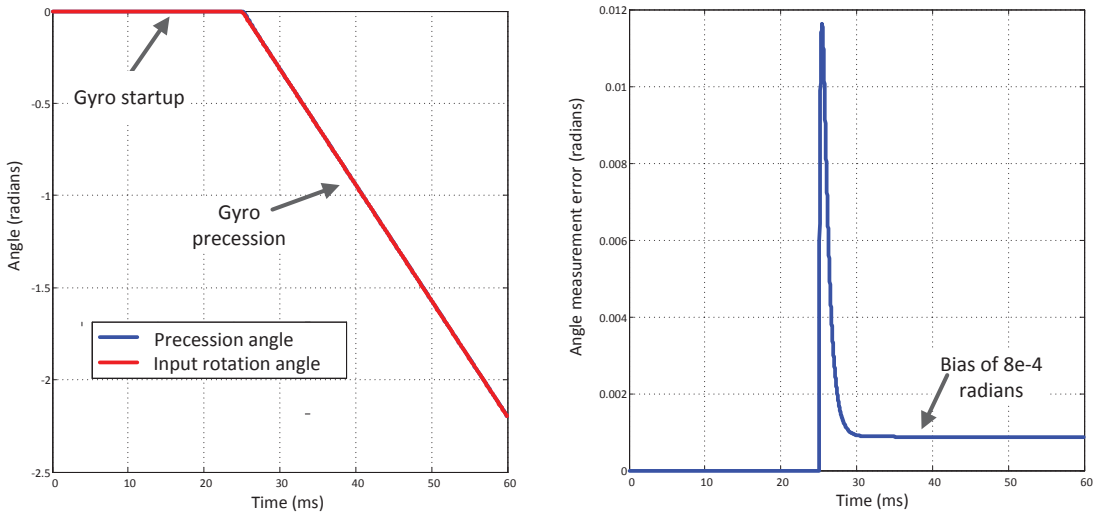

Figure 3.18: Precession angle response (left) and its difference from the input rotation angle.

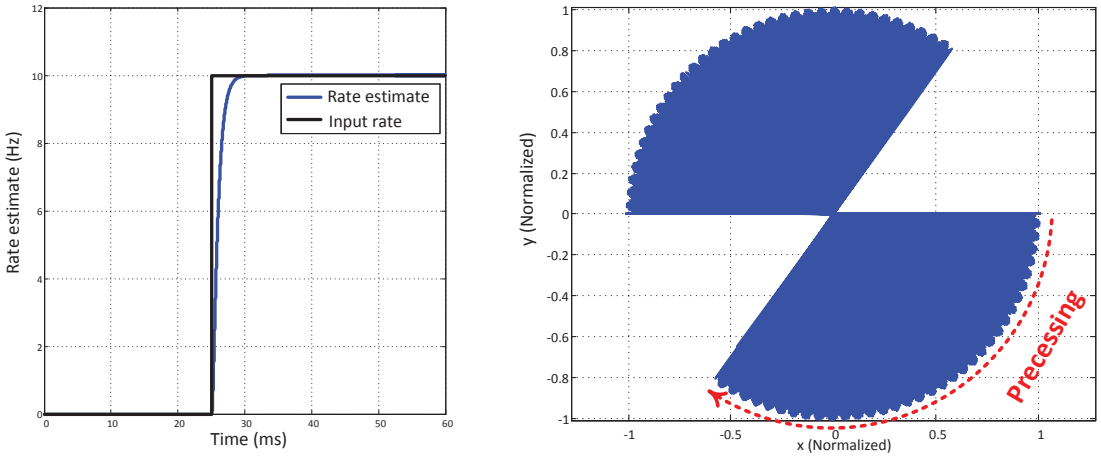

Figure 3.19: Input rate estimate (left) and gyro precession (right).

The right figure in Fig. 3.19 shows the gyro trajectory. It can be seen that the gyro is fully oscillated during the startup phase. When input rate is present, the gyro's principal axis of vibration precesses at a rate proportional to the input rate by the gain factor κ, which is one in this simulation, with a constant energy level and zero quadrature motion. This achieves all the MRIG control objectives.

3.4.7 Simulation Results for an Asymmetric MRIG with Mismatches

The method of averaging with the new demodulation scheme has proved its efficacy on symmetric MRIGs in preceding sections. Since the new demodulation scheme results in LTI control loops, the disturbance induced by frequency and damping mismatches should be predictable by the closed loop disturbance attenuation functions. In this section, simulation study is performed on an asymmetric MRIG to demonstrate the effect of mismatches, and to verify the prediction of the new demodulation scheme. Parameters for the simulated MRIG model are summarized in Table 3.5.

Fig. 3.20 shows the phase lock loop response. It can be seen that the frequency estimate oscillates around its ground true value at the amplitude of 5 Hertz. The oscillation frequency is twice of the input rate. For the phase reference error, the oscillation amplitude is about 0.0307. All these results are in agreement with analytical results that can be obtained from the PLL disturbance attenuation transfer function in Fig. 3.13. Fig. 3.21 shows the energy and quadrature responses. It can be seen that the energy is barely affected by the mismatch. However, the quadrature is significantly degraded. The residual quadrature level is about 0.1946, which is in agreement with the analytical value obtained from the quadrautre loop disturbance attenuation transfer function in Fig. 3.15

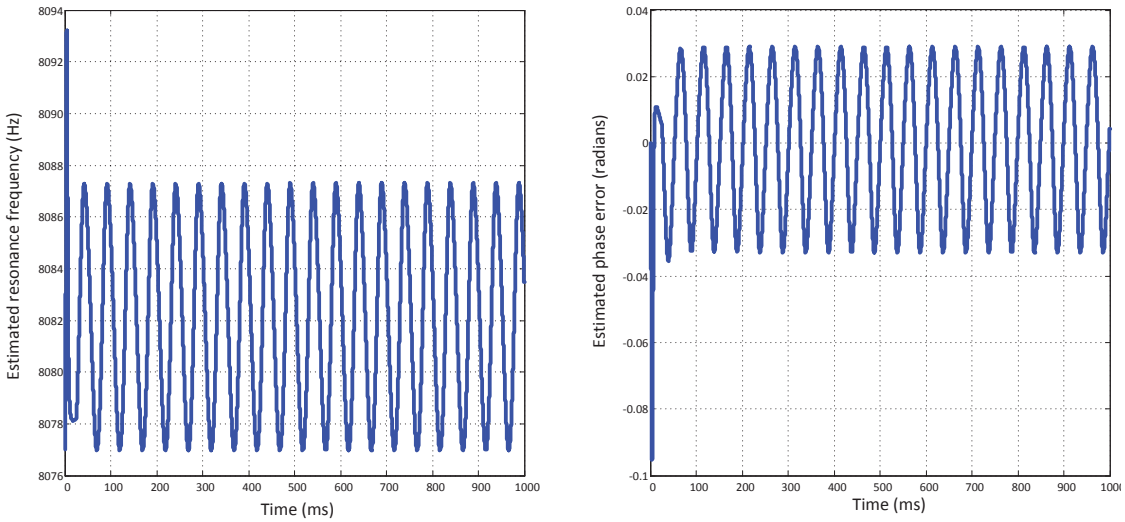

Figure 3.20: PLL time response in the presence of mismatches. The left figure shows the oscillation frequency estimate; the right figure shows the phase reference error.

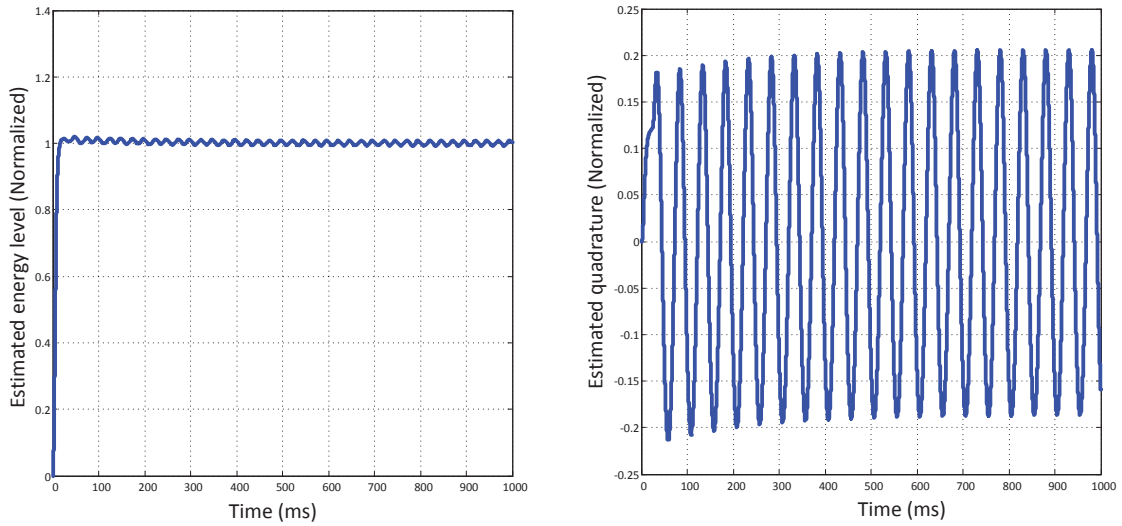

Figure 3.21: The energy (left) and quadrature (right) loops time response in the presence of mismatches.

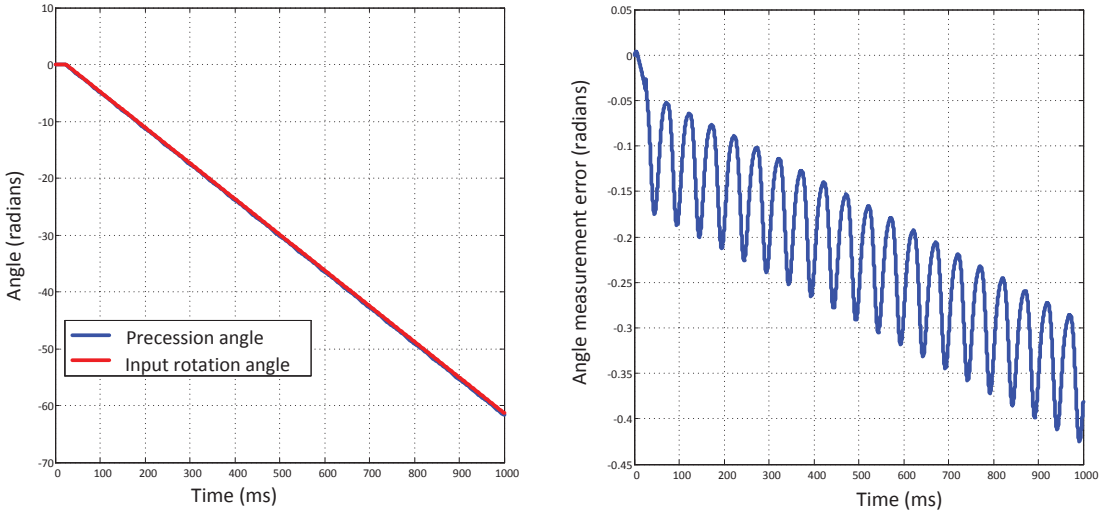

Figure 3.22: Precession angle response (left) and its difference from the input rotation angle, in the presence of mismatches.

Finally, the pattern angle response and its error from the input rotation angle is shown in Fig. 3.22. It can be seen that, the frequency and damping mismatches introduce both oscillatory and ramp drift in angle measurement, which is in agreement with the analytical result obtained from section 3.3.

3.5 Summary

This chapter considered the feedback controller design for MRIGs. Due to its ability to operate in the whole angle mode, the method of averaging introduced in [50] was utilized as the starting point for performing the controller design. Nonlinearities that are the results of the conventional method of averaging [50] were studied and a new demodulation scheme was introduced in this chapter, in order to eliminate the nonlinearities. It was shown that the new demodulation scheme can produce linear time invariant control loops, thus enabling the use of linear system theory in MRIG controller design, which in turn simplifies the control system design and analysis and produce more predictable MRIG performance and robustness bounds, through the use of well-studied LTI control synthesis and analysis techniques. A simulation study performed on a symmetric MRIG verified the efficacy of the proposed scheme. Finally, the effect of stiffness and damping mismatches, which are inevitable in MRIGs produced using existing micro-fabrication techniques, were analyzed. It was shown that these mismatches can prevent the gyro from operating in the whole angle mode, lending the necessity of mismatch compensation schemes, which will be introduced in the following chapters.

Chapter 4

Mismatch Compensation Using Electrostatic Spring Softening And Tuning

Analysis in preceding chapters has shown that the stiffness and damping mismatches caused by fabrication imperfections can dramatically degrade the gyro performance and even cause the gyro to stall in some extreme cases. Hence, in order for MRIGs to operate in the whole angle mode, it is necessary to compensate these mismatches. For this purpose, several approaches have been proposed. The first one is to eliminate the damping and stiffness frequency mismatches during the manufacturing process to a level that does not significantly affect the gyro performance. This is essentially the solution adopted for conventional Hemispherical Resonator Gyroscope (HRGs) [34]. Such a manufacturing process is rather sophisticated, requiring iterative polishing and extremely fine fabrication, and is not yet available on current micro-fabrication mass product lines. The second approach is to compensate for the mismatch via electrostatic spring softening and tuning during the calibration phase. Unlike the first one, this approach can be performed after the resonator is packaged. The third option is compensating for the mismatch by improving control algorithms. This chapter considers the second approach while the third one will be covered in the next chapter.

4.1 Principle of Electrostatic Spring Softening and Tuning

The basic idea behind the electrostatic spring softening and tuning is rather straightforward. Recall that the electrostatic sensing and actuation can soften the gyro's stiffness. As shown in Eq. (2.37), the amount of softened stiffness is determined by the bias voltage applied on the electrodes. Hence, by applying more bias voltage on the vibration mode with larger stiffness, it is possible to re-balance the stiffness mismatch between them.

Before continuing, we again show in Fig. 4.1 the sensing and actuation electrode configuration (shown in Fig. 2.9) and review the electrode notation that was introduced in chapter 2 and will again be used here. As shown in Fig. 4.1, the four readout electrodes along x vibration mode are respectively denoted by $+x^+, +x^-, -x^+$ and $-x^-$; while the four readout electrodes along y vibration mode are respectively denoted by $+y^+, +y^-, -y^+$ and $-y^-$. Therefore, $V[+y^+]$ denotes the voltage produced on the $+y^+$ electrode, while $x[+y^+]$ denotes the displacement of the vibration mode along $+y^+$ axis. The actuation electrodes are respectively denoted by $+(+x,+y), -(+x,+y), +(+x,-y), -(+x,-y), +(-x,-y), -(-x,-y), +(-x,+y)$ and $-(-x,+y)$. Therefore, $V[+(+x,+y)]$ denotes the voltage applied on the $+(+x,+y)$ electrode, while $x[+(+x,+y)]$ denotes the vibration displacement along $+(+x,+y)$ axis.

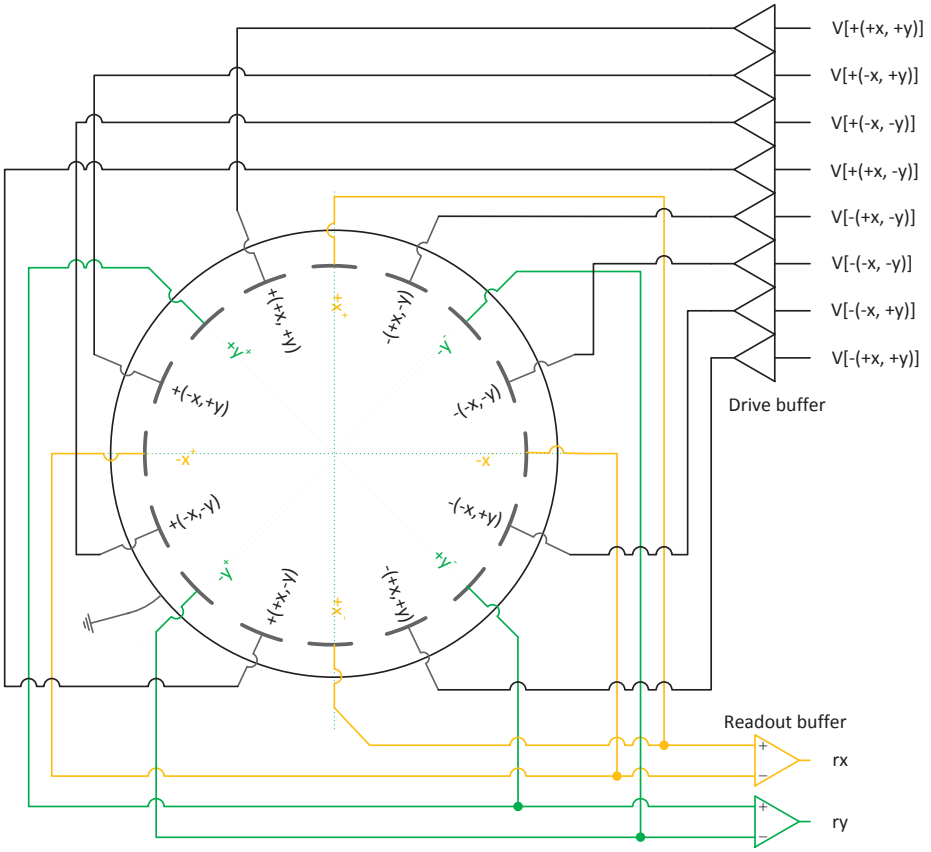

Figure 4.1: Electrical configurations of a shell resonator with 16 electrodes.

Composing the forces produced by sensing electrodes (see Eq. (2.31)) and forces produced by actuation electrodes (see Eq. (2.32)) in the way described by Eq. (2.30), yields the total forces in the primary and secondary modes of vibration, for a general voltage configuration

$$
\begin{aligned}
f_x &= \tfrac{\sqrt{2}}{4}\left(\tfrac{dC}{dx}\right)_{x=0}\left\{\begin{array}{ll} + & V[+(+x,+y)]^2+V[-(+x,+y)]^2 \\ - & V[+(-x,+y)]^2-V[-(-x,+y)]^2 \\ + & V[+(+x,-y)]^2+V[-(+x,-y)]^2 \\ - & V[+(-x,-y)]^2-V[-(-x,-y)]^2 \end{array}\right\} \\
&+ \tfrac{1}{4}\left(\tfrac{d^2C}{dx^2}\right)_{x=0}\left\{\begin{array}{ll} + & V[+(+x,+y)]^2+V[-(+x,+y)]^2 \\ + & V[+(-x,+y)]^2+V[-(-x,+y)]^2 \\ + & V[+(+x,-y)]^2+V[-(+x,-y)]^2 \\ + & V[+(-x,-y)]^2+V[-(-x,-y)]^2 \end{array}\right\} x \\
&+ \tfrac{1}{4}\left(\tfrac{d^2C}{dx^2}\right)_{x=0}\left\{\begin{array}{ll} + & V[+(+x,+y)]^2+V[-(+x,+y)]^2 \\ - & V[+(-x,+y)]^2-V[-(-x,+y)]^2 \\ - & V[+(+x,-y)]^2-V[-(+x,-y)]^2 \\ + & V[+(-x,-y)]^2+V[-(-x,-y)]^2 \end{array}\right\} y \\
&+ \tfrac{1}{2}\left(\tfrac{dC}{dx}\right)_{x=0}\left(\begin{array}{ll} + & V[+x^+]^2+V[+x^-]^2-V[-x^+]^2-V[-x^-]^2 \end{array}\right) \\
&+ \tfrac{1}{2}\left(\tfrac{d^2C}{dx^2}\right)_{x=0}\left(\begin{array}{ll} + & V[+x^+]^2+V[+x^-]^2+V[-x^+]^2+V[-x^-]^2 \end{array}\right) x \\
f_y &= \tfrac{\sqrt{2}}{4}\left(\tfrac{dC}{dx}\right)_{x=0}\left\{\begin{array}{ll} + & V[+(+x,+y)]^2+V[-(+x,+y)]^2 \\ + & V[+(-x,+y)]^2+V[-(-x,+y)]^2 \\ - & V[+(+x,-y)]^2-V[-(+x,-y)]^2 \\ - & V[+(-x,-y)]^2-V[-(-x,-y)]^2 \end{array}\right\} \\
&+ \tfrac{1}{4}\left(\tfrac{d^2C}{dx^2}\right)_{x=0}\left\{\begin{array}{ll} + & V[+(+x,+y)]^2+V[-(+x,+y)]^2 \\ - & V[+(-x,+y)]^2-V[-(-x,+y)]^2 \\ - & V[+(+x,-y)]^2-V[-(+x,-y)]^2 \\ + & V[+(-x,-y)]^2+V[-(-x,-y)]^2 \end{array}\right\} x \\
&+ \tfrac{1}{4}\left(\tfrac{d^2C}{dx^2}\right)_{x=0}\left\{\begin{array}{ll} + & V[+(+x,+y)]^2+V[-(+x,+y)]^2 \\ + & V[+(-x,+y)]^2+V[-(-x,+y)]^2 \\ + & V[+(+x,-y)]^2+V[-(+x,-y)]^2 \\ + & V[+(-x,-y)]^2+V[-(-x,-y)]^2 \end{array}\right\} y \\
&+ \tfrac{1}{2}\left(\tfrac{dC}{dx}\right)_{x=0}\left(\begin{array}{ll} + & V[+y^+]^2+V[+y^-]^2-V[-y^+]^2-V[-y^-]^2 \end{array}\right) \\
&+ \tfrac{1}{2}\left(\tfrac{d^2C}{dx^2}\right)_{x=0}\left(\begin{array}{ll} + & V[+y^+]^2+V[+y^-]^2+V[-y^+]^2+V[-y^-]^2 \end{array}\right) y
\end{aligned}
\tag{4.1}
$$

While the frequency matrix from Eq. (2.12) is

$$
K = \begin{bmatrix} \omega^2 - \omega\Delta\omega\cos(2\theta_\omega) & -\omega\Delta\omega\sin(2\theta_\omega) \\ -\omega\Delta\omega\sin(2\theta_\omega) & \omega^2 + \omega\Delta\omega\cos(2\theta_\omega) \end{bmatrix} \tag{4.2}
$$

In order to compensate the off-diagonal elements in the frequency matrix, it is necessary to apply a bias voltage on the actuation electrodes. Note that the actuation electrodes need

also to produce control actions that are determined by the actual controller. Therefore, the total voltage for each actuation electrode is

$$V[i] = V_b[i] + \delta V[i] \tag{4.3}$$

where $\delta V[i] \ll V_b[i]$ is used to produce the effective control force that is used to excite the gyro's $n = 2$ mode of vibration. The force in Eq. (2.26) can hence be rewritten as

$$f = \frac{1}{2}\frac{dC}{dx}\left(V_b^2 + 2V_b \cdot \delta V + \delta V^2\right) + \frac{1}{2}\frac{d^2C}{dx^2}\left(V_b^2 + 2V_b \cdot \delta V + \delta V^2\right)x \tag{4.4}$$

where δV^2 is very small and negligible; $\frac{1}{2}\frac{dC}{dx}V_b^2$ is a DC component that produces no effect on the gyro vibration, and $\frac{1}{2}\frac{d^2C}{dx^2}V_b \cdot \delta V \cdot x$ is far off the resonance frequency of the gyro vibration. As a consequence, the force that affects the effective stiffness on each electrode is

$$f = \frac{dC}{dx}V_b \cdot \delta V + \frac{1}{2}\frac{d^2C}{dx^2}V_b^2 x \tag{4.5}$$

Setting the bias voltage for actuation electrodes to

$$\begin{array}{lll} V[+(+x,+y)] & = V[-(+x,+y)] & = V_1 \\ V[+(-x,-y)] & = V[+(-x,-y)] & = V_1 \\ V[+(+x,-y)] & = V[+(+x,-y)] & = V_2 \\ V[+(-x,+y)] & = V[+(-x,+y)] & = V_2 \end{array} \tag{4.6}$$

and the bias voltage for sensing electrodes to

$$\begin{array}{lll} V[+x^+] & = V[+x^-] & = V_x \\ V[-x^+] & = V[-x^-] & = -V_x \\ V[+y^+] & = V[+y^-] & = V_y \\ V[-y^+] & = V[-y^-] & = -V_y \end{array} \tag{4.7}$$

yields the effective force in the primary and secondary mode of vibration

$$\begin{aligned} f_x &= \tfrac{\sqrt{2}}{2}\left(\tfrac{dC}{dx}\right)_{x=0}\left\{\begin{array}{ll} + & V_1\delta V[+(+x,+y)] + V_1\delta V[-(+x,+y)] \\ - & V_2\delta V[+(-x,+y)] - V_2\delta V[-(-x,+y)] \\ + & V_2\delta V[+(+x,-y)] + V_2\delta V[-(+x,-y)] \\ - & V_1\delta V[+(-x,-y)] - V_1\delta V[-(-x,-y)] \end{array}\right\} \\ &+ \left(\tfrac{d^2C}{dx^2}\right)_{x=0}(V_1^2+V_2^2)\,x \\ &+ \left(\tfrac{d^2C}{dx^2}\right)_{x=0}(V_1^2-V_2^2)\,y \\ &+ 2\left(\tfrac{d^2C}{dx^2}\right)_{x=0}V_x^2 x \end{aligned} \tag{4.8}$$

$$\begin{aligned} f_y &= \tfrac{\sqrt{2}}{2}\left(\tfrac{dC}{dx}\right)_{x=0}\left\{\begin{array}{ll} + & V_1\delta V[+(+x,+y)] + V_1\delta V[-(+x,+y)] \\ + & V_2\delta V[+(-x,+y)] + V_2\delta V[-(-x,+y)] \\ - & V_2\delta V[+(+x,-y)] - V_2\delta V[-(+x,-y)] \\ - & V_1\delta V[+(-x,-y)] - V_1\delta V[-(-x,-y)] \end{array}\right\} \\ &+ \left(\tfrac{d^2C}{dx^2}\right)_{x=0}(V_1^2-V_2^2)\,x \\ &+ \left(\tfrac{d^2C}{dx^2}\right)_{x=0}(V_1^2+V_2^2)\,y \\ &+ 2\left(\tfrac{d^2C}{dx^2}\right)_{x=0}V_y^2 y \end{aligned}$$

The resulting frequency softening matrix is given by

$$K_{\text{softening}} = \begin{bmatrix} \frac{\left(\frac{d^2C}{dx^2}\right)_{x=0}\left(V_1^2+V_2^2+2V_x^2\right)}{m} & \frac{\left(\frac{d^2C}{dx^2}\right)_{x=0}\left(V_1^2-V_2^2\right)}{m} \\ \frac{\left(\frac{d^2C}{dx^2}\right)_{x=0}\left(V_1^2-V_2^2\right)}{m} & \frac{\left(\frac{d^2C}{dx^2}\right)_{x=0}\left(V_1^2+V_2^2+2V_y^2\right)}{m} \end{bmatrix} \tag{4.9}$$

The effective frequency matrix is hence $\bar{K} = K - K_{\text{softening}}$. In order to compensate the diagonal and off-diagonal elements in the frequency matrix, it is necessary that

$$V_2^2 - V_1^2 = \frac{m\omega\Delta\omega\sin(2\theta_\omega)}{\left(\frac{d^2C}{dx^2}\right)_{x=0}} \tag{4.10}$$

$$V_y^2 - V_x^2 = \frac{m\omega\Delta\omega\cos(2\theta_\omega)}{\left(\frac{d^2C}{dx^2}\right)_{x=0}} \tag{4.11}$$

The effective resonance frequency is hence

$$\bar{\omega} = \sqrt{\omega^2 - \frac{\left(\frac{d^2C}{dx^2}\right)_{x=0}\left(V_1^2+V_2^2+V_x^2+V_y^2\right)}{m}} \tag{4.12}$$

And the effective control forces are

$$\begin{array}{rcl} \bar{f}_x & = & \frac{\sqrt{2}}{2}\left(\frac{dC}{dx}\right)_{x=0}\left\{\begin{array}{ll} + & V_1\delta V[+(+x,+y)]+V_1\delta V[-(+x,+y)] \\ - & V_2\delta V[+(-x,+y)]-V_2\delta V[-(-x,+y)] \\ + & V_2\delta V[+(+x,-y)]+V_2\delta V[-(+x,-y)] \\ - & V_1\delta V[+(-x,-y)]-V_1\delta V[-(-x,-y)] \end{array}\right\} \\ \bar{f}_y & = & \frac{\sqrt{2}}{2}\left(\frac{dC}{dx}\right)_{x=0}\left\{\begin{array}{ll} + & V_1\delta V[+(+x,+y)]+V_1\delta V[-(+x,+y)] \\ + & V_2\delta V[+(-x,+y)]+V_2\delta V[-(-x,+y)] \\ - & V_2\delta V[+(+x,-y)]-V_2\delta V[-(+x,-y)] \\ - & V_1\delta V[+(-x,-y)]-V_1\delta V[-(-x,-y)] \end{array}\right\} \end{array} \tag{4.13}$$

In practice, the required effective control force are computed by the actual controller. Then the voltage applied on each electrode is determined as

$$\begin{array}{rcl} \delta V[+(+x,+y)] & = & \frac{\bar{f}_x+\bar{f}_y}{4\sqrt{2}\left(\frac{dC}{dx}\right)_{x=0}V_1} \\ \delta V[-(+x,+y)] & = & \frac{\bar{f}_x+\bar{f}_y}{4\sqrt{2}\left(\frac{dC}{dx}\right)_{x=0}V_1} \\ \delta V[+(-x,+y)] & = & \frac{-\bar{f}_x+\bar{f}_y}{4\sqrt{2}\left(\frac{dC}{dx}\right)_{x=0}V_2} \\ \delta V[-(-x,+y)] & = & \frac{-\bar{f}_x+\bar{f}_y}{4\sqrt{2}\left(\frac{dC}{dx}\right)_{x=0}V_2} \\ \delta V[+(+x,-y)] & = & \frac{\bar{f}_x-\bar{f}_y}{4\sqrt{2}\left(\frac{dC}{dx}\right)_{x=0}V_2} \\ \delta V[-(+x,-y)] & = & \frac{\bar{f}_x-\bar{f}_y}{4\sqrt{2}\left(\frac{dC}{dx}\right)_{x=0}V_2} \\ \delta V[+(-x,-y)] & = & -\frac{\bar{f}_x+\bar{f}_y}{4\sqrt{2}\left(\frac{dC}{dx}\right)_{x=0}V_1} \\ \delta V[-(-x,-y)] & = & -\frac{\bar{f}_x+\bar{f}_y}{4\sqrt{2}\left(\frac{dC}{dx}\right)_{x=0}V_1} \end{array} \tag{4.14}$$

Notice that there are in principle an infinity number of ways to produce the required control force. The solution in Eq. (4.14) is the one that distributes the control force into all the actuation electrodes as uniformly as possible.

4.2 Experimental Validation

4.2.1 Experiment Platform Setup

This section performs an experimental study on real MRIGs in order to validate the mismatch compensation scheme presented in last section. The MRIG was provided by Honeywell Inc. As shown in Fig. 4.2, the MRIG package was first integrated to an analog front-end board which performs preliminary filtering and amplification on the readout and actuation signals. Then the analog front-end board is connected to the microprocessor board that performs the control task.

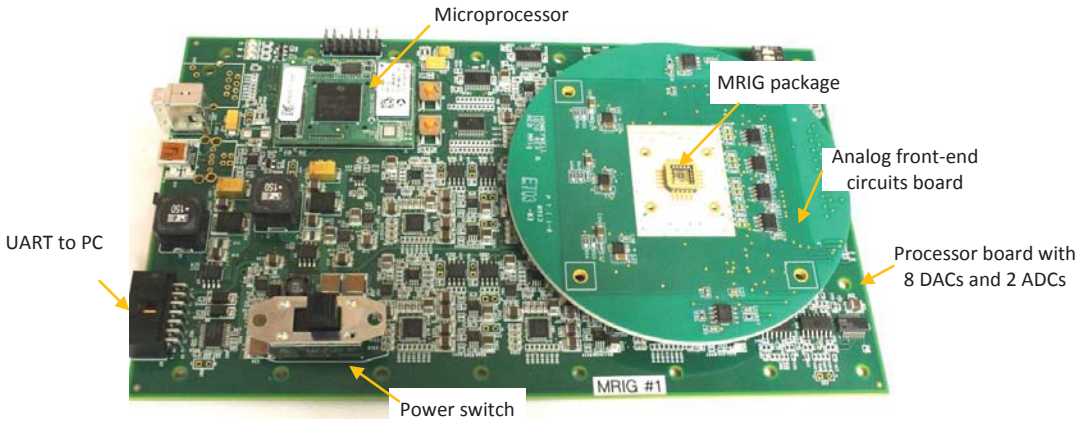

Figure 4.2: Control board for the MRIG fabricated by Honeywell. Courtesy of Burgess R. Johnson, Honeywell

The microprocessor board is a customized OMAP-L138 evaluation board [54] with 8 onboard CODECs of TLV320AIC3124. Each CODEC chip contains two ADC channels (i.e. left and right) and two DAC channels (i.e. left and right). Hence, the microprocessor is capable of receiving/driving up to 16 channels. Among them, two of the ADC channels are used to receive the sensed x and y signals while all the DAC channels are used to either drive the actuation electrodes or configure the bias voltage on the sensing electrodes. Since all the CODEC chips are connected to the McASP port in the microprocessor, the voltages shown on the CODECs (i.e. the bias voltages for the electrodes) are programmable via the software running on the microprocessor. Fig. 4.3 shows the system interconnections. In addition, the sampling rate for the DACs and ADCs in the CODAC chip were set to 96kHz. An interrupt is generated by the McASP port once a new data is received from the CODEC.

The microprocessor used for implementing the controller is an OMAP-L138 C6-Integra DSP+ARM processor [33] from Texas Instruments. It contains an ARM core and a DSP core. The DSP core is a floating point processor that runs at 456MHz. In addition, it has rich hardware resources, including pipelines and a SIMD instruction set architecture, which can dramatically speed up the data processing speed.

The software that runs on the electronics consists of two parts: a software shell and a controller applet. The shell performs three tasks: (1) initializes the system hardware including setting the CODECs operation mode and sampling rate and registering interrupts handler; (2) streams the buffer data via UART ports. A client running on the PC end can therefore monitor the running status of the microprocessor in real time; (3) read the ADC data once interrupted by CODECs and write the control actions into the corresponding DAC channels subsequently. In this way, the shell abstracted the electronic hardware and provided a software level interface for the controller applet to read sensors and send out control actions.

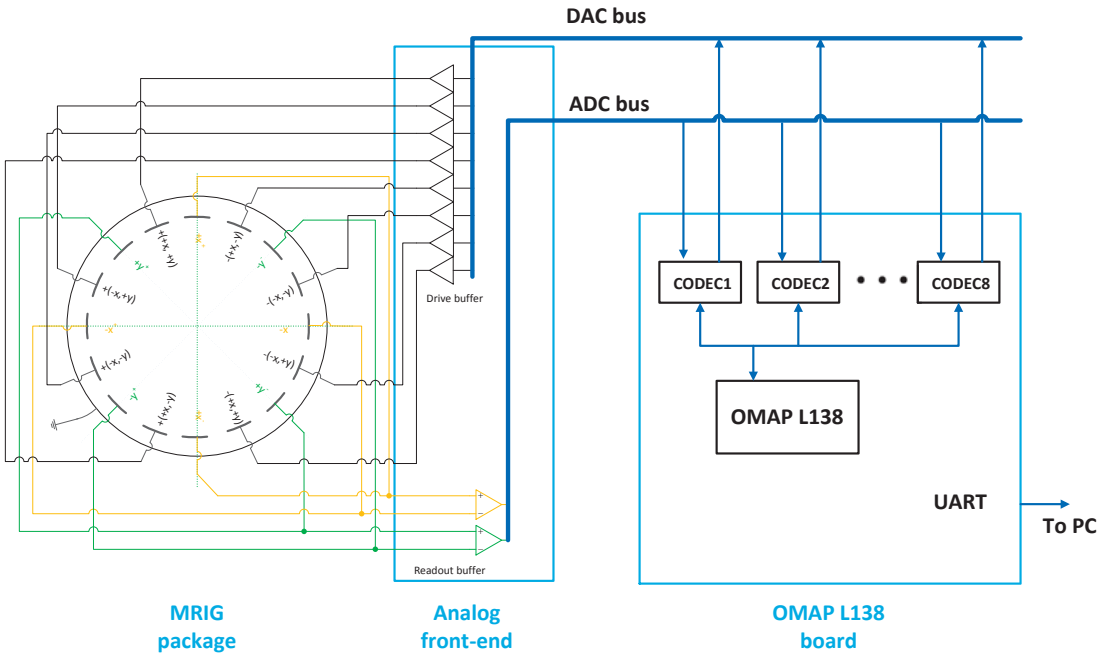

Figure 4.3: Interconnections of the MRIG, CODECs and the OMAP-L138 processor. Courtesy of Burgess R. Johnson, Honeywell

The controller applet runs on top of the shell. It takes sensor inputs from the shell and computes the appropriate control actions accordingly. In order to leave enough time for the shell to stream buffer data, the controller applet should finish its computation no later than 80 percent of the whole sampling period. Due to its rich computational resources, the DSP core can in principle achieve this goal. In order to fully take advantage of the DSP computational resources, the techniques that were utilized include: (1) All the codes were placed on the L1 RAM memory. This can drastically improve the running speed as the L1 RAM is the fastest memory in OMAP L138 processor; (2) The chip specific math functions were used instead of the standard C math function. The chip specific math functions are provided by the chip manufacturer and are usually highly optimized for speed; (3) The proper optimization options were enabled in Code Composer Studio when compiling the codes. For example, turning off the debug symbols results in half the running time. Using these techniques, the optimized code took less than 25 percent of the whole sampling period, leaving much room for data streaming, and implementing more complicated controllers.

4.2.2 Gain Mismatch and Phase Delay Compensation

Recall that there are two ADC channels for sensing the x and y signals, while there are eight DAC channels for driving the $n = 2$ mode of vibration. Due to the circuitry mismatch over the different ADC and DAC channels, the gain and phase delay over different input-output pair is different. Such a gain mismatch and phase delay can be characterized by analyzing the frequency response of each input-output channel pair with MRIG package bypassed.

A digital frequency analyzer was implemented in the DSP, in order to obtain the frequency response of different input-output channel pair. The idea behind the implementation of frequency analyzer is as follows. Assume that the input-output channel pair being inspected has gain of g_ω and phase delay of ϕ_ω, then making a sinusoidal signal on the output channel

$$x = a\cos(\omega t) \tag{4.15}$$

where ω is the frequency point over which the gain g_ω and phase delay ϕ_ω is investigated, produces a signal on input channels shown as follows

$$y = g_\omega a\cos(\omega t - \phi_\omega) \tag{4.16}$$

Then demodulating the input signal yields its in phase and in quadrature components with ωt

$$\begin{array}{rcl} c_y & = & LPF[y\cos(\omega t)] \\ s_y & = & LPF[y\sin(\omega t)] \end{array} \tag{4.17}$$

where $LPF[\cdot]$ denotes low pass filtering.

It can be shown that

$$\begin{array}{rcl} c_y & = & \frac{1}{2}g_\omega a\cos\phi_\omega \\ s_y & = & \frac{1}{2}g_\omega a\sin\phi_\omega \end{array} \tag{4.18}$$

The gain and phase delay can therefore be computed as

$$\begin{array}{rcl} g_\omega & = & 2\frac{\sqrt{c_x^2+c_y^2}}{a} \\ \phi_\omega & = & \tan^{-1}\frac{s_y}{c_y} \end{array} \tag{4.19}$$

In practice, the time t is set to $n \cdot t_s$ where t_s is the sampling period; a is set to different values at different frequency points in order to obtain a good Signal to Noise Ratio (SNR). For each concerned frequency point, the above demodulation process was performed in real time for ten times of the time constant of the low pass filter, in order to make it sure that the low pass filter has reached its steady state.The measured gain and phase delay are shown in Fig. 4.4. Note that the phase delay is almost linear to the frequency due to the group delay in CODECs.

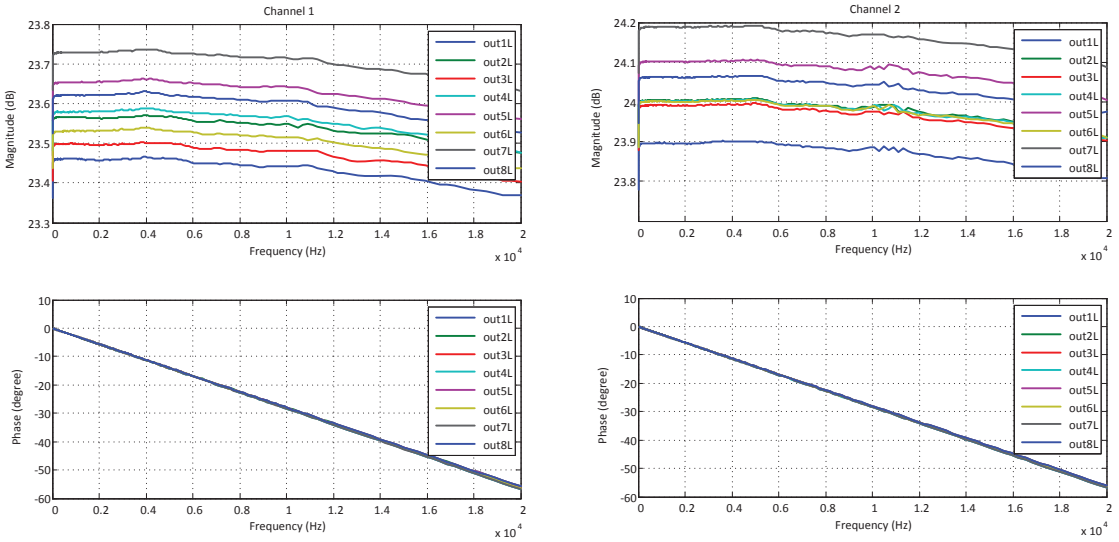

Figure 4.4: Gain and phase delay on input channel x (left) and channel y (right), over all of the eight output channels.

When implementing a controller, it is necessary to apply the following compensations: (1) Gain mismatch between the two input channels. The common gain needs no compensation as it can be lumped into the output channel gain, which can be addressed by the controller gain margins. (2) Phase delay difference between the two input channels. The common phase delay needs no compensation as it can be lumped into the output channel delay, which can be dealt by the output channel phase delay compensation techniques. (3) Phase delay on the output channels.

From Fig. 4.4, the gain mismatch between the two input channels can be computed as follows: For each of the eight output channels, compute the gain ratio between channel one over channel two. Then averaging the eight ratios yields the gain mismatch. Performing this procedure for all frequency points yields the gain mismatch over different frequency. However, notice that the gain mismatch, even the gain itself, does not vary significantly over frequencies, and it can hence be assumed to be constant. The phase delay difference can be computed in the same way and assumed to be constant as well. In contrast to the gain mismatch, phase delays on output channels are very sensitive to frequencies due to the large group delay in the CODECs. Therefore, the phase delay on output channels have to be instantaneously determined for the current frequency, and be compensated subsequently. In order to do so, the phase delay for the two input channels are averaged to produce the phase delay over different output channels. Then a second order polynomial is fitted to the averaged phase delay for each output channel. The phase delays on output channels can hence be computed by evaluating these second order polynomials.

The gain mismatch between the two input channels can be compensated by multiplying one of the sensed signals by an appropriate ratio. The phase delay difference can be compensated by artificially delaying one of the input signals by the appropriate number of sampling steps. Since delaying the input signal by one step yields a phase delay of $\omega \cdot t_s$ radians where ω is frequency of the input signal and t_s is the sampling time. This compensation method can only compensate the phase delay difference that is larger than $\omega \cdot t_s$.

Compensating the phase delay on output channels can be achieved by introducing an additional phase delay of $2\pi - \phi_d^i$, where ϕ_d^i is the phase delay on i-th output channel. As a result, in order to generate a signal $\sin(\omega t)$, the real value that the software needs to send to the CODECs is in the form of

$$f = \sin(\omega t + \phi_d^i) \tag{4.20}$$

Since the eight output channels have different phase delays ϕ_d^i, evaluating eight sine functions is rather time consuming. In oder to save computation time, the control action can be computed as

$$f = \sin(\omega t)\cos(\phi_d^i) + \cos(\omega t)\sin(\phi_d^i) \tag{4.21}$$

where $\cos(\phi_d^i)$ and $\sin(\phi_d^i)$ are computed a-priori and $\cos(\omega t)$ and $\sin(\omega t)$ are computed in real time. In this way, Eq. (4.21) only requires evaluating the common $\sin(\omega t)$ and $\cos(\omega t)$ terms for all output channels.

It is worth mentioning that, the above phase delay compensation method can only compensate the fast dynamics (i.e. the carrier signal, see Eq. (3.9)) in the method of averaging, it does not help with the slow dynamics (i.e. the envelope signal). As a consequence, the feedback controllers presented in preceding chapters need to have enough phase margins in order to stabilize the system.

4.2.3 MRIG Characterizing

Based on the experimental platform and phase compensation techniques presented in preceding sections, parameters of the MRIG can be characterized by obtaining the frequency response of the MRIG. Omitting the external rotation rate in Eq. (2.12) yields

$$\begin{aligned}
&\ddot{x} + \left(\omega^2 - \omega\Delta\omega\cos 2\theta_\omega\right)x + \left[\frac{2}{\tau} + \Delta\left(\frac{1}{\tau}\right)\cos 2\theta_\tau\right]\dot{x} \\
&\quad - \omega\Delta\omega\sin 2\theta_\omega y + \Delta\left(\frac{1}{\tau}\right)\sin 2\theta_\tau \dot{y} = \frac{f_x}{m} \\
&\ddot{y} + \left(\omega^2 + \omega\Delta\omega\cos 2\theta_\omega\right)y + \left[\frac{2}{\tau} - \Delta\left(\frac{1}{\tau}\right)\cos 2\theta_\tau\right]\dot{y} \\
&\quad - \omega\Delta\omega\sin 2\theta_\omega x + \Delta\left(\frac{1}{\tau}\right)\sin 2\theta_\tau \dot{x} = \frac{f_y}{m}
\end{aligned} \tag{4.22}$$

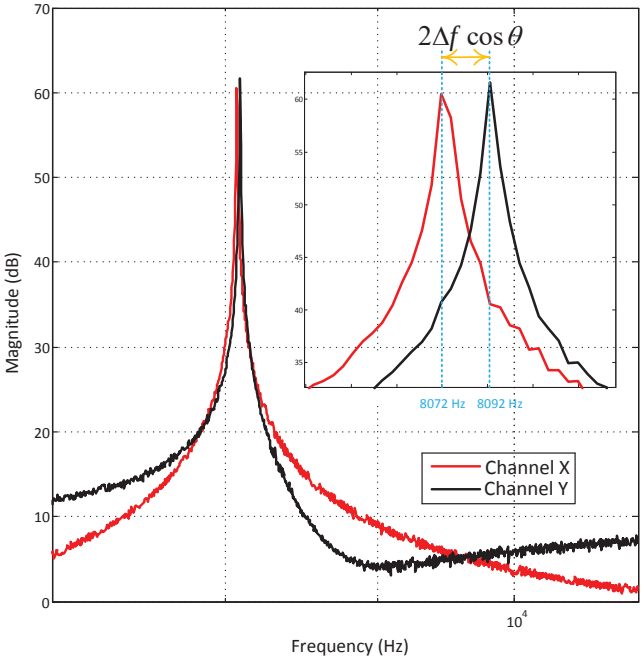

Figure 4.5: Frequency response of the primary and secondary mode of vibration

The obtained frequency response for the MRIG is shown in Fig. 4.5. It can be seen that the resonance frequency for primary vibration mode is at 8072 Hz while the secondary one is 8092 Hz. The resulting frequency mismatch is as large as 10 Hz. The other characteristic parameters are summarized in Table 4.1. As implied by the simulation results shown in Chapter 3, such a MRIG is barely able to operate in the whole angle mode with the required performance.

Table 4.1: MRIG characteristic parameters.

Variables	Descriptions	Values	Units
f_x	Resonance frequency in the x direction	8072	Hertz
$\frac{1}{\tau_x}$	Decay rate in the x direction	1.0897	1/sec
f_y	Resonance frequency in the y direction	8092	Hertz
$\frac{1}{\tau_y}$	Decay rate in the y direction	0.8092	1/sec
f	Mean resonance frequency	8082	Hertz
δf	Frequency mismatch	10	Hertz
$\frac{1}{\tau}$	Mean decay rate	0.9494	1/sec
$\Delta\left(\frac{1}{\tau}\right)$	Damping mismatch	0.1402	1/sec

4.2.4 Mismatch Compensation Using the Method of Electrostatic Spring Softening and Tuning

This section presents the experimental results that verifies the mismatch compensation scheme using the method of electrostatic spring softening and tuning. Only the diagonal mismatch in the frequency matrix was compensated by applying the proper bias voltage on readout electrodes. The bias voltage for actuation electrodes were all set to 5 volts. The bias voltage for x axis was set to 5 volts as well, while the bias voltage for y axis was varying. For each bias voltage applied on y direction, the MRIG was characterized by measuring its frequency response. Fig. 4.6 shows the resonance frequency of the primary and secondary vibration modes over different bias voltage on the readout y electrodes. It can be seen that, as the bias voltage on y varies, the resonance frequency on x barely changes. This is in agreement with the preceding analysis. The slight variation on the resonance frequency is due to the parasitic voltage being varying over time and temperature. Moreover, the resonance frequency on y decreases as its bias voltage increases. As shown in Table 4.2, when the bias voltage is 6.78 volts, the frequency mismatch is tuned at its optimal. The tuned frequency mismatch is as small as 0.5 Hertz.

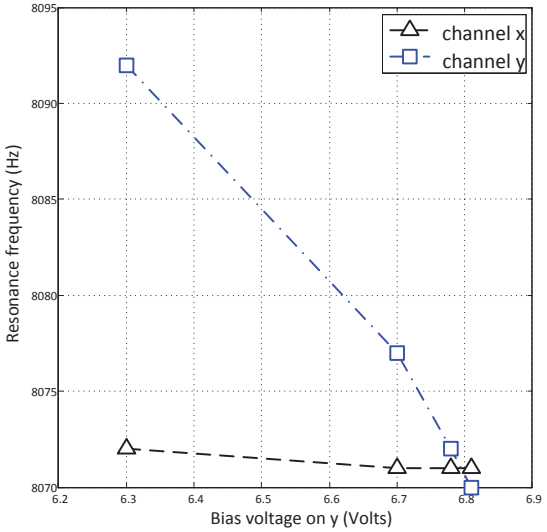

Figure 4.6: Resonance frequency of the primary and secondary mode of vibration over different bias voltage on y.

Table 4.2: Frequency mismatch over different bias voltage on y.

Bias voltage (volts)	6.3	6.7	6.78	6.81
Freq mismatch (Hertz)	10	3	0.5	-0.5

4.3 Summary

This chapter considered the frequency mismatch compensation scheme using the method of electrostatic spring softening and tuning. The principle behind such a compensation scheme was derived in detail. In order to verify its efficacy, this compensation scheme was implemented on a real MRIG provided by Honeywell. The experimental platform and several implementation details like phase compensation, gain mismatch balancing were discussed. Based on these theoretic derivation and experimental setup, experimental results were obtained and validated the efficacy of the proposed compensation scheme. It was shown that the compensation scheme can reduce the frequency mismatch to the level of 0.5 Hertz.

Chapter 5

Mismatch Compensation Using Adaptive Feedforward Controllers

As discussed in preceding chapter, there are three approaches that can be employed to reduce the effect of frequency and damping mismatches caused by fabrication imperfections in gyroscopes. The first one, improving the manufacturing process, requires the use of an extremely sophisticated and expensive fabrication process, which is not yet available on micro-fabrication product lines. MRIGs that are produced on currently available micro-fabrication product lines, have a significant amount of mismatches, as indicated by the experimental results shown in last chapter. The method of electrostatic spring softening and tuning can effectively reduce the stiffness mismatch. But it can only be performed prior to the operation of the gyro. Therefore, it is susceptible to parasitic voltages, which vary with temperature, pressure, etc. Moreover, electrostatic softening can only compensate the stiffness mismatch and requires human involvement. This chapter considers the third approach, which consists in compensating the mismatches in the control algorithm and will show great superiority over the electrostatic spring softening and tuning method.

Most of the adaptive controllers mentioned in Chapter 3 have the capability of estimating and compensating the mismatches in real time. However, they were all designed for MEMS gyros operating in rate mode. Very few mismatch compensation scheme specifically designed for rate integrating gyroscopes can be seen in literatures. This is probably because all the past rate-integrating gyroscopes are essentially for high-end applications where the cost is of no concern. The resulting gyroscopes are almost ideally polished and trimmed during the manufacturing process and get rid of all significant mismatches. A typical example is the Hemispherical Resonator Gyroscopes (HRGs) [34].

[28] presented a damping and stiffness frequency mismatch compensation algorithm that runs together with the conventional method of averaging. Simulation and experimental results presented in [28] show that the compensation scheme is somewhat effective, but is not capable of achieving high compensation precision, partly due to the heuristic nature of the algorithm.

In this chapter, we propose an adaptive compensation scheme to compensate for the frequency and damping mismatches. The proposed compensator runs as an add-on feedforward compensator to the LTI feedback control scheme presented in Chapter 3. The PI controllers provide the baseline feedback action with sufficient robustness, while the adaptive compensator is dedicated to estimating and compensating the damping and frequency mismatches in order to achieve a sufficient level of performance. The combination of these two schemes can effectively compensate the gyro mismatches and stabilize the system. Simulation results will be presented to show the efficacy of the adaptive compensator. In order to avoid the stall condition and estimate the mismatches for relative small input rates, an artificial input rate is used to autonomously calibrate the gyro. This self-calibration scheme is capable of performing the gyro calibration automatically, requiring no auxiliary device or human involvement.

5.1 Adaptive Feedforward Mismatch Compensation

As analyzed in preceding chapters, MRIG oscillation energy can be effectively maintained at the desired level by a PI feedback controller, which requires no compensation action. Since the phase lock loop runs inside the controller, requiring no physical control action, gains of the phase lock loop can be set to large values, which can result in large attenuation gains over the mismatch induced disturbance. The residual disturbance is nevertheless significant to degrade the phase lock loop performance. In addition, the gains of the feedback PI controller for quadrature regulation are usually set to low values, in order to obtain a sufficient level of robustness. This results in poor disturbance rejection performance. As a consequence, the frequency mismatch significantly degrades the performance of the quadrature feedback control law, which in turn degrades gyro precession. Moreover, the pattern angle controller is essentially open when the gyro is operating in whole angle mode. Therefore, any amount of mismatches will directly act on the pattern angle loop and degrade its precession. In sum, the phase lock loop and the quadrature and pattern angle controllers are all affected by stiffness and damping mismatches, and in turn degrade gyro performance. Hence, in order to achieve a sufficient level of gyro performance, the mismatches need to be compensated in all these three controllers.

In this section, we propose the use of three adaptive feedforward compensators to respectively compensate the mismatch in the quadrature, phase lock loop and pattern angle controllers. Each of adaptive compensator consists of an estimator, which estimates the effective mismatch using a recursive least square algorithm, and a compensator, which compensates the mismatch in real time.

5.2 Quadrature Control Adaptive Mismatch Compensation

Recall that the averaged quadrature control dynamics can be expressed as follows

$$\dot{Q} = -\frac{2}{\tau}Q \; - \; \Delta\omega \sin 2(\theta - \theta_\omega)E \; + \; \frac{\sqrt{E}}{\omega} f_{q_c} \tag{5.1}$$

where the feedback control action f_{q_c} is given by Eq. (3.11).

Based on the block diagram shown in Fig. 3.8, the quadrature measured by the controller is

$$\widehat{Q} = G_{d2\widehat{Q}}(s)\,[d_Q - u_{QC}] \tag{5.2}$$

where u_{QC} is the feedforward control actions, which remains to be designed, and $G_{d2\widehat{Q}}(s) = \frac{G_p^Q G_{lpf}^Q}{1+G_c^Q G_p^Q G_{lpf}^Q}$ is the closed loop transfer function from the disturbance to the measured quadrature level. Notice that $G_{d2\widehat{Q}}(s)$ is a strictly causal system.

Since the controller is implemented in digital devices like DSPs, we design our controller based on the discrete time model

$$\widehat{Q}(k) = G_{d2\widehat{Q}}(z)\,[d_Q(k) - u_{QC}(k)] \tag{5.3}$$

where k is the sample index and $G_{d2\widehat{Q}}(z) = (1-z^{-1})\mathcal{Z}\left[\frac{G_{d2\widehat{Q}}(s)}{s}\right]$ denotes the well-known zero order hold discrete time transfer function of $G_{d2\widehat{Q}}(s)$.

Notice that the disturbance can be rewritten as

$$d_Q(k) = \Theta_Q^T \Phi_Q(k) \tag{5.4}$$

where $\Theta_Q = [\Delta\omega \sin 2\theta_\omega E, \; -\Delta\omega \cos 2\theta_\omega E]^T$ is the parameter vector. Since the energy control loop always maintains the oscillation energy at the desired level E_0, Θ_Q can be considered to be a constant but unknown vector to be estimated. $\Phi_Q(k) = [\cos 2\theta(k), \sin 2\theta(k)]^T$ is the regressor vector, and $\theta(k)$ is the pattern angle measured by the gyro. Notice that given the gyro is precessing, the regressor vector $\Phi_Q(k)$ is persistently exciting (i.e. $P.E. \triangleq rank\left(\lim_{m\to+\infty} \frac{\Sigma_{k=0}^{k=m} \Phi_Q(k)\Phi_Q^T(k)}{m}\right) = 2$).

The compensation action at step k is designed as follows

$$u_{QC}(k) = \widehat{\Theta}_Q(k)^T \Phi_Q(k) \tag{5.5}$$

where the parameter estimate $\widehat{\Theta}_Q(k)$ is updated by the following Parameter Adaptation Algorithm (PAA)

$$
\begin{aligned}
\Psi_Q(k-1) &= G_{d2\widehat{Q}}(z)\left[\Phi_Q(k)\right] \\
e_Q^o(k) &= \widehat{Q}(k) - \widehat{\Theta}_Q(k-1)^T\Psi_Q(k-1) + G_{d2\widehat{Q}}(z)\left[\widehat{\Theta}_Q^T(k)\Phi_Q(k)\right] \\
e_Q(k) &= \frac{\lambda_1^Q e_Q^o(k)}{\lambda_1^Q + \Psi_Q(k-1)^T F_Q(k-1)\Psi_Q(k-1)} \\
\widehat{\Theta}_Q(k) &= \widehat{\Theta}_Q(k-1) + \frac{1}{\lambda_1^Q}F_Q(k-1)\Psi_Q(k-1)e_Q(k) \\
F_Q(k) &= \frac{1}{\lambda_1^Q}\left[F_Q(k-1) - \lambda_2^Q\frac{F_Q(k-1)\Psi_Q(k-1)\Psi_Q(k-1)^T F_Q(k-1)}{\lambda_1^Q + \lambda_2^Q\Psi_Q(k-1)^T F_Q(k-1)\Psi_Q(k-1)}\right] \\
&\widehat{\Theta}_Q(0) \in \mathbb{R}^2; F_Q(0) \in \mathbb{S}_+^{2\times 2}; 0 < \lambda_1^Q \leq 1; 0 < \lambda_2^Q < 2
\end{aligned}
\tag{5.6}
$$

where $\mathbb{S}_+^{2\times 2}$ denotes the set of two by two positive definite matrix.

It is worth mentioning that, in the algorithm described by Eq. (5.6), computing the a-priori error $e_Q^o(k)$ involves evaluating $G_{d2\widehat{Q}}(z)\left[\widehat{\Theta}_Q^T(k)\Phi_Q(k)\right]$, where $\widehat{\Theta}_Q^T(k)$ is updated after $e_Q^o(k)$. This, however, does not violates the causality as $G_{d2\widehat{Q}}(z)$ is strictly causal, evaluating $G_{d2\widehat{Q}}(z)\left[\widehat{\Theta}_Q^T(k)\Phi_Q(k)\right]$ only requires the knowledge of $\widehat{\Theta}_Q^T(k-1)\Phi_Q(k-1)$, $\widehat{\Theta}_Q^T(k-2)\Phi_Q(k-2)$, etc. As shown in Lemma 2, Appendix C, if the gyro is precessing, the above PAA produces zero $\widehat{Q}$ and in addition, the PAA converges to its ground true values and therefore perfectly cancels the disturbance d_Q, which in turn implies zero quadrature Q.

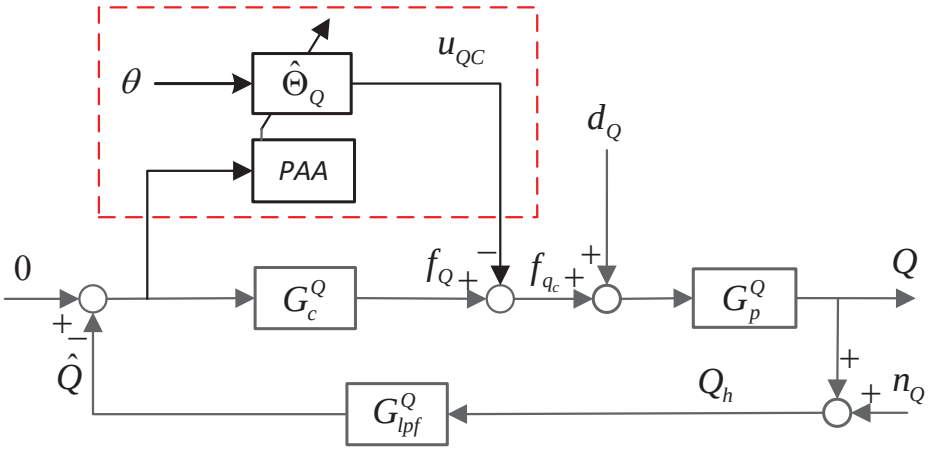

Figure 5.1: The quadrature control adaptive mismatch compensator

5.3 Phase Lock Loop (PLL) Adaptive Mismatch Compensation

Recall that the averaged Phase Lock Loop (PLL) dynamics can be expressed as follows

$$\delta\dot{\phi} = \dot{\phi} + \frac{1}{2}\Delta\omega\cos 2(\theta - \theta_\omega) + \frac{1}{2}\Delta\left(\frac{1}{\tau}\right)\sin 2(\theta - \theta_\tau)\frac{Q}{E} + \frac{f_{a_c}}{2\omega\sqrt{E}} \tag{5.7}$$

where the feedback controller is given by Eq. (3.11).

Based on the block diagram shown in Fig. 3.6, the phase reference error measured by the controller is

$$\widehat{L} = G_{d2\widehat{L}}(s)\left[d_L - u_{LC}\right] \tag{5.8}$$

where u_{LC} is the feedforward control action which remains to be designed and $G_{d2\widehat{L}}(s) = \frac{G_p^L G_{lpf}^L}{1+G_c^L G_p^L G_{lpf}^L}$ is the closed loop transfer function from the disturbance to the measured phase reference error. Notice that $G_{d2\widehat{L}}(s)$ is strictly causal. The discretized model is

$$\widehat{L}(k) = G_{d2\widehat{L}}(z)\left[d_L(k) - u_{LC}(k)\right] \tag{5.9}$$

where k is the sample index and $G_{d2\widehat{L}}(z) = (1-z^{-1})\mathcal{Z}\left[\frac{G_{d2\widehat{L}}(s)}{s}\right]$ denotes the well-known zero order hold discrete time transfer function of $G_{d2\widehat{L}}(s)$.

Given zero quadrature level, the disturbance for PLL can be rewritten as

$$d_L(k) = \Theta_L^T \Phi_L(k) \tag{5.10}$$

where $\Theta_L = \left[\frac{1}{2}\Delta\omega\cos 2\theta_\omega,\ \frac{1}{2}\Delta\omega\sin 2\theta_\omega\right]^T$ is the parameter vector. $\Phi_L(k) = [\cos 2\theta(k), \sin 2\theta(k)]^T$ is the regressor vector, and $\theta(k)$ is the pattern angle measured by the gyro. Notice that given the gyro is precessing, the regressor vector $\Phi_L(k)$ is persistently exciting (i.e. $P.E. \triangleq rank\left(\lim_{m\to+\infty}\frac{\Sigma_{k=0}^{k=m}\Phi_L(k)\Phi_L^T(k)}{m}\right) = 2$).

The compensation action for PLL at step k is designed as follows

$$u_{LC}(k) = \widehat{\Theta}_L(k)^T \Phi_L(k) \tag{5.11}$$

where the parameter estimate $\widehat{\Theta}_L(k)$ is updated by the following Parameter Adaptation Algorithm (PAA).

$$
\begin{aligned}
\Psi_L(k-1) &= G_{d2\widehat{L}}(z)\left[\Phi_L(k)\right] \\
e_L^o(k) &= \widehat{L}(k) - \widehat{\Theta}_L(k-1)^T\Psi_L(k-1) + G_{d2\widehat{L}}(z)\left[\widehat{\Theta}_L^T(k)\Phi_L(k)\right] \\
e_L(k) &= \frac{\lambda_1^L e_L^o(k)}{\lambda_1^L + \Psi_L(k-1)^T F_L(k-1)\Psi_L(k-1)} \\
\widehat{\Theta}_L(k) &= \widehat{\Theta}_L(k-1) + \frac{1}{\lambda_1^L} F_L(k-1)\Psi_L(k-1)e_L(k) \\
F_L(k) &= \frac{1}{\lambda_1^L}\left[F_L(k-1) - \lambda_2^L \frac{F_L(k-1)\Psi_L(k-1)\Psi_L(k-1)^T F_L(k-1)}{\lambda_1^L + \lambda_2^L \Psi_L(k-1)^T F_L(k-1)\Psi_L(k-1)}\right] \\
\widehat{\Theta}_L(0) &\in \mathbb{R}^2; F_L(0) \in \mathbb{S}_+^{2\times 2}; 0 < \lambda_1^L \leq 1; 0 < \lambda_2^L < 2
\end{aligned}
\tag{5.12}
$$

where $\mathbb{S}_+^{2\times 2}$ denotes the set of two by two positive definite matrix.

Fig. 5.2 shows the block diagram of the phase lock loop with the feedback controller and feedforward compensator. As shown in Lemma 2, Appendix C, if the gyro is precessing, the above PAA produces zero $\widehat{L}$ and in addition, the PAA converges to its ground true values and therefore perfectly cancels the disturbance d_L, which in turn implies zero phase reference error L.

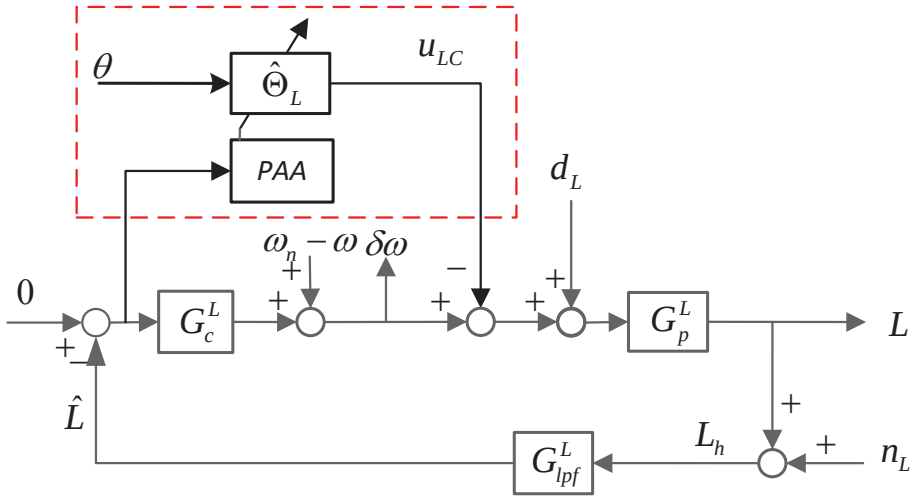

Figure 5.2: The Phase Lock Loop (PLL) adaptive mismatch compensator

5.4 Pattern Angle Adaptive Mismatch Compensation

Given zero quadrature, the pattern angle has a dynamics in the form of

$$\dot{\theta} = -\kappa\Omega + \frac{1}{2}\Delta\left(\frac{1}{\tau}\right)\sin 2(\theta - \theta_\tau) - u_\theta \tag{5.13}$$

where the control action

$$u_\theta = \frac{f_{q_s}}{2\omega\sqrt{E}} \tag{5.14}$$

is normally set to zero in the whole angle operation mode, but will be used in this section to compensate the damping mismatch disturbance.

The discrete time version of the pattern angle dynamics can be approximated as follows

$$\theta(k) = \theta(k-1) - \kappa\Omega t_s + d_\theta(k-1)t_s - u_\theta(k-1)t_s \tag{5.15}$$

where t_s is the sampling time and the damping mismatch-induced disturbance is

$$d_\theta(k) = a_\theta \cos 2\theta(k) + b_\theta \sin 2\theta(k) \tag{5.16}$$

where $a_\theta = -\frac{1}{2}\Delta\left(\frac{1}{\tau}\right)\sin 2\theta_\tau, b_\theta = \frac{1}{2}\Delta\left(\frac{1}{\tau}\right)\cos 2\theta_\tau$ are the damping mismatch coefficients to be estimated.

The compensation action is designed as follows

$$u_\theta = \widehat{a}_\theta(k)\cos 2\theta(k) + \widehat{b}_\theta(k)\sin 2\theta(k) \tag{5.17}$$

where $\widehat{a}_\theta(k)$ and $\widehat{b}_\theta(k)$ are respectively the estimates of a_θ and b_θ at step k.

Collecting all the unknown parameters Ω, a_θ and b_θ yields the parameter vector

$$\Gamma \triangleq \begin{bmatrix} \Omega & a_\theta & b_\theta \end{bmatrix}^T \tag{5.18}$$

and corresponding regressor vector

$$\Upsilon(k) \triangleq \begin{bmatrix} -\kappa t_s & \cos 2\theta(k)t_s & \sin 2\theta(k)t_s \end{bmatrix}^T \tag{5.19}$$

A normalized least mean square algorithm is utilized to update the parameter estimate $\widehat{\Gamma}(k)$ as follows, in order to estimate time varying input rates.

$$\begin{aligned} \widehat{\theta}(k) &= \theta(k-1) - \kappa\widehat{\Omega}(k-1)t_s \\ e_\theta(k) &= \theta(k) - \widehat{\theta}(k) \\ \widehat{\Gamma}(k) &= \widehat{\Gamma}(k-1) + \mu\frac{\Upsilon(k-1)e_\theta(k)}{\Upsilon^T(k-1)\Upsilon(k-1)} \end{aligned} \tag{5.20}$$

where $\widehat{\Omega}$ is the input rate estimate; $\widehat{\theta}(k)$ is the predicted pattern angle using the input rate estimate; $e_\theta(k)$ is the a-priori error and μ is the step size of the least mean square algorithm. The resulting block diagram is shown in Fig. 5.3.

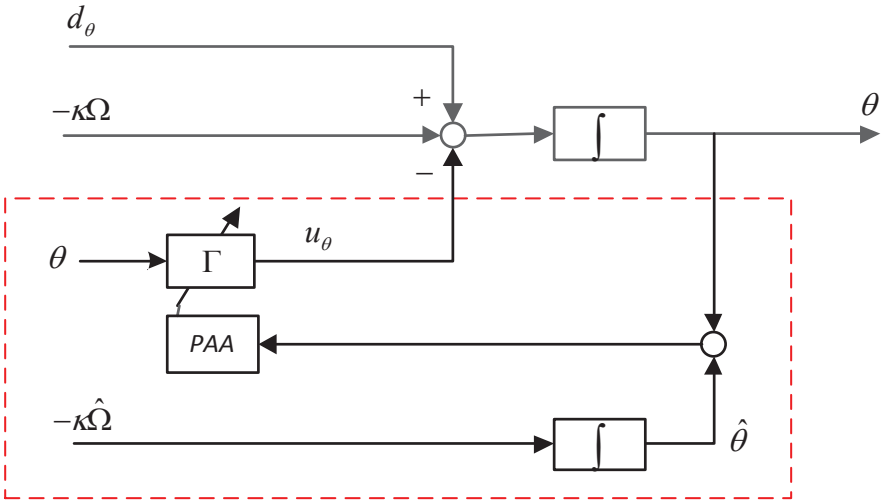

Figure 5.3: The pattern angle adaptive mismatch compensator

Notice that the a-priori error $e_\theta(k)$ is subject to

$$e_\theta(k) = \widetilde{\Gamma}^T(k-1)\Upsilon(k-1) \tag{5.21}$$

where $\widetilde{\Gamma}(k-1)$ is the parameter estimation error. It is shown in [30] that the normalized least mean square algorithm given by Eq. (5.20) converges to the ground true values if the following conditions hold.

1. $0 < \mu < 2$;
2. *The persistence of excitation, which is defined as P.E.* $\triangleq$ *rank* $\left(\lim_{m\to+\infty} \frac{\Sigma_{k=0}^{k=n}\Upsilon(k)\Upsilon^T(k)}{n}\right)$, *is greater than or equal to 3*

Under these circumstances, the PAA can correctly estimate and compensate the mismatches. Therefore, the pattern angle precesses as desired.

5.5 Simulation Study

5.5.1 Simulation Setups

In order to verify the efficacy of the proposed adaptive mismatch compensation scheme, it is tested on a simulated MRIG model with parameters summarized in Table 3.5. Also notice that the simulated gyro model essentially has the real MRIG parameters characterized in Chapter 4 (see Table 4.1). The feedback controllers for the phase lock loop, quadrature and energy are identical to those described in Chapter 3.

The three adaptive feedforward controllers, namely the quadrature feedforward controller, the PLL feedforward controller and the pattern angle feedforward controller, are all turned on in the simulation. Parameters for these adaptive controllers are summarized in Table 5.1.

Table 5.1: Summary of parameters for adaptive feedforward controllers

Parameters	λ_1^Q	λ_2^Q	$F_Q(0)$	λ_1^L	λ_2^L	$F_L(0)$	μ
values	1.0	1.0	$\begin{bmatrix} 1e5 & 0 \\ 0 & 1e5 \end{bmatrix}$	1.0	1.0	$\begin{bmatrix} 2e5 & 0 \\ 0 & 2e5 \end{bmatrix}$	$3e\text{-}5 \cdot \max\{1.0, \lvert\widehat{\Omega}(k)\rvert\}$

5.5.2 Simulation Results

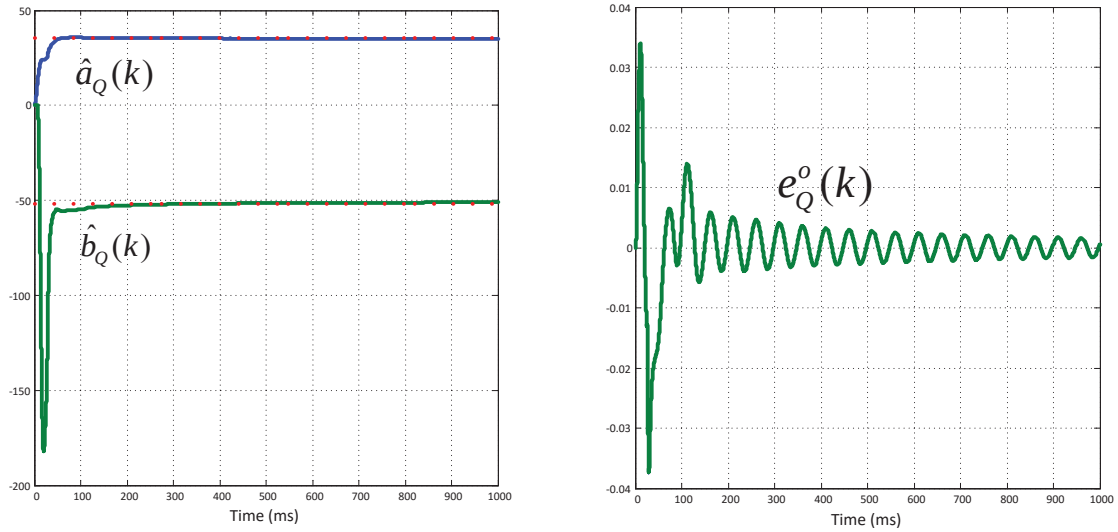

Figure 5.4: Convergence of the PAA in the quadrature adaptive controller. The left figure shows the parameter estimate. The right figure shows the a-priori error.

For the quadrature adaptive controller, Fig. 5.4 shows the convergence of the parameter estimate and a-priori error. It can be seen that the parameter estimate $\widehat{\Theta}_Q = \left[\widehat{a}_Q, \widehat{b}_Q\right]^T$ converges to its correct value of $\Theta_Q = [\Delta\omega \sin(2\theta_\omega)E, -\Delta\omega \cos(2\theta_\omega)E]^T$ (the dotted red lines), and the a-priori error converges to zero.

Fig. 5.5 shows a comparison of the quadrature response with and without the proposed adaptive compensation scheme. It can be seen that the adaptive feedforward compensator can successfully estimate and compensate the disturbance that is induced by frequency mismatch. The resulting quadrature level is drastically reduced, when compared to the uncompensated case. In addition, the quadrature with adaptive compensation converges to zero at steady state.

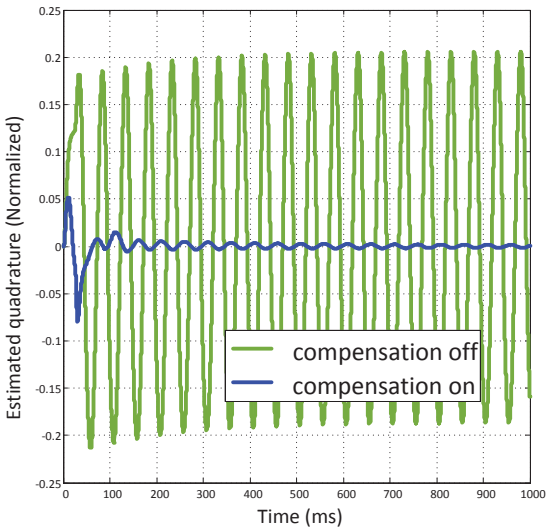

Figure 5.5: Quadrature response with and without the proposed adaptive feedforward compensator.

Fig. 5.6 shows the convergence of the parameter estimate and the a-priori error for the phase lock loop. It can be seen that the parameter vector converges to its correct value of $\Theta_L = \left[\frac{1}{2}\Delta\omega \cos(2\theta_\omega), \frac{1}{2}\Delta\omega \sin(2\theta_\omega)\right]^T$ (the dotted red lines); In addition, the a-priori error converges to zero.

Fig. 5.7 shows a comparison of the phase lock loop response with and without the proposed adaptive compensation scheme. It can be seen that the adaptive feedforward compensator can successfully estimate and compensate the disturbance in the phase lock loop. The resulting phase reference error and frequency estimate error are drastically attenuated.

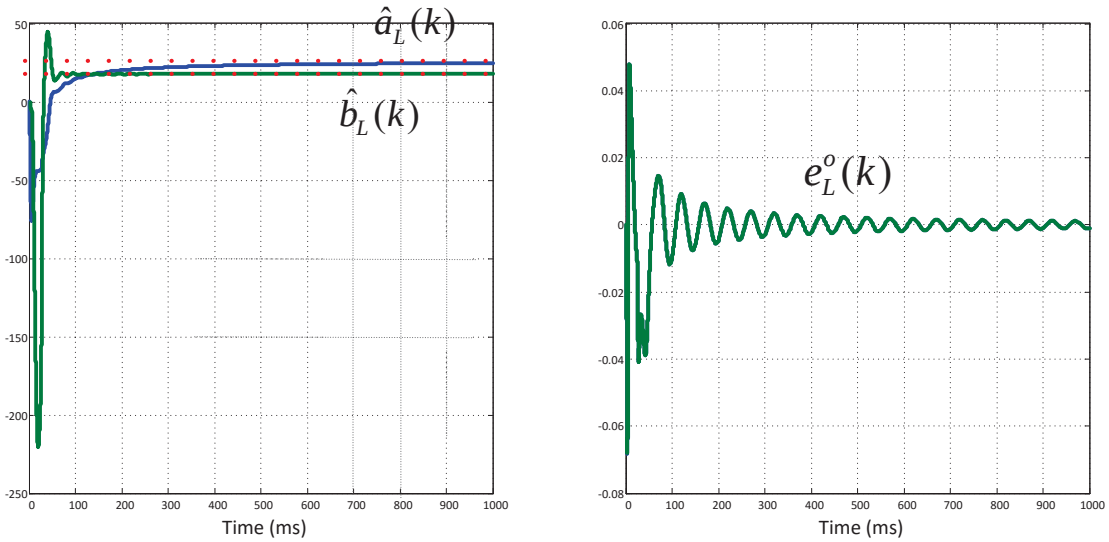

Figure 5.6: Convergence of the PAA in the phase lock loop adaptive controller. The left figure shows the parameter estimate $\widehat{\Theta}_L = \left[\widehat{a}_L, \widehat{b}_L\right]^T$. The right figure shows the a-priori error.

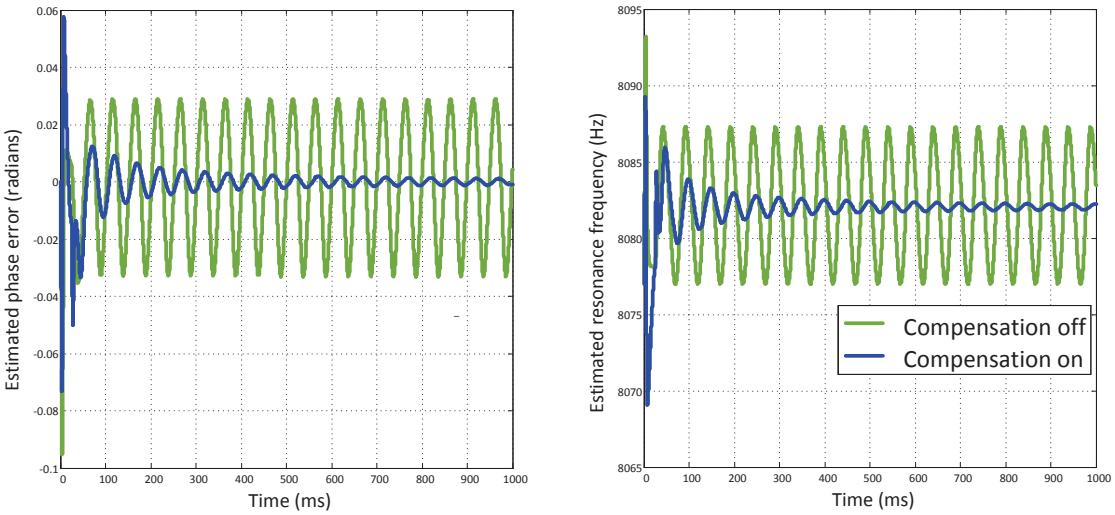

Figure 5.7: Phase lock loop response with and without the proposed adaptive feedforward compensator.

It is worth mentioning that, the residual oscillations observed in the a-priori error, phase reference error and frequency estimate error are caused by the slow convergence rate of the PAA. These oscillations will continue to decaying.

Fig. 5.8 shows the convergence of the parameter estimate in the pattern angle adaptive compensator. It can be seen that, the parameter adaptation algorithm converges. More specifically, the input rate estimate $\widehat{\Omega}$ converges to the real input rate, which is $10Hz$, after a warming startup phase where the input rate is zero. However, the mismatch estimates $\widehat{a}_\theta$ and $\widehat{b}_\theta$ do not converge to the predicted values, which are respectively $a_\theta = -\frac{1}{2}\Delta\left(\frac{1}{\tau}\right)\sin 2\theta_\tau$ and $b_\theta = \frac{1}{2}\Delta\left(\frac{1}{\tau}\right)\cos 2\theta_\tau$. This is because the feedback controller and the adaptive compensator are running at a relative low sampling rate (i.e. $96kHz$). The low sampling rate couples the stiffness mismatch $\Delta\omega$ to the damping mismatch $\Delta\left(\frac{1}{\tau}\right)$ when discretizing the gyro model and averaging the fast dynamics. In addition, the amount of coupling depends on both the sampling rate and input rate. Fortunately, the proposed adaptive compensator can effectively estimate the total mismatch and attenuate them within a level that does not affect the gyro performance. As shown in the right figure in Fig. 5.8, the estimation error for the input rate estimate $\widehat{\Omega}$ at 1 seconds is at the magnitude of ppm.

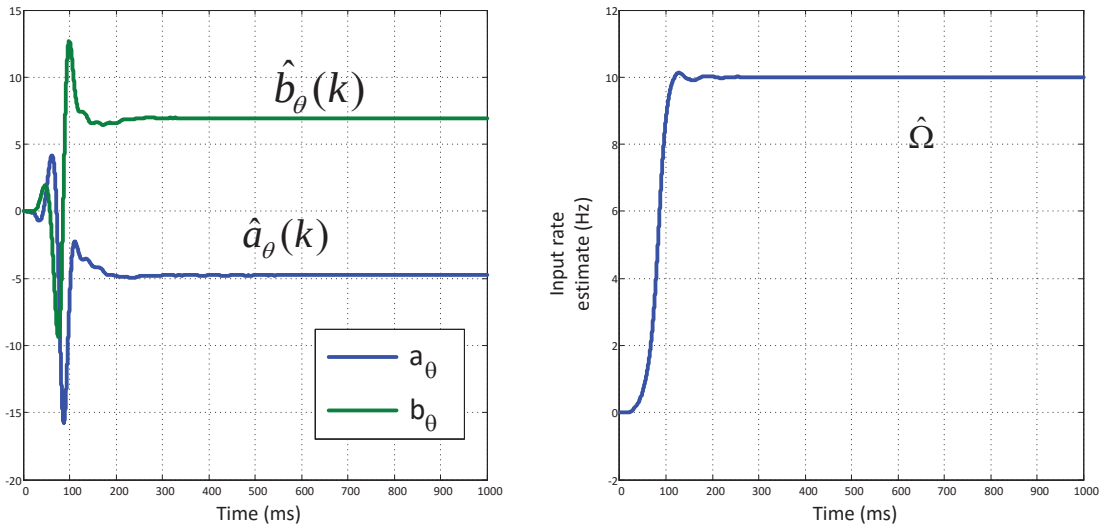

Figure 5.8: Convergence of the PAA in pattern angle adaptive compensator. The left figure shows the parameter estimate $\widehat{\Gamma} = \left[\widehat{a}_\theta, \widehat{b}_\theta\right]^T$. The right figure shows the input rate estimate response.

The left figure in Fig. 5.9 shows a comparison of the angle measurement error with and without the proposed adaptive feedforward compensator. It can be seen that, without the compensation scheme, the angle measurement suffers from both an oscillatory error and a ramp drift. The adaptive compensator, on the other hand, dramatically reduces the effect of the mismatch and tracks the input rotation angle with a constant bias. This DC bias is caused by the transient response of the adaptive compensator, and is at the level of 10^{-2} radians.

The right figure in Fig. 5.9 shows the vibration trajectory of the MRIG when the adaptive compensator is converged. It can be seen that the gyro's principal axis of vibration is precessing at the input rate, with a constant level of energy and zero quadrature. This achieves all the control objectives for MRIGs.

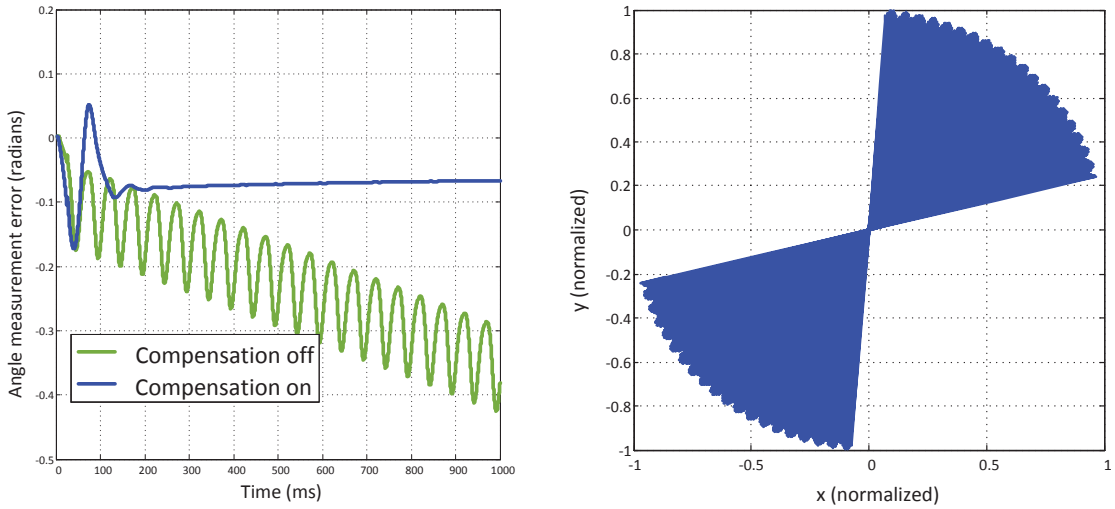

Figure 5.9: The left figure shows the ange measurement error with and without the adaptive feedforward compensator. The right figure shows the gyro precession when the adaptive mismatch compensator is converged.

5.6 MRIG Self-Calibration

As indicated in last section, the proposed adaptive mismatch compensation scheme can effectively estimate and compensate for the MRIG frequency and damping mismatches, if the system is persistently excited. In order to obtain the sufficient persistence of excitation, the pattern angle needs to constantly precess. This can be achieved by introducing an artificial input rate, which is produced as follows

$$u_\theta = \underbrace{\hat{a}_\theta \cos 2\theta(k) + \hat{b}_\theta \sin 2\theta(k)}_{\text{Mismatch Compensation}} - \underbrace{\kappa\Omega_a}_{\text{Artificial Input Rate}} \tag{5.22}$$

It can be seen from Eq. (3.10) that, the artificially induced input rate Ω_a has the same affect on the gyro's principal axis of vibration as that of a genuine input rate. As a consequence, the gyro can be calibrated without the use of auxiliary device like rotation table or human involvement. The artificial input rate can also avoid the stall condition that occurred for small input rates, as described in Chapter 3.

5.7 Summary

In this chapter, we proposed an adaptive scheme to compensate the damping and frequency mismatches in MRIGs. The proposed adaptive compensators run as add-on feedforward controllers, on top of the feedback controllers presented in preceding chapters. Such add-on feedforward compensators preserve the robustness of the baseline feedback controllers, but dramatically reduce the effects of disturbances and improve the controller performance. Simulation results confirmed the efficacy of the proposed compensation scheme. In order to obtain the sufficient persistence of excitation, which is necessary to calibrate the gyro mismatches, artificial input rate was introduced to autonomously calibrate the gyro, requiring no auxiliary device or human involvement.

Chapter 6

Conclusion

6.1 Conclusions

In this dissertation, a comprehensive methodology was developed to analyze Microscale Rate Integrating Gyroscopes (MRIGs), including its modeling, controller design, mismatch compensation and calibration.

A MRIG resonator has three vibration modes. Namely, the $n = 1$ mode, the $n = 2$ mode and the $n = 3$ mode. These vibration modes have different vibration patterns and resonance frequencies. Among these vibration modes, the $n = 2$ mode of vibration was selected as the gyro operation mode due to its modulate resonance frequency and stable vibration pattern. The $n = 2$ mode of vibration can be modeled as a two dimensional harmonic oscillator with unbalanced stiffness and damping principal axes, in order to account for the fabrication imperfections. Applying the Newton's second law and preliminary kinematics to the equivalent model yields the gyro resonator's equations of motion, which provide the basic system plant model for subsequent controller design and analysis. Solution trajectory of ideal MRIG resonators was solved for analyzing the gyro precession. It was shown that an ideal MRIG resonator is a natural rate integrating gyroscope that can automatically operate in the rate integrating mode once excited, requiring no active control actions. Based on the ideal MRIG precession, control objectives for general MRIGs, which suffer from energy dissipation and mismatches, were casted.

For the MRIG control, the method of averaging was adopted as the control law due to its simplicity and capability of operating in the rate integrating mode. However, analysis showed that the conventional method of averaging essentially produces nonlinear control loops, which cause big problems when designing and analyzing the performance of MRIG controllers. A new demodulation scheme was proposed to eliminate the nonlinearity. The new demodulation scheme, together with the method of averaging, produces linear control loops. As a consequence, the well-studied linear system theory can be adopted to analyze

MRIG performance. This provides a tractable and predictable way of designing and analyzing the performance of MRIG controllers. Such a fundamental improvement opened up new opportunities for linear control theory for the control of MRIGs, and drastically ease the MRIG controller design and analysis. Simulation study was performed on a symmetric MRIG model and verified the efficacy of such a new demodulation scheme.

The feedback controller, the method of averaging with the new demodulation scheme, can effectively operate a symmetric MRIG in rate integrating mode with a very high level of accuracy that far meets the requirements. However, an actual MRIG produced on microfabrication mass producing lines is usually susceptible to stiffness frequency mismatch and damping mismatch due to the fabrication imperfections. Analysis and simulation study showed that these mismatches dramatically degrade the gyro performance, even cause the gyro to stall in some extreme conditions. This lends the necessity of mismatch compensation schemes

Two compensation schemes that compensate for the gyro frequency and damping mismatches were studied. The first one is electrostatic spring softening and tuning method. This method can compensate the frequency mismatch via applying appropriate bias voltages on sensing and actuation electrodes. Experiments showed that this method can reduce the frequency mismatch within 0.5 Hertz, more than 26 decibels of attenuation on initial frequency mismatch. The method of electrostatic spring softening and tuning can be performed after the gyro resonator is packaged, but prior to the gyro operation. Hence its performance is degraded by parasitic voltage that is varying over time and temperature when gyro is in operation. In addition, such a compensation scheme is time consuming and requires much human involvement.

The other way to compensate for the mismatch is improving the control algorithm. This dissertation proposed an adaptive compensation scheme to compensate for the frequency and damping mismatches. The proposed compensator runs as an add-on feedforward compensator to the feedback controller. In this way, the feedback controller provides the baseline controller with required robustness level, while the adaptive compensator is specifically used to estimate and compensate the damping and frequency mismatches, in order to achieve a sufficient level of performance. Simulation results indicated that such adaptive scheme can correctly estimate and compensate the unknown mismatch. Since the convergence rate of the adaptive scheme relies on input rates, it has a quite long transient response for small input rates. Such a long transient response will in turn delay the gyro precession, hence resulting in a considerable DC bias in angle measurement. In order to shorten the transient response of the proposed adaptive compensators, and also obtain the sufficient persistence of excitation and avoid the stall condition, an artificial input rate was introduced to speed up the precession of gyro's principal axis of vibration. It was also shown that, the artificial input rate is capable of calibrating the gyro mismatches automatically, requiring no auxiliary device or human involvement.

6.2 Future Work

Based on the controller design methodology presented in this dissertation, several related aspects of research can be performed in future.

Implement the feedback controller presented in this dissertation on real MRIGs. Most of the effort in this dissertation has been focused on mathematical derivation and simulation, there are many actual issues to investigate when implementing such a feedback control law. To name a few, since the control actuation and the feedback signal are at the same frequency (i.e. the resonance frequency of the $n = 2$ mode of vibration), feed-through takes place on the electronic board. Feed-through can contaminate the readout signal and degrade the control performance in some extent. In principle, such a feed-through can be eliminated by modulating the control actuation onto a frequency that is far higher than the resonance frequency. A very simple modulation scheme is flipping the sign of the voltages applied on MRIG actuation electrodes back and forth at such a high frequency. Notice that sign flipping does not alter the force produced on the electrode as the force is determined by the voltage squared (see Eq. (2.25)). Other considerations include saturation on control actuation, computational complexity of the control algorithm, etc. Even though the simulation study performed on MRIG model has shown that they can achieve very high level of performance, it would be much convincing and great valuable if they can be demonstrated on real MRIGs.

Apply the mismatch compensation scheme and self-calibration method to actual MRIGs. Simulation results presented in this dissertation has shown the efficacy of the adaptive mismatch compensation scheme and the artificial precession rate. It would be interesting to apply them to actual MRIGs and investigate the convergence rate and accuracy of the on-line parameter adaptation algorithm, the efficacy of artificial precession rate, and demonstrate a working MRIG under different environment conditions.

The feedback controller and the parameter adaptation algorithm presented in this dissertation are both running at the sampling rate (i.e. 96kHz). This is, however, not necessary. Recall that the resonance frequency is around 8kHz. Since the feedback controller and parameter adaptation algorithm are built on the slow dynamics (i.e. the energy, quadrature, phase reference error, and precession angle) which changes far slower than the high frequency oscillation at the resonance frequency. The feedback control rate can be drastically reduced. Only the control modulation needs to run at the sampling rate. This can significantly save the computation time, without degrading the controller performance.

Design more complicated feedback controllers that can achieve better performance. The new demodulation scheme presented in this dissertation enables the use of linear control theory for MRIG control. But the controllers are not limited within the class of Proportional-Integral (PI) controller that was presented in this dissertation. More complicated feedback controller can be adopted to achieve better MRIG performance.

Bibliography

[1] Cenk Acar and Andrei Shkel. *MEMS vibratory gyroscopes: structural approaches to improve robustness*. Springer Science & Business Media, 2008.

[2] Cenk Acar and Andrei M Shkel. "An approach for increasing drive-mode bandwidth of MEMS vibratory gyroscopes". In: *Microelectromechanical Systems, Journal of* 14.3 (2005), pp. 520–528.

[3] Riccardo Antonello and Roberto Oboe. *MEMS Gyroscopes for Consumers and Industrial Applications*. INTECH Open Access Publisher, 2011.

[4] HJ Arditty and Herbert C Lefevre. "Sagnac effect in fiber gyroscopes". In: *Optics letters* 6.8 (1981), pp. 401–403.

[5] Mario N Armenise et al. "Advances in Gyroscope Technologies". In: ed. by Mario N Armenise et al. Springer, 2011. Chap. Introduction.

[6] Karl J Åström and Björn Wittenmark. *Adaptive control*. Courier Corporation, 2013.

[7] LK Baxter. "Capacitive sensors offer numerous advantages". In: *Electronic design* 46.2 (1998), pp. 46–55.

[8] Giovanni Bianchi and Roberto Sorrentino. *Electronic filter simulation & design*. McGraw-Hill New York, 2007.

[9] Niels Bruckner and Richard Packard. "Large area multiturn superfluid phase slip gyroscope". In: *Journal of applied physics* 93.3 (2003), pp. 1798–1805.

[10] GH Bryan. "On the beats in the vibrations of a revolving cylinder or bell". In: *Proceedings of the Cambridge Philosophical Society*. Vol. 7. 1. 1890, pp. 101–111.

[11] JS Burdess et al. "A review of vibratory gyroscopes". In: *Engineering Science & Education Journal* 3.6 (1994), pp. 249–254.

[12] Stephen Butterworth. "On the theory of filter amplifiers". In: *Wireless Engineer* 7.6 (1930), pp. 536–541.

[13] M Chia et al. "Ao electroformed CMOS integrated angular rate sensor". In: *Sensors & Actuators: A. Physical* 1.66 (1998), pp. 138–143.

[14] J Cho et al. "A high-Q birdbath resonator gyroscope (BRG)". In: *Solid-State Sensors, Actuators and Microsystems (TRANSDUCERS & EUROSENSORS XXVII), 2013 Transducers & Eurosensors XXVII: The 17th International Conference on*. IEEE. 2013, pp. 1847–1850.

[15] Jae Yoong Cho. "High-performance micromachined vibratory rate-and rate-integrating gyroscopes". PhD thesis. The University of Michigan, 2012.

[16] C Ciminelli. "Innovative photonic technologies for gyroscope systems". In: *EOS Topical Meeting-Photonic Devices in Space, Paris*. 2006, pp. 18–19.

[17] Caterina Ciminelli, Francesco Peluso, and Mario N Armenise. "A new integrated optical angular velocity sensor". In: *Integrated Optoelectronic Devices 2005*. International Society for Optics and Photonics. 2005, pp. 93–100.

[18] William A Clark, Thor Juneau, and Roger T Howe. *Micromachined vibratory rate gyroscope*. US Patent 6,067,858. 2000.

[19] J Classen et al. "MEMS gyroscopes for automotive applications". In: *Advanced Microsystems for Automotive Applications*. Springer. 2007, pp. 291–306.

[20] Joseph De Fato and Ralph A Patterson. "Fiber Optic Gyro Development for Navy Shipboard Inertial Reference System Applications". In: *s ELECTE* (1995), p. 78.

[21] A Defendini et al. "A compact CMG product for agile satellites". In: *Space Technology* 24.1 (2004), pp. 1–6.

[22] *Distributed Mass Hemispherical Resonator Gyroscope*. URL: `http://www.faqs.org/patents/imgfull/20120144917_05`.

[23] Lili Dong and Robert P Leland. "The adaptive control system of a MEMS gyroscope with time-varying rotation rate". In: *American Control Conference, 2005. Proceedings of the 2005*. IEEE. 2005, pp. 3592–3597.

[24] Lili Dong, Qing Zheng, and Zhiqiang Gao. "On control system design for the conventional mode of operation of vibrational gyroscopes". In: *Sensors Journal, IEEE* 8.11 (2008), pp. 1871–1878.

[25] G Greenhill. "A Treatise on Gyrostatics and Rotational Motion Theory and Applications". In: *Nature* 103 (1919), pp. 121–122.

[26] JA Gregory, J Cho, and K Najafi. "Characterization and control of a high-Q MEMS inertial sensor using low-cost hardware". In: *Position Location and Navigation Symposium (PLANS), 2012 IEEE/ION*. IEEE. 2012, pp. 239–247.

[27] JA Gregory, J Cho, and K Najafi. "MEMS rate and rate-integrating gyroscope control with commercial software defined radio hardware". In: *Solid-State Sensors, Actuators and Microsystems Conference (TRANSDUCERS), 2011 16th International*. IEEE. 2011, pp. 2394–2397.

[28] Jeffrey A Gregory, J Cho, and Khalil Najafi. "Novel mismatch compensation methods for rate-integrating gyroscopes". In: *Position Location and Navigation Symposium (PLANS), 2012 IEEE/ION*. IEEE. 2012, pp. 252–258.

[29] *Gyroscopes and Accelerometers on a Chip*. URL: `http://www.geekmomprojects.com/gyroscopes-and-accelerometers-on-a-chip/`.

[30] Simon S Haykin. *Adaptive filter theory*. Pearson Education India, 2008.

[31] Amir Heidari et al. "Hemispherical wineglass resonators fabricated from the microcrystalline diamond". In: *Journal of Micromechanics and Microengineering* 23.12 (2013), p. 125016.

[32] *Hemispherical Resonator Gyroscope*. URL: `http://timeandnavigation.si.edu/multimedia-asset/hemispherical-resonator-gyroscope`.

[33] Texas Instruments. "OMAP-L138 C6-Integra DSP+ ARM Processor". In: *SPRS586D, Oct* (2011).

[34] EA Izmailov et al. "Hemispherical resonator gyro technology. Problems and possible ways of their solutions". In: *RTO SCI International Conference on Integrated Navigation Systems*. 1999.

[35] Xuesong Jiang et al. "A monolithic surface micromachined Z-axis gyroscope with digital output". In: *VLSI Circuits, 2000. Digest of Technical Papers. 2000 Symposium on*. IEEE. 2000, pp. 16–19.

[36] James D John and Thurai Vinay. "Novel concept of a single-mass adaptively controlled triaxial angular rate sensor". In: *Sensors Journal, IEEE* 6.3 (2006), pp. 588–595.

[37] Burgess R Johnson et al. "Toroidal resonators with small frequency mismatch for rate integrating gyroscopes". In: *Inertial Sensors and Systems (ISISS), 2014 International Symposium on*. IEEE. 2014, pp. 1–4.

[38] M Kanik et al. "Microscale three-dimensional hemispherical shell resonators fabricated from metallic glass". In: *Inertial Sensors and Systems (ISISS), 2014 International Symposium on*. IEEE. 2014, pp. 1–4.

[39] VN Koshliakov. "The theory of a gyrocompass". In: *Journal of Applied Mathematics and Mechanics* 23.5 (1959), pp. 1164–1173.

[40] Benjamin C Kuo. *Automatic control systems*. Prentice Hall PTR, 1981.

[41] VJ Lappas, WH Steyn, and CI Underwood. "Torque amplification of control moment gyros". In: *Electronics Letters* 38.15 (2002), pp. 837–839.

[42] Herve C Lefevre and Herve J Arditty. "Fiber-optic gyroscope". In: *In AGARD, Advances in Fibre-Optic Technology in Communications and for Guidance and Control 6 p (SEE N92-28084 18-32)*. Vol. 1. 1992.

[43] Robert P Leland. "Adaptive tuning for vibrational gyroscopes". In: *IEEE CONFERENCE ON DECISION AND CONTROL*. Vol. 4. IEEE; 1998. 2001, pp. 3447–3452.

[44] Robert P Leland, Yacov Lipkin, and Alton Highsmith. "Adaptive oscillator control for a vibrational gyroscope". In: *American Control Conference, 2003. Proceedings of the 2003*. Vol. 4. IEEE. 2003, pp. 3347–3352.

[45] Robert Patton Leland. "Adaptive control of a MEMS gyroscope using Lyapunov methods". In: *Control Systems Technology, IEEE Transactions on* 14.2 (2006), pp. 278–283.

[46] Edward J Loper and David D Lynch. "The HRG: A new low-noise inertial rotation sensor". In: *Proc. 16 th Jt. Services Data Exchange For Inertial Systems, Los Angeles, CA* (1982).

[47] Robert Lutwak. "Micro-Technology for Positioning, Navigation, and Timing Towards PNT Everywhere and Always". In: *Inertial Sensors and Systems (ISISS), 2014 International Symposium on*. IEEE. 2014, pp. 1–4.

[48] David D Lynch. "Hemispherical resonator gyro". In: *Inertial Technology for the Future, IEEE Transactions on Aerospace Electronic Systems* 20.4 (1984), pp. 414–444.

[49] David D Lynch, Ryan R Savava, and James J Campanile. *Hemispherical resonator gyro control*. US Patent 7,318,347. 2008.

[50] DD Lynch. "Vibratory gyro analysis by the method of averaging". In: *Proc. 2nd St. Petersburg Conf. on Gyroscopic Technology and Navigation, St. Petersburg*. 1995, pp. 26–34.

[51] DD Lynch and A Matthews. "Dual-mode hemispherical resonator gyro operating characteristics". In: *Saint Petersburg International Conference on Integrated Navigation Systems, 3 rd, St. Petersburg, Russia*. 1996, pp. 37–44.

[52] WM Macek and DTM Davis Jr. "ROTATION RATE SENSING WITH TRAVELING-WAVE RING LASERS". In: *Applied Physics Letters* 2.3 (1963), pp. 67–68.

[53] Robert T M'Closkey and Alex Vakakis. "Analysis of a microsensor automatic gain control loop". In: *American Control Conference, 1999. Proceedings of the 1999*. Vol. 5. IEEE. 1999, pp. 3307–3311.

[54] Michael G Morrow, Cameron HG Wright, and Thad B Welch. "winDSK8: A user interface for the OMAP-L138 DSP board". In: *Acoustics, Speech and Signal Processing (ICASSP), 2011 IEEE International Conference on*. IEEE. 2011, pp. 2884–2887.

[55] S Murugesan and PS Goel. "Autonomous fault-tolerant attitude reference system using DTGs in symmetrically skewed configuration". In: *Aerospace and Electronic Systems, IEEE Transactions on* 25.2 (1989), pp. 302–307.

[56] Deepan Muthirayan and Roberto Horowitz. "A Self-Tuning Algorithm for Z-Axis Micro Rate Integrating Gyroscopes". In: *ASME 2012 5th Annual Dynamic Systems and Control Conference joint with the JSME 2012 11th Motion and Vibration Conference*. American Society of Mechanical Engineers. 2012, pp. 235–244.

[57] B SOMANATHAN NAIR and SR Deepa. *APPLIED ELECTROMAGNETIC THEORY: Analyses, Problems and Applications*. PHI Learning Pvt. Ltd., 2008.

[58] Steven Nasiri et al. "A critical review of MEMS gyroscopes technology and commercialization status". In: *Avaliable online: http://invensense. com/mems/gyro/documents/whitepapers/ME (accessed on 25 May 2012)* (2009).

[59] Sungsu Park. "Adaptive control of a vibratory angle measuring gyroscope". In: *Sensors* 10.9 (2010), pp. 8478–8490.

[60] Sungsu Park. "Adaptive control strategies for MEMS gyroscopes". PhD thesis. University of California, Berkeley, 2000.

[61] Sungsu Park and Roberto Horowitz. "Adaptive control for the conventional mode of operation of MEMS gyroscopes". In: *Microelectromechanical Systems, Journal of* 12.1 (2003), pp. 101–108.

[62] Sungsu Park and Roberto Horowitz. "Adaptive control for Z-axis MEMS gyroscopes". In: *American Control Conference, 2001. Proceedings of the 2001.* Vol. 2. IEEE. 2001, pp. 1223–1228.

[63] Michael Perlmutter and Laurent Robin. "High-performance, low cost inertial MEMS: A market in motion!" In: *Position Location and Navigation Symposium (PLANS), 2012 IEEE/ION*. IEEE. 2012, pp. 225–229.

[64] Popovic B Popovic. "Introductory Electromagnetics Z". In: (2000).

[65] Igor P Prikhodko et al. "Foucault pendulum on a chip: Rate integrating silicon MEMS gyroscope". In: *Sensors and Actuators A: Physical* 177 (2012), pp. 67–78.

[66] Md Mahbubur Rahman et al. "3-D hemispherical micro glass-shell resonator with integrated electrostatic excitation and capacitive detection transducers". In: *Micro Electro Mechanical Systems (MEMS), 2014 IEEE 27th International Conference on*. IEEE. 2014, pp. 672–675.

[67] David M Rozelle. "The hemispherical resonator gyro: From wineglass to the planets". In: *Proc. 19th AAS/AIAA Space Flight Mechanics Meeting*. 2009, pp. 1157–1178.

[68] Mohammad Salah et al. "Time-varying angular rate sensing for a MEMS Z-axis gyroscope". In: *Decision and Control, 2006 45th IEEE Conference on*. IEEE. 2006, pp. 2165–2170.

[69] D Senkal et al. "Demonstration of sub-1 Hz structural symmetry in micro-glassblown wineglass resonators with integrated electrodes". In: *Solid-State Sensors, Actuators and Microsystems (TRANSDUCERS & EUROSENSORS XXVII), 2013 Transducers & Eurosensors XXVII: The 17th International Conference on*. IEEE. 2013, pp. 1380–1383.

[70] Derek K Shaeffer. "MEMS inertial sensors: A tutorial overview". In: *Communications Magazine, IEEE* 51.4 (2013), pp. 100–109.

[71] A Shkel, Roger T Howe, and Roberto Horowitz. "Modeling and simulation of micromachined gyroscopes in the presence of imperfections". In: *Int. Conf. On Modelling and Simulation of Microsystems*. 1999, pp. 605–608.

[72] Andrei M Shkel. "Micromachined gyroscopes: challenges, design solutions, and opportunities". In: *SPIE's 8th Annual International Symposium on Smart Structures and Materials*. International Society for Optics and Photonics. 2001, pp. 74–85.

[73] Andrei M Shkel. "Precision navigation and timing enabled by microtechnology: Are we there yet?" In: *SPIE Defense, Security, and Sensing*. International Society for Optics and Photonics. 2011, pp. 803118–803118.

[74] Andrei M Shkel. "Type I and Type II micromachined vibratory gyroscopes". In: *Position, Location, and Navigation Symposium, San Diego*. 2006, pp. 25–27.

[75] Andrei M Shkel, Cenk Acar, and Chris Painter. "Two types of micromachined vibratory gyroscopes". In: *Sensors, 2005 IEEE*. IEEE. 2005, 6–pp.

[76] Andrei M Shkel et al. "Dynamics and control of micromachined gyroscopes". In: *American Control Conference, 1999. Proceedings of the 1999*. Vol. 3. IEEE. 1999, pp. 2119–2124.

[77] LD Sorenson, X Gao, and F Ayazi. "3-D micromachined hemispherical shell resonators with integrated capacitive transducers". In: *Micro Electro Mechanical Systems (MEMS), 2012 IEEE 25th International Conference on*. IEEE. 2012, pp. 168–171.

[78] P Taheri-Tehrani et al. "Micro-scale diamond hemispherical resonator gyroscope". In: *Hilton Head Workshop*. 2014, pp. 289–292.

[79] David Titterton and John L Weston. *Strapdown inertial navigation technology*. Vol. 17. IET, 2004.

[80] Alexander A Trusov. "Overview of MEMS Gyroscopes: History, Principles of Operations, Types of Measurements". In: *University of California, Irvine, USA, maj* (2011).

[81] Alexander A Trusov et al. "Ultra-high Q silicon gyroscopes with interchangeable rate and whole angle modes of operation". In: *Sensors, 2010 IEEE*. IEEE. 2010, pp. 864–867.

[82] Xu Wang et al. "The modeling of hemispherical resonator gyro and its space applications". In: *Proc. SPIE* 8321 (2011), pp. 832104–832104–9. DOI: 10.1117/12.903641. URL: http://dx.doi.org/10.1117/12.903641.

[83] Paul Ward. *Electronics for Coriolis force and other sensors*. US Patent 5,481,914. 1996.

[84] Marc Weinberg et al. "Energy loss in MEMS resonators and the impact on inertial and RF devices". In: *Proc. Transducers 2009* (2009), pp. 688–695.

[85] *Wikipedia - Gyroscope*. URL: http://en.wikipedia.org/wiki/Gyroscope.

[86] *Wikipedia - Hemispherical resonator gyroscope*. URL: http://en.wikipedia.org/wiki/Hemispherical_resonator_gyroscope.

[87] *Wikipedia - Quadrature amplitude modulation*. URL: http://en.wikipedia.org/wiki/QAM#Receiver.

[88] KF Woodman, PW Franks, and MD Richards. "The nuclear magnetic resonance gyroscope: a review". In: *Journal of Navigation* 40.03 (1987), pp. 366–384.

[89] Peter C Young. "Recursive Least Squares Estimation". In: *Recursive Estimation and Time-Series Analysis*. Springer, 2011, pp. 29–46.

[90] Fu Zhang et al. "The method of averaging using an adaptive notch filter in vibratory gyroscopes". In: *Inertial Sensors and Systems (ISISS), 2014 International Symposium on*. IEEE. 2014, pp. 1–4.

Appendix A

Derivation of the New Demodulation Scheme

Problem setups. Given the input signal in the form of

$$\begin{aligned} x &= a\cos\theta\cos(\omega t+\phi_0) - q\sin\theta\sin(\omega t+\phi_0) \\ y &= a\sin\theta\cos(\omega t+\phi_0) + q\cos\theta\sin(\omega t+\phi_0) \end{aligned} \tag{A.1}$$

and a phase reference $\omega t + \phi$. The energy E, variable R, S, phase reference error L and quadrature Q are respectively defined as

$$\begin{aligned} E &= a^2+q^2 \\ R &= \cos 2\theta \\ S &= \sin 2\theta \\ L &= (a^2-q^2)\sin 2(\phi-\phi_0) \\ Q &= 2aq \end{aligned} \tag{A.2}$$

Need to show that E_h, R_h, S_h, L_h and Q_h, which are respectively defined as

$$\begin{aligned} E_h &= \tfrac{x_c^2+x_s^2+y_c^2+y_s^2}{2} \\ R_h &= \tfrac{x_c^2+x_s^2-y_c^2-y_s^2}{2} \\ S_h &= x_c y_c + x_s y_s \\ L_h &= 2(x_c x_s + y_c y_s) \\ Q_h &= 2(y_c y_s - x_c x_s)\sin 2\hat{\theta} + 2(x_s y_c + x_c y_s)\cos 2\hat{\theta} \end{aligned} \tag{A.3}$$

where

$$\begin{aligned} x_c &= 2x\cos(\omega t+\phi) \\ x_s &= 2x\sin(\omega t+\phi) \\ y_c &= 2y\cos(\omega t+\phi) \\ y_s &= 2y\sin(\omega t+\phi) \end{aligned} \tag{A.4}$$

satisfies

$$\begin{array}{rcl} E_h &=& E + a_E \sin(2\omega t + \phi_E) \\ R_h &=& R + a_R \sin(2\omega t + \phi_R) \\ S_h &=& S + a_S \sin(2\omega t + \phi_S) \\ L_h &=& L + a_L^1 \sin(2\omega t + \phi_L^1) + a_L^2 \sin(4\omega t + \phi_L^2) \\ Q_h &=& Q + a_Q^1 \sin(2\omega t + \phi_Q^1) + a_Q^2 \sin(4\omega t + \phi_Q^2) \end{array} \tag{A.5}$$

for some $a_E, a_R, a_S, a_L^1, a_L^2, a_Q^1, a_Q^2, \phi_E, \phi_R, \phi_S, \phi_L^1, \phi_L^2, \phi_Q^1$ and ϕ_Q^2.

Proof. In order to simplify the proof, define

$$C := \begin{bmatrix} x_c + ix_s \\ y_c + iy_s \end{bmatrix} \tag{A.6}$$

and

$$\sigma_1 = \begin{bmatrix} 0 & 1 \\ 1 & 0 \end{bmatrix}; \sigma_2 = \begin{bmatrix} 1 & 0 \\ 0 & -1 \end{bmatrix}; \sigma_3 = \begin{bmatrix} -\sin 2\hat{\theta} & \cos 2\hat{\theta} \\ \cos 2\hat{\theta} & \sin 2\hat{\theta} \end{bmatrix}; \tag{A.7}$$

Using these notations, it can be shown that Eq. (A.3) can be rewritten as

$$\begin{array}{rcl} E_h &=& \frac{1}{2} C^* C \\ R_h &=& \frac{1}{2} C^* \sigma_2 C \\ S_h &=& \frac{1}{2} C^* \sigma_1 C \\ L_h &=& Im\left[C^T C\right] \\ Q_h &=& Im\left[C^T \sigma_3 C\right] \end{array} \tag{A.8}$$

where C^* denotes the complex conjugate of C; C^T denotes the transpose of C; $Im[C]$ denotes the imaginary part of C.

Also notice that

$$C = 2 \begin{bmatrix} x \\ y \end{bmatrix} e^{i(\omega t + \phi)} \tag{A.9}$$

Substituting Eq. (A.1) into Eq. (A.9) yields

$$C = 2 \begin{bmatrix} \cos\theta & -\sin\theta \\ \sin\theta & \cos\theta \end{bmatrix} \begin{bmatrix} \cos(\omega t + \phi_0) & 0 \\ 0 & \sin(\omega t + \phi_0) \end{bmatrix} \begin{bmatrix} a \\ q \end{bmatrix} e^{i(\omega t + \phi)} \tag{A.10}$$

Substituting Eq. (A.10) into Eq. (A.8) and assuming $\hat{\theta} = \theta$ yields

$$\begin{array}{rcl} E_h &=& a^2 + q^2 + a^2 \cos(2\omega t + 2\phi_0) - q^2 \sin(2\omega t + 2\phi_0) \\ R_h &=& (a^2 - q^2)\cos 2\theta + (a^2 + q^2)\cos 2\theta \cos(2\omega t + 2\phi_0) - 2aq \sin 2\theta \sin(2\omega t + 2\phi_0) \\ S_h &=& (a^2 - q^2)\sin 2\theta + (a^2 + q^2)\sin 2\theta \cos(2\omega t + 2\phi_0) + 2aq \cos 2\theta \sin(2\omega t + 2\phi_0) \\ L_h &=& (a^2 - q^2)\sin 2\delta\phi + 2(a^2 + q^2)\sin(2\omega t + 2\phi) + (a^2 - q^2)\sin(4\omega t + 2\phi_0 + 2\phi) \\ Q_h &=& Q \cos 2\delta\phi - Q \cos(4\omega t + 2\phi_0 + 2\phi) \end{array} \tag{A.11}$$

where $\delta\phi = \phi - \phi_0$.

Comparing Eq. (A.11) with Eq. (A.2) and assuming $\delta\phi = 0$, it can be seen that

$$\begin{aligned} E_h &= E + a_E \sin(2\omega t + \phi_E) \\ R_h &= R + a_R \sin(2\omega t + \phi_R) \\ S_h &= S + a_S \sin(2\omega t + \phi_S) \\ L_h &= L + a_L^1 \sin(2\omega t + \phi_L^1) + a_L^2 \sin(4\omega t + \phi_L^2) \\ Q_h &= Q + a_Q \sin(4\omega t + \phi_Q) \end{aligned} \tag{A.12}$$

where

$$\begin{aligned} a_E &= \sqrt{a^4 + q^4} \\ \phi_E &= \tfrac{\pi}{2} + \tan^{-1} \tfrac{q^2}{a^2} \\ a_R &= \sqrt{E^2 \cos^2 2\theta + Q^2 \sin^2 2\theta} \\ \phi_R &= \tfrac{\pi}{2} + \tan^{-1} \tfrac{Q \sin 2\theta}{E \cos 2\theta} \\ a_S &= \sqrt{E^2 \sin^2 2\theta + Q^2 \cos^2 2\theta} \\ \phi_R &= \tfrac{\pi}{2} - \tan^{-1} \tfrac{Q \cos 2\theta}{E \sin 2\theta} \\ a_L^1 &= 2E \\ \phi_L^1 &= 2\phi \\ a_L^2 &= a^2 - q^2 \\ \phi_L^2 &= 2\phi_0 + 2\phi \\ a_Q &= Q \\ \phi_Q &= -\tfrac{\pi}{2} + 2\phi_0 + 2\phi \end{aligned} \tag{A.13}$$

This completes the proof. □

Appendix B

Proof of Lemma 1

Lemma 1. *Given a nonlinear system described by*

$$\dot{\theta} = \lambda \sin\theta + c; \quad |\lambda| > |c|, \quad \lambda, c \in \mathbb{R} \tag{B.1}$$

there exists infinite number of equilibrium points:

$$\theta_{eq} = \begin{cases} 2m\pi + \sin^{-1}\left(-\frac{c}{\lambda}\right) \\ 2m\pi + \pi - \sin^{-1}\left(-\frac{c}{\lambda}\right) \end{cases}; \; m \in \mathbb{N} \tag{B.2}$$

Given $\lambda > 0$, then $2m\pi + \pi - \sin^{-1}\left(-\frac{c}{\lambda}\right)$ is the group of stable equilibrium points. Given $\lambda < 0$, $2m\pi + \sin^{-1}\left(-\frac{c}{\lambda}\right)$ is the group of stable equilibrium points.

Proof. Equilibrium points of the system described by Eq. (B.1) can be obtained by setting $\dot{\theta} = 0$. The set of solutions is shown in Fig. B.1.

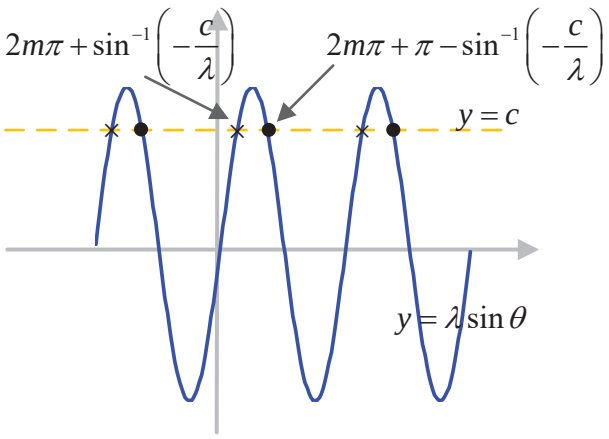

Figure B.1: Equilibrium points of the system $\dot{\theta} = \lambda \sin\theta + c$.

To show the stability of the equilibrium points, the proof for the case where $\lambda < 0$ is given as follows. Proof for the case where $\lambda > 0$ is similar. Let $\theta_{eq} = 2m\pi + \sin^{-1}\left(-\frac{c}{\lambda}\right)$ be the equilibrium to study.

$$\theta = \theta_{eq} + \tilde{\theta} \tag{B.3}$$

where $\tilde{\theta}$ is small variation from the equilibrium point.

Substituting Eq. (B.3) into Eq. (B.1) yields

$$\dot{\tilde{\theta}} = \lambda \sin\theta_{eq} \cos\tilde{\theta} + \lambda \cos\theta_{eq} \sin\tilde{\theta} + c; \tag{B.4}$$

Since $\theta_{eq} = 2m\pi + \sin^{-1}\left(-\frac{c}{\lambda}\right)$, we have

$$\sin\theta_{eq} = \sin\left[\sin^{-1}\left(-\frac{c}{\lambda}\right)\right] \tag{B.5}$$

$$= -\frac{c}{\lambda}; \tag{B.6}$$

Since the range of function $\sin^{-1}(\cdot)$ is $[-\frac{\pi}{2}, \frac{\pi}{2}]$, over which the cosine function is always positive. Therefore

$$\cos\theta_{eq} = \cos\left[\sin^{-1}\left(-\frac{c}{\lambda}\right)\right] \tag{B.7}$$

$$= \frac{\sqrt{\lambda^2 - c^2}}{|\lambda|} \tag{B.8}$$

$$= -\frac{\sqrt{\lambda^2 - c^2}}{\lambda} \quad \text{for} \quad \lambda < 0 \tag{B.9}$$

Substituting Eq. (B.6) and Eq. (B.9) into Eq. (B.4) yields

$$\dot{\tilde{\theta}} = -c\cos\tilde{\theta} - \sqrt{\lambda^2 - c^2}\sin\tilde{\theta} + c \tag{B.10}$$

When $\tilde{\theta} \approx 0$, $\cos\tilde{\theta} \approx 1, \sin\tilde{\theta} \approx \tilde{\theta}$. As a result,

$$\dot{\tilde{\theta}} = -\sqrt{\lambda^2 - c^2}\ \tilde{\theta} \tag{B.11}$$

The linearized system is stable. As a result, the system given by Eq. (B.1) is stable at the equilibrium points $2m\pi + \sin^{-1}\left(-\frac{c}{\lambda}\right); m \in \mathbb{N}$. $\square$

Appendix C

Proof of Lemma 2

Lemma 2. *Given a system described by*

$$y(k) = G(z)\left[\Theta^T\Phi(k) - u(k)\right] \tag{C.1}$$

where $G(z)$ is strictly casual and asymptotically stable; and $u(k)$ is updated by the following Parameter Adaptation Algorithm (PAA)

$$\begin{aligned}
\Psi(k-1) &= G(z)\left[\Phi(k)\right] && \text{(C.2)}\\
e^o(k) &= y(k) - \widehat{\Theta}(k-1)^T\Psi(k-1) + G(z)\left[\widehat{\Theta}^T(k)\Phi(k)\right] && \text{(C.3)}\\
e(k) &= \frac{\lambda_1 e^o(k)}{\lambda_1 + \Psi(k-1)^T F(k-1)\Psi(k-1)} && \text{(C.4)}\\
\widehat{\Theta}(k) &= \widehat{\Theta}(k-1) + \frac{1}{\lambda_1}F(k-1)\Psi(k-1)e(k) && \text{(C.5)}\\
u(k) &= \widehat{\Theta}(k)^T\Phi(k) && \text{(C.6)}\\
F(k) &= \frac{1}{\lambda_1}\left[F(k-1) - \lambda_2\frac{F(k-1)\Psi(k-1)\Psi(k-1)^T F(k-1)}{\lambda_1 + \lambda_2\Psi(k-1)^T F(k-1)\Psi(k-1)}\right] && \text{(C.7)}\\
&\widehat{\Theta}(0) = \Theta_0 \in \mathbb{R}^n_+; F(0) = F_0 \in \mathbb{S}^{n\times n}_+ && \text{(C.8)}\\
&0 < \lambda_1 \leq 1; 0 < \lambda_2 < 2 && \text{(C.9)}
\end{aligned}$$

Given the persistence of excitation, which is defined as

$$P.E. \triangleq rank\left(\lim_{m\to+\infty}\frac{\Sigma_{k=0}^{k=m}\Phi(k)\Phi^T(k)}{m}\right) \tag{C.10}$$

is greater than or equal to n, the PAA yields:

(1) $e(k) \to 0, e^o(k) \to 0$;
(2) $\widehat{\Theta}(k) \to \Theta$;
(3) $y(k) \to 0$.

Proof. Define the parameter estimation error

$$\widetilde{\Theta}(k) \triangleq \Theta - \widehat{\Theta}(k) \tag{C.11}$$

Substituting Eq. (C.11) into Eq. (C.5) yields:

$$\widetilde{\Theta}(k) = \widetilde{\Theta}(k-1) - \frac{1}{\lambda_1} F(k-1)\Psi(k-1)e(k); \tag{C.12}$$

Substituting Eq. (C.6) and Eq. (C.1) into Eq. (C.3) yields

$$e^o(k) = \widetilde{\Theta}(k-1)^T \Psi(k-1) \tag{C.13}$$

Substituting Eq. (C.12) into the Eq. (C.13) yields

$$e^o(k) = \widetilde{\Theta}(k)^T \Psi(k-1) + \frac{1}{\lambda_1} \Psi(k-1)^T F(k-1)\Psi(k-1)e(k) \tag{C.14}$$

Substituting the Eq. (C.14) into Eq. (C.4) yields

$$e(k) = \widetilde{\Theta}(k)^T \Psi(k-1) \tag{C.15}$$

As a result, $e, \widetilde{\Theta}$ and F are subject to

$$\begin{aligned} e(k) &= \widetilde{\Theta}(k)^T \Psi(k-1) && \text{(C.16)} \\ \widetilde{\Theta}(k) &= \widetilde{\Theta}(k-1) - \frac{1}{\lambda_1} F(k-1)\Psi(k-1)e(k) && \text{(C.17)} \\ F(k) &= \frac{1}{\lambda_1}\left[F(k-1) - \lambda_2 \frac{F(k-1)\Psi(k-1)\Psi(k-1)^T F(k-1)}{\lambda_1 + \lambda_2 \Psi(k-1)^T F(k-1)\Psi(k-1)}\right] && \text{(C.18)} \end{aligned}$$

which is a general Parameter Adaptation Algorithm. In addition, since $G(z)$ is asymptotically stable and $\Phi(k)$ is persistently exciting, $\Psi(k)$ is also persistently exciting [6]. As shown in [6], the above PAA produces zero a-priori and a-posteriori errors (i.e. conclusion (1)), and converges to the real values (i.e. conclusion (2)). Moreover, since $\widehat{\Theta}(k) \to \Theta$, it implies $u(k) \to d(k)$. Given that $G(z)$ is asymptotically stable, it concludes $y(k) \to 0$. □